/
Article / Book Information

( )	
Title(English)	Analysis of plate spin motion
( )	
Author(English)	Takeshi Matsuyama
( )	: ( ), : 10076 , :2016 3 26 , : , : , , , ,
Citation(English)	Degree:Doctor (Science), Conferring organization: Tokyo Institute of Technology, Report number: 10076 , Conferred date:2016/3/26, Degree Type:Course doctor, Examiner:,,,,
( )	
Type(English)	Doctoral Thesis

Doctoral Thesis

Analysis of plate spin motion

Takeshi Matsuyama

TOKYO TECH

Department of Earth and Planetary Sciences,
Tokyo Institute of Technology

2016

Abstract

Rapid growth and development of space geodetic methods, such as the global positioning system (GPS), have enabled us to construct high-resolution plate models, including the small plates (less than several hundred kilometers in plate size) and deformation of the plates. In this thesis, based on the high-resolution plate models, we analyze plate motion and the driving forces, particularly focusing on vorticity of the plate velocity field and spin motion of the individual plates. First, we perform spherical harmonic expansion of the plate velocity field to higher degrees (up to 1000) than ever and find an increase in the toroidal/poloidal ratio at the higher spherical harmonic degrees, which is different from the conventional view that the ratio is broadly constant. We investigate the effect of the variable geometry and motion of plate upon the toroidal-poloidal power and discuss the possible causes of the increase in toroidal/poloidal ratio. Next, we decompose the plate motion into a "spin" motion around the geometrical center of plate and a "straight" motion along the great circle. We investigate the relationship between the plate size and the two plate motions and find that the spin rotation rates of most of the small plates (less than approximately 1000 km in size) are distinctly higher than those of the larger plates. This relationship constrains the overall strength of plate boundaries to be 3 to 75 MPa, which is consistent with several seismological estimates, including those constrained from The 2011 off the Pacific coast of Tohoku Earthquake. Finally, we analyze the torque balance for the spin motion of the Philippine Sea plate (PHS), indicating that an eastward force is applied to the subducted PHS slab along its northern edge and could have caused the wavy geometry of the slab beneath southwestern Japan by viscous buckling, not by elastic deformation. Based on the folding theory, the slab viscosity is estimated to be 1 to 14×10^{24} Pa s.

Contents

Chapter 1

Introduction

1.1 Observations for plate motion

In addition to accumulation of conventionally utilized data from precise determination of location and slip vector of earthquakes, magnetic anomalies of the sea floor and the precise bathymetry data to assist detailed determination of plate boundaries, rapid growth and development of space geodetic methods, such as very long baseline interferometry (VLBI), satellite laser ranging (SLR) and the global positioning system (GPS), have enabled us to develop a new stage of plate motion study (e.g., Gordon, 1998), particularly after 2000. PB2002 (Bird, 2003), which we utilized for the analysis of plate motion in this study, compiled plate motion data and define plate configuration with the higher resolution than ever (Figure 1.1 and Table 1.1).

In Table 1.1, we compile the observation methods and the estimated errors. The observations include those from conventional methods, such as focal mechanisms, transform fault azimuth and magnetic anomaly of the oceanic plate, as well as relatively novel methods, such as those utilizing space geodesy. There are both advantages and disadvantages for individual methods. For example, the focal mechanism approach provides us with invaluable information on stress for a significant depth range (see Section 3.3.4), although the amount of displacement is not accurately estimated. On the other hand, the GPS ob-

Table. 1.1   Observations used in the plate model PB2002. Min in the 1σ column means that the observation did not estimate the error and we instead estimate the minimum error by considering the total errors of the relative Euler poles to obtain the Euler pole of the plate. For detail, please read the text in Section 3.3.2.

Plate Name		Observation	reference	1 σ [degree]
Africa	AF	Focal mechanism, transform fault azimuth and magnetic anomaly	DeMets et al. [1994]	7.91
Amur	AM	GPS	Heki et al. [1999]	27.51
Antarctica	AN	Focal mechanism, transform fault azimuth and magnetic anomaly	DeMets et al. [1994]	6.91
Altiplano	AP	GPS, paleomagnetism and focal mechanism	Lamb [2000]	RR:±0.07° /Myr
Arabia	AR	Focal mechanism, transform fault azimuth and magnetic anomaly	DeMets et al. [1994]	12.21
Aegean Sea	AS	GPS	McClusky et al. [2000]	9.51
Anatolia	AT	GPS	McClusky et al. [2000]	8.01
Australia	AU	Focal mechanism, transform fault azimuth and magnetic anomaly	DeMets et al. [1994]	6.71
Birds Head	BH	GPS	Bird [2003]	Min
Balmoral Reef	BR	Focal mechanism	Bird [2003]	Min
Banda Sea	BS	GPS	Rangin et al. [1999]	Min
Burma	BU	Tectonic Map	Circum-Pacific Map. Proj. [1986]	Min
Caribbean	CA	GPS	Weber et al. [2001]	17.41
Caroline	CL	Focal mechanism	Seno et al. [1993]	20.71
Cocos	CO	Focal mechanism, transform fault azimuth and magnetic anomaly	DeMets et al. [1994]	6.71
Conway Reef	CR	Focal mechanism and magnetic anomaly	Bird [2003]	Min
Easter	EA	Focal mechanism and magnetic anomaly	Engeln and Stein [1984]	6.3
Eurasia	EU	Focal mechanism, transform fault azimuth and magnetic anomaly	DeMets et al. [1994]	7.01
Futuna	FT	Focal mechanism and magnetic anomaly	Bird [2003]	Min
Galapagos	GP	Bathymetry and magnetic anomaly	Lonsdale [1988]	Min
India	IN	Focal mechanism, transform fault azimuth and magnetic anomaly	DeMets et al. [1994]	14.11
Juan de Fuca	JF	Magnetic anomaly	Wilson [1988]	Min
Juan Fernandez	JZ	Bathymetry and magnetic anomaly	Anderson-Fontana et al. [1986]	6.21
Kermadec	KE	GPS and focal mechanism	Bird [2003]	Min
Mariana	MA	GPS and magnetic anomaly	Bird [2003]	Min
Manus	MN	Magnetic anomaly	Martinez and Taylor [1996]	Min
Maoke	MO	GPS	Bird [2003]	RR:±0.4° /Myr
Molucca Sea	MS	GPS	Rangin et al. [1999]	Min
North America	NA	Focal mechanism, transform fault azimuth and magnetic anomaly	DeMets et al. [1994]	7.01
North Bismarck	NB	GPS	Tregoning et al. [1998]	6.52
North Andes	ND	GPS	Trenkamp et al. [1996]	Min
New Hebrides	NH	Magnetic anomaly	Bird [2003]	Min
Niuafo'ou	NI	Bathymetry, magnetic anomaly and focal mechanism	Zellmer and Taylor [2001]	9.71
Nazca	NZ	Focal mechanism, transform fault azimuth and magnetic anomaly	DeMets et al. [1994]	7.51
Okhotsk	OK	Focal mechanism	Cook et al. [1986]	15.11
Okinawa	ON	GPS	Bird [2003]	Min
Pacific	PA	Focal mechanism and magnetic anomaly	Gripp [2002]	5.71
Panama	PM	GPS	Kellog et al. [1995]	RR:±0.04° /Myr
Philippine Sea	PS	Focal mechanism and GPS	Seno et al. [1993]; Kato et al. [1998]	20.71
Rivera	RI	Focal mechanism, transform fault azimuth and magnetic anomaly	DeMets and Traylen[2000]	7.41
South America	SA	Focal mechanism, transform fault azimuth and magnetic anomaly	DeMets et al. [1994]	9.91
South Bismarck	SB	GPS	Tregoning et al. [1999]	6.07
Scotia	SC	Focal mechanism	Pelayo and Wiens [1989]	8.91
Shetland	SL	Hypothetical	Bird [2003]	Min
Somalia	SO	Focal mechanism and magnetic anomaly	Chu and Gordon [1999]	18.41
Solomon Sea	SS	GPS, transform fault azimuth	Bird [2003]	Min
Sunda	SU	GPS	Rangin et al. [1999]	Min
Sandwich	SW	Focal mechanism	Pelayo and Wiens [1989]	14.91
Timor	TI	GPS	Bird [2003]	Min
Tonga	TO	Bathymetry, magnetic anomaly and focal mechanism	Zellmer and Taylor [2001]	7.71
Woodlark	WL	GPS	Tregoning et al. [1998]	8.72
Yangtze	YA	GPS	Heki et al. [1999]	30.31

RR: Rotation Rate; Min: No Error Estimate
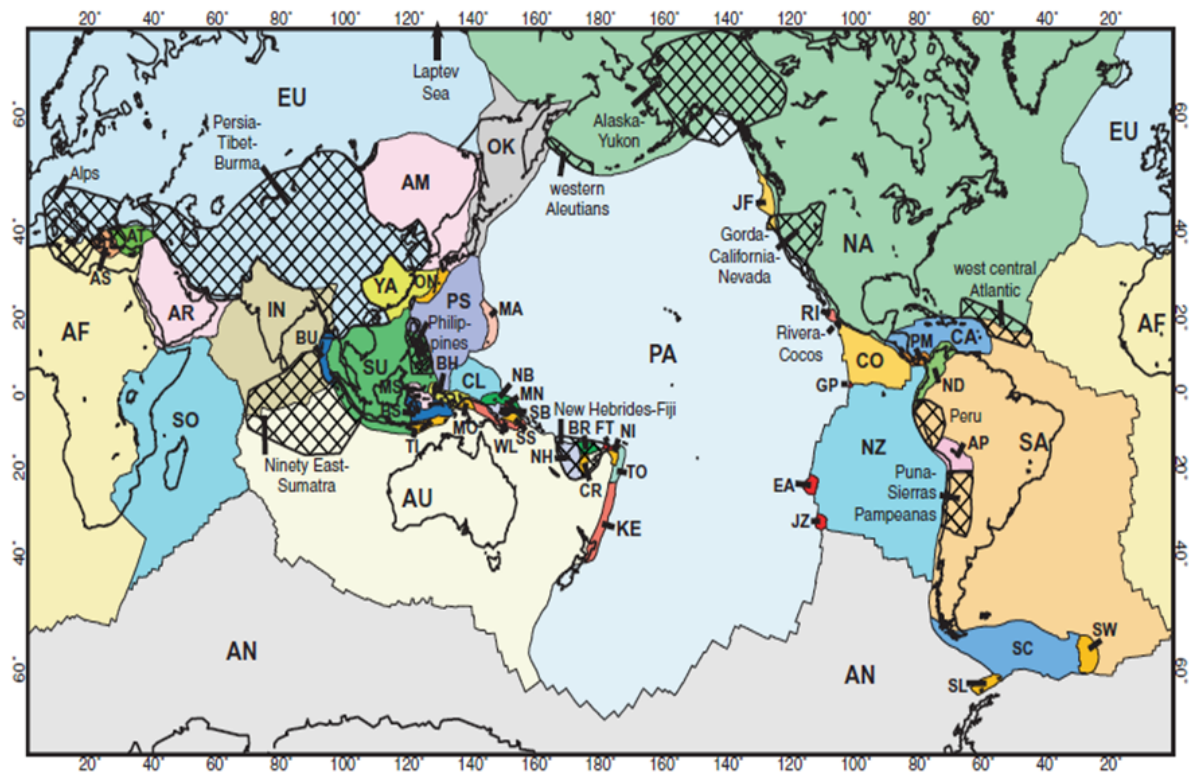
Fig. 1.1   The 52 plates of plate model PB2002 on a Mercator projection from Bird (2003). The cross-hatched areas are "orogens" where a rigid plate model is not expected to be accurate. As for two-letter plate abbreviations and plate names, please refer to the plate name table (Table 1.1).

servation accurately monitors the surface displacement, but it does not necessarily coincide the plate motion over a geologic time (which is important for our purpose in this study) due to, e.g., an elastic response or local deformation of the plate itself (e.g. Heki et al., 1999; Weber et al., 2001). Accordingly the combination of these methods may provide more accurate estimates on plate motion. Several Euler poles have been determined by the combination of the conventional method and GPS data (e.g., Seno et al. (1993); Kato et al. (1998) for the Philippine Sea plate). As Table 1.1 shows, those various observational methods and their combination help us acquire the more accurate plate motion data with the finer scale than ever.

Accordingly there are several remarkably improved aspects which have not been clearly seen in the earlier works. One aspect concerns the number and distribution of plates identified and their size variation. For instance, whereas Morgan (1972) defines 15 plates

in the plate model, PB2002 contains 52 plates, ranging from the largest Pacific plate of
> 10000 km to the smallest Manus plate of ~ 100 km (Table 3.1). Another important aspect
is that, although "plate" is originally defined as a rigid shell that is allowed to move differ-
ently from the adjacent plate, the space geodetic approaches clearly demonstrate that the
plates are not rigid and can deform (e.g., Gordon, 1998). Although the precise observa-
tional methods provide us with the detailed motions of the surface of the Earth, the data
contain both the plate motion and the plate deformation itself. In order to distinguish
these two, Bird (2003) defines "orogen" that represents a region where a significant defor-
mation undergoes (Figure 1.1). In another updated plate model, Kreemer et al. (2014) have
utilized more GPS data than PB2002 and defined plate configuration and motions. They
also defined the deformation zones in their plate model to exclude active deformation
zones (Table 3.1).

   Fully utilizing these accurate and fine-scale plate motion data, in this study, we inves-
tigate two essential aspects for understanding the plate motions, the toroidal-poloidal
power of the plate velocity field and the driving force of plate motions as follows.

1.2   Toroidal/poloidal ratio

Although the idea of mantle convection originated in the 19th century (Perry, 1895a,b,c)
and has been developed subsequently by, e.g., Lord Rayleigh (Strutt John William (Lord
Rayleigh), 1916), Benard (Benard, 1901) and Chandrasekhar (Chandrasekhar, 1961), one
of the important characteristics, toroidal-poloidal flow, in the convective regime was not
specifically studied until Hager and O'Connell (1978) who first discovered the equipar-
titioning of the toroidal power (associated with strike-slip motion and the horizontal
spin motion) and the poloidal power (associated with the thermal convection and the
divergent-convergent power). Hager and O'Connell (1978) remarked that the significant

power of toroidal motion comparable to poloidal motion is unexpected for thermal convection in the Earth, which was thought to primarily induce vertical circulation as a heat pump system. Subsequently the mechanism to generate a significant toroidal component (e.g. Bercovici, 1993, 1995a,b, 2003) and the temporal variation of toroidal/poloidal ratio (Lithgow-Bertelloni and Richards, 1993) have been investigated.

Numerical simulations of mantle convection utilize the toroidal/poloidal ratio and its spectrum as a benchmark feature upon simulation for reproducing the characteristics of the Earth. With the development of computer power, more realistic and detailed form of mantle convection and plate tectonics will be tackled in the near future; thus, it is beneficial to investigate the toroidal/poloidal ratio and its spectrum that can be compared with the observed plate motion from the global to a finer scale. Moreover, owing to the improvement of the observation method about the plate geometry and configuration, we can attempt to comprehend the relationship between the geometry and the toroidal-poloidal power, which is still poorly understood. For these reasons, this study first conducts spherical harmonic expansion to higher degrees than ever in Section 2 and tries to understand the relationship between the plate geometry and toroidal/poloidal ratio in Section 2.1 and Appendix C.

1.3   Driving forces of plate motion

During the development of theory of plate tectonics, first, a drag force applied to the bottom of plate had been thought to be the primary force of plate motion and continental drift, as was originally proposed by Holmes (1928), and later suggested by numerical simulation of mantle convection (e.g., see Turcotte and Oxburgh (1972) for review). In other words, mantle convection and its near-surface horizontal flow actively drive the plates on the surface. On the other hand, several studies suggest that the plate motions are

not driven by basal drag: e.g., Oldenburg and Brune (1972) suggest that the plates are pull apart passively based on the morphological features of spreading ridge and fracture zones at mid-ocean ridges, and McKenzie and Bickle (1988) show that the thermal structure beneath mid-ocean ridges implies no "hot plume" from depth instead the mantle are dragged by the plate motion to cause passive mantle upwelling at mid-ocean ridges that may subduct as in the Chile triple junction.

Of the studies concerning the driving forces of plate motion, Forsyth and Uyeda (1975) have found that there is a correlation between the length of subduction zone and the speed of the plate motion and investigated the relative importance of forces applied to the plates, as is schematically illustrated in Figure 1.2. They concluded that the slab pull force is approximately one order higher than the other forces. This notion supports the "passive origin" of mid-ocean ridge as stated above. More than 25 years later, Becker and O'Connell (2001) re-examined the driving forces of plate motion in a similar manner to Forsyth and Uyeda (1975) but with updated data for plate motions based on improved methods, including estimates of slab-pull force using seismic tomographic images. However, their main conclusion is the same as in Forsyth and Uyeda (1975), i.e., the slab pull force generally can account for the observed plate motions. For example, Figure 1.3 from Becker and O'Connell (2001) shows that for the major plates, including the Pacific, Australia, Nazca, Philippine Sea and Cocos plates, the calculated torque solely by slab pull (torque: orange star; the direction of straight motion: line with orange diamond in the figure) may reproduce the observed Euler pole (Euler pole: light-blue star; the direction of straight motion: upward light-blue vector) reasonably well. However, for the Philippine Sea and Cocos plate, which demonstrate clear spin motion as will be discussed later, the slab pull force (line with orange diamond) broadly explains the observed "straight" motion (upward light-blue vector) although the observed spin motion of the Philippine Sea plate
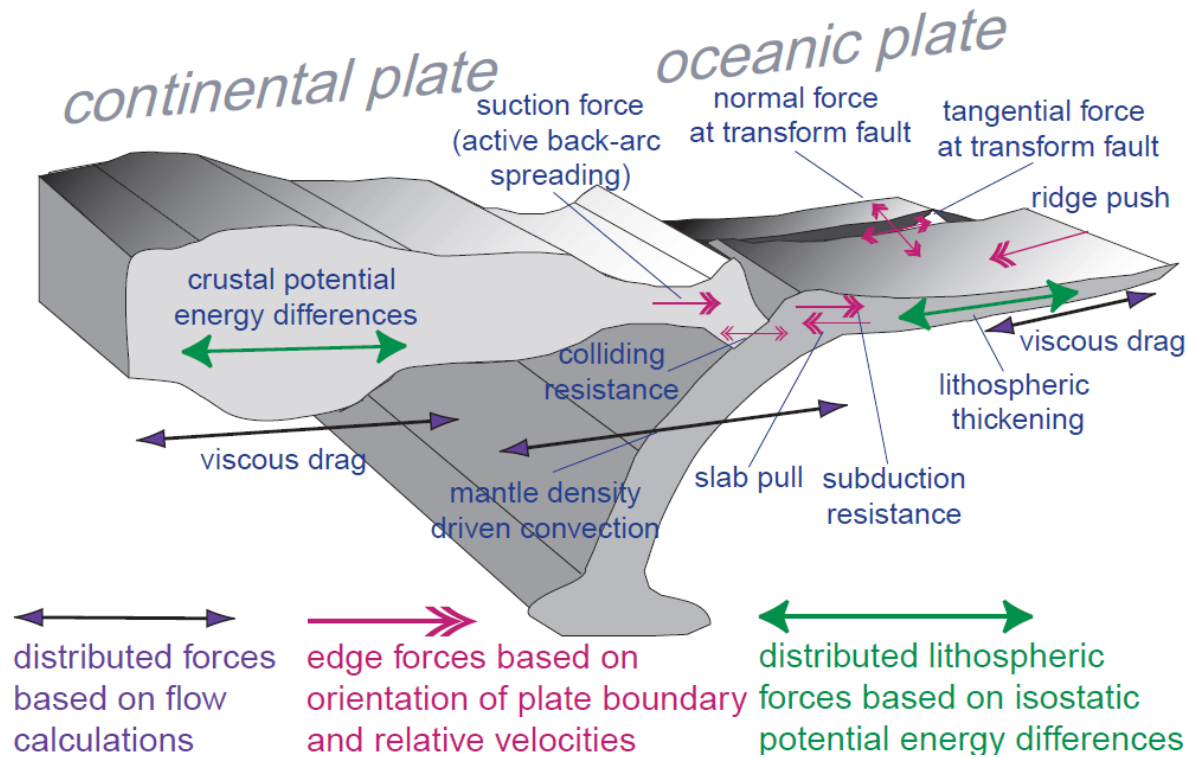
Fig. 1.2   Forces acting on plates from Becker and O'Connell (2001).

and the Cocos plate (light-blue two arc segments) cannot be accounted for by the slab pull

force or any other forces raised in their analyses. Forsyth and Uyeda (1975) and Becker

and O'Connell (2001) focused on the major plates and only the primary force for the plate

motion, and as a result they have not discussed the origin of the spin motions.

It is noted that Forsyth and Uyeda (1975) as well as Becker and O'Connell (2001) have

estimated the relative importance of driving forces in terms torque balance in which the

plate spin motion is naturally involved. Nevertheless, the plate spin motion has not been

considered as is partly expressed in their conceptual Figure 1.2 as if the surface toroidal

motion can be neglected. This indicates that, although spin motion is not negligibly small

even for several major plates, unless we specifically aim at analyzing the spin motion, it

could be hidden behind the major configuration consisting of slab-pull, straight motion

and spreading ridge. In addition, as will be shown later, small plates exhibit more signif-
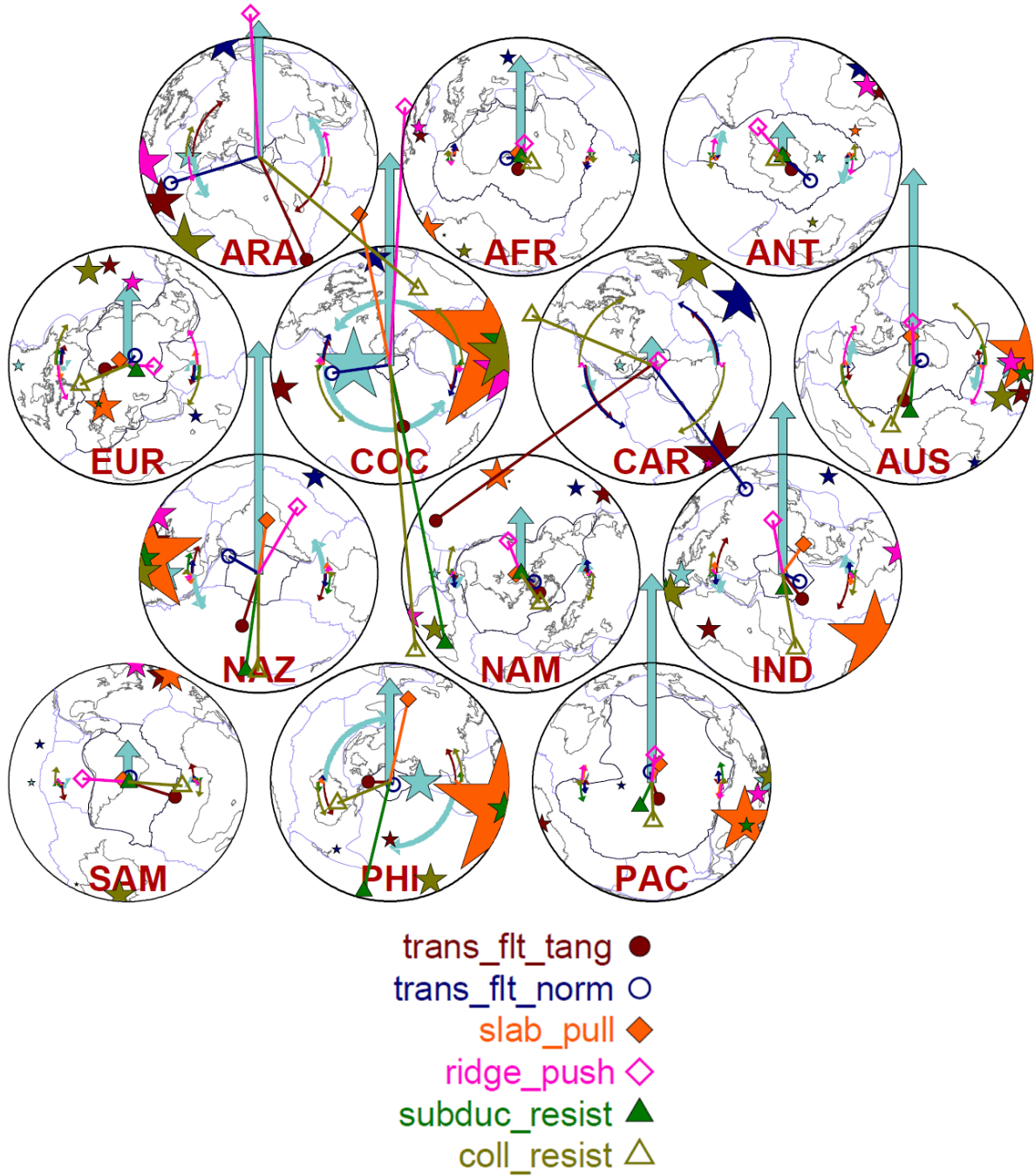
Fig. 1.3   Torque analysis from Becker and O'Connell (2001). Three letters represent:
AFR, Africa; ANT, Antarctica; ARA, Arabia; AUS, Australia; CAR, Caribbean; COC, Co-
cos; EUR, Eurasia; IND, India; NAM, North America; NAZ, Nazca; PAC, Pacific; PHI,
Philippines; and SAM, South America. Stars represent the location of the observed Euler
pole (light-blue) or the calculated torque (brown: transform fault tangential, dark-blue:
transform normal, orange: slab pull, pink: ridge push, green: subduction resistance,
bronze yellow: colliding resistance). Lines and a pair of circular vectors represents the
straight and spin motion components, respectively. The size of star and the length of
the line and the circular vector show the magnitude of the value.

icant spin motions, and it is necessary to include not only the major plates but also the small plates into the analyses of plate motion, in order to envisage the whole picture of driving forces of plate motion.

In spite of these difficulties, there are a few previous works that have discussed the spin motions of a large plate (Seno, 2000) or a small plate (Schouten et al., 1993). Seno (2000) has discussed the driving force of clockwise spin motion of the Philippine Sea plate. Seno (2000) attributed the driving force to mantle upwelling off the west coast of Kyushu, which is suggested by the crustal stress variation (Seno, 2000), the electrical conductivity (Shimoizumi et al., 1997; Handa, 2005) and seismic observations (Sadeghi et al., 2000; Yoshizawa et al., 2010) in the Kyushu region. Seno (2000) also suggested that the estimated magnitude of the torque caused by the upwelling may not be sufficient to simulate the observed plate spin motions and another driving force might be necessary. Regarding the spin motion of small plates, Schouten et al. (1993) observed the bathymetry and the magnetic anomaly of a micro plate in southeastern Pacific, the Easter plate, and discussed the history of the plate motion in the last several million years, which involves the present-day clockwise spin motion. They argued the relative motions between the adjacent plates, the Pacific plate and the Nazca plate, and the kinematics among those three plates. Whereas they pointed out that the interaction between these neighboring plates drives the spin motion of micro plate like a gear, they did not estimate either the force balance or the actual stress required for the spin motion.

Based on these improved data and new plate models including Bird (2003) and Kreemer et al. (2014), we globally investigate the driving force and mechanism of plate spin motions that have not been assessed in the previous works. Our analyses are different from the previous studies mainly in the following two points.

First, unlike the previous studies on driving forces of plate motion (Forsyth and Uyeda

(1975) and Becker and O'Connell (2001), who have consolidated the primary importance of slab-pull force), we focus on the spin motion of plates and its driving force. Secondly, we include small plates in our analysis, most of which exhibit significant spin motions as will be demonstrated. The smallest plate Forsyth and Uyeda (1975) coped with is the Cocos plate (or the Caribbean plate) and their size is approximately 2000 km in diameter. Many of the plates they analyzed do not exhibit significant spin motions. For this reason, even if Forsyth and Uyeda (1975) focused on plate spin motions, they would not have been able to discuss the driving force of plate spin motion. In contrast, our study adopts detailed plate configuration and motions based on the improved observations (Bird, 2003; Argus et al., 2011; Kreemer et al., 2014) which also allow us to exclude the "orogens" or "deformation zones" that complicate the analysis of plate motion.

As a result, focusing on the plate spin motions based on the detailed plate models, our study may contribute to a step-forward understanding of the driving forces of plate motion.

Chapter 2

Toroidal-poloidal analysis

First, we performed a spherical harmonic expansion of the plate velocity field (e.g., Hager and O'Connell, 1978). (Concerning the condition of the toroidal-poloidal decomposition, please refer to Appendix A.1 "Condition of Toroidal-Poloidal Decomposition".) Plate boundaries (which include a narrow deformation zone) are key to the characterization of plate motions (Gordon, 2000; Bercovici, 2003), therefore, we used the high-resolution plate model of Bird (2003) (PB2002), which includes 52 plates defined by topography, volcanism, magnetic anomalies, moment tensor solutions and geodesy (Figure 1.1 and Table 3.1 and 1.1). Then, we prepared a detailed global dataset at a resolution of 0.1° (Figure 2.1), and, based on a hotspot reference frame (Gripp and Gordon, 2002), we calculated the toroidal-poloidal components for spherical harmonic degrees that were higher than those performed in previous studies ($l = 1000$; i.e., to a resolution of ~ 20 km), by developing a new code that utilizes the parity of spherical harmonics (Appendix A and B, especially B.3).

The ratio $\gamma(l)$ of the toroidal power $\sigma_T(l)$ to the poloidal power $\sigma_P(l)$ is calculated as

$$\gamma(l) = \frac{\sigma_T(l)}{\sigma_P(l)} = \sqrt{\sum_m c_{lm} c_{lm}^*} \bigg/ \sqrt{\sum_m b_{lm} b_{lm}^*}, \tag{2.1}$$

where c_{lm} and b_{lm} represent the toroidal and poloidal coefficients of the velocity fields, respectively, and the asterisk denotes the complex conjugate. Note that the first degree
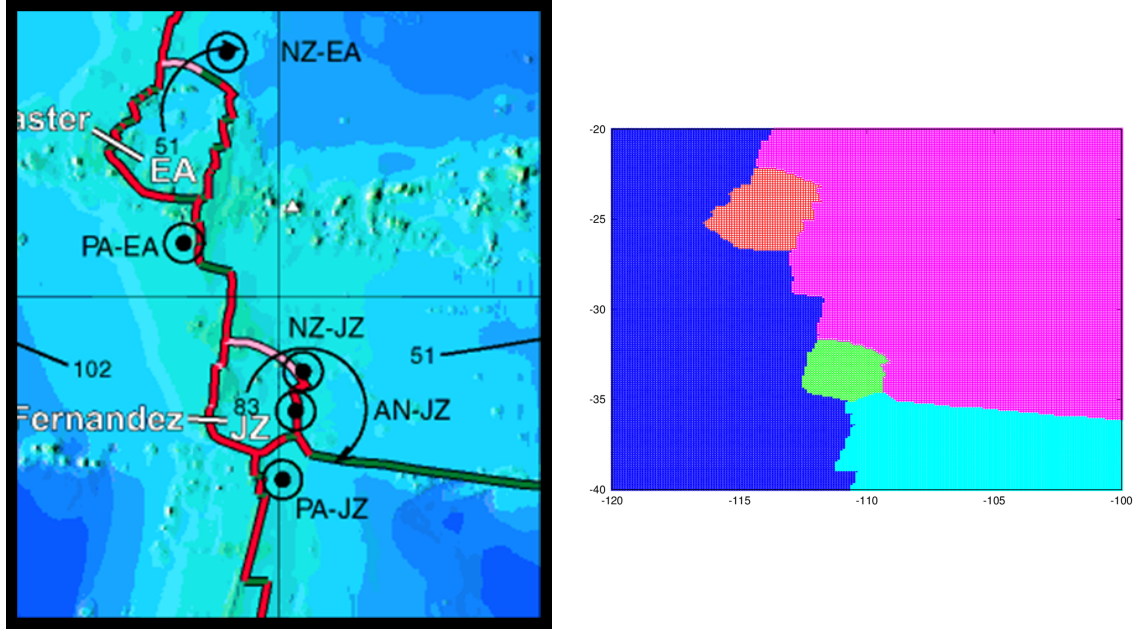
Fig. 2.1   Digitization of plate configuration of PB2002. For plate analysis, we digitized the original plate configuration data of PB2002 (Bird, 2003) (left figure: an example area from 100° W to 120° W and from 20° S to 40° S) into the digital plate data at a resolution of 0.1° (right figure: the corresponding area).

term in the toroidal expansion corresponds to the net rotation of the lithosphere, which depends on an absolute reference frame; we therefore do not discuss this term in this study.

The result of the spherical harmonic expansion is shown as a blue line in Figure 2.3 (and the power spectra in Figure 2.2). Although O'Connell et al. (1991) argued that the ratio of the amplitude of the toroidal to poloidal spectra is nearly constant for $l < 32$ (at ~0.8), our new result, applicable to higher harmonics, shows that the amplitude ratio broadly trends towards higher values for $l > 20$, which corresponds to a scale < 1000 km, and is demonstrated by the approximate lines in Figure 2.3.

To estimate the error of this result, caused by the uncertainties in plate motions, we calculated the toroidal/poloidal ratio of another plate model, NNR-MORVEL (Argus et al., 2011) (Figure 2.4). The result is indicated by the red line in Figure 2.3 and demonstrates that there is only a little difference in the toroidal/poloidal ratio between the plate models,
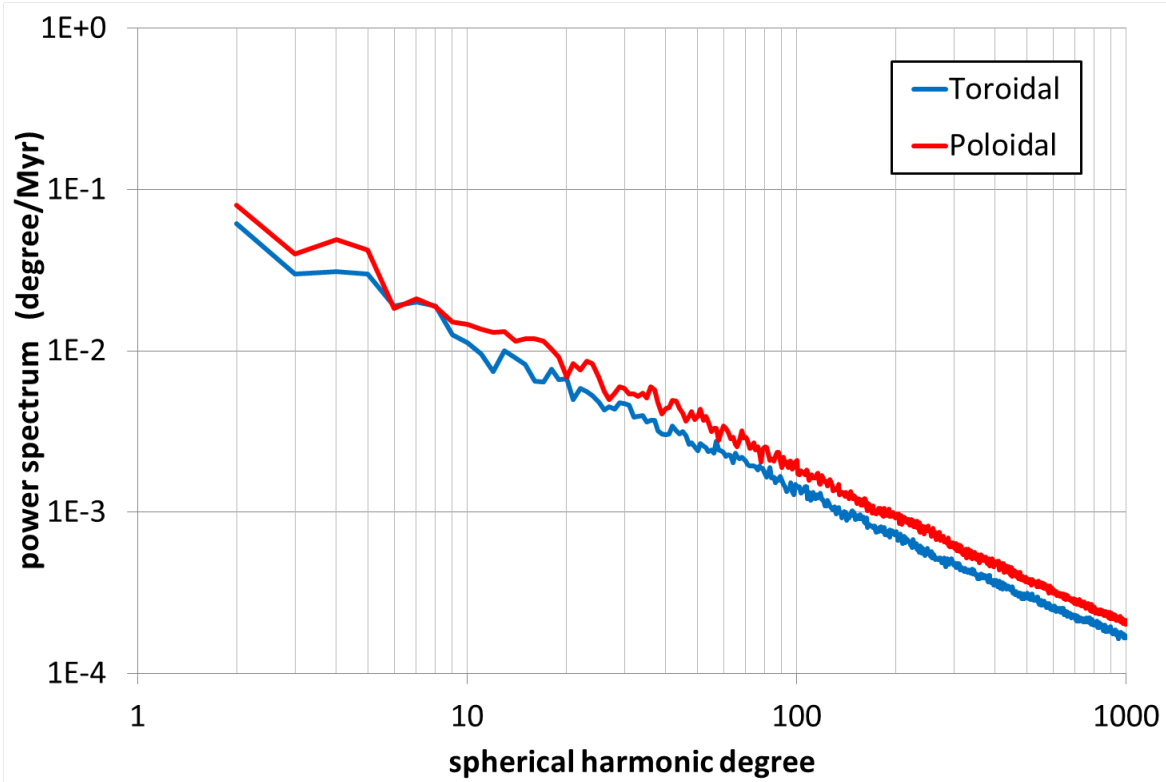
Fig. 2.2   Toroidal-poloidal power spectrum. The blue and red lines represent spectra for toroidal power and poloidal power of the plate model PB2002 (Bird, 2003), respectively.

indicating that the error of plate motion in a plate model is negligible and the trend of toroidal/poloidal ratio in this analysis is robust.
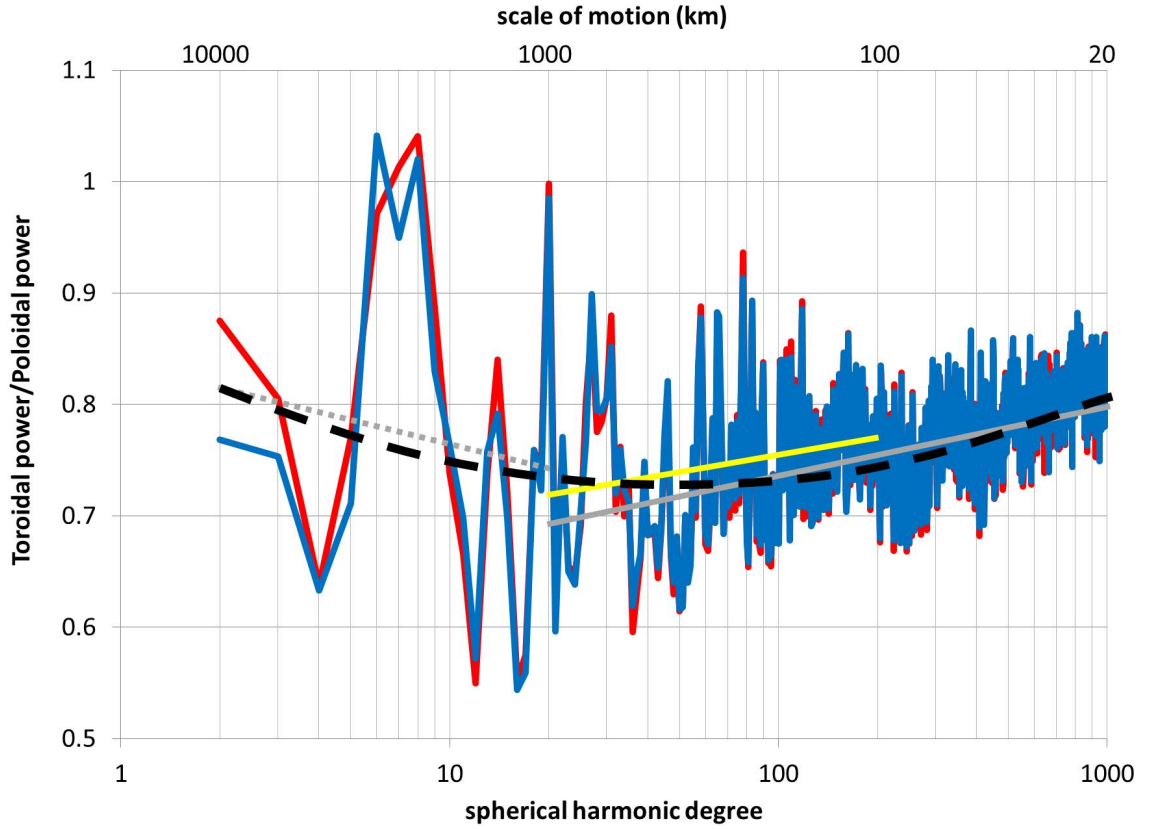
Fig. 2.3 Ratio of toroidal to poloidal power as a function of spherical harmonic degree. The blue and red spectra represent the ratios of the plate model from PB2002 (Bird, 2003) and NNR-MORVEL (Argus et al., 2011), respectively. The upper horizontal axis shows the scale of motion corresponding to the spherical harmonic degree. There are four logarithmic trendlines to fit the data of PB2002: the broken black line is the quadratic fitting curve for the whole spectrum, the yellow line is the linear fitting line for the range from 100 km to 1000 km in the scale of motion, and the gray dotted and solid lines represent linear fitting lines for $l < 20$ (> 1000 km) and $l > 20$ (< 1000 km), respectively. The range for the yellow line (100–1000 km) might be related to the analysis of individual spin motion and the driving force (Figure 3.3 and 3.5). The ratio of total toroidal power to total poloidal power ($l = 2, 3, \ldots, 1000$), γ, is 0.753 for PB2002.
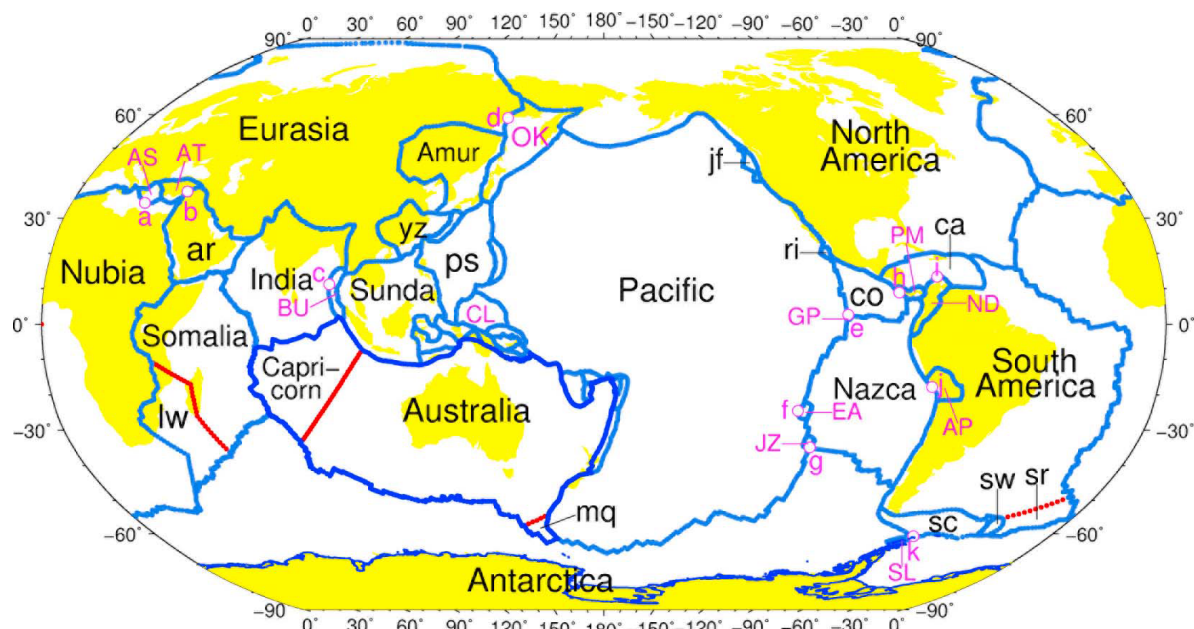
Fig. 2.4 The 56 plates of plate model NNR-MORVEL from Argus et al. (2011). Blue and red lines represent the plate boundaries. Capricorn, lw (Lwandle), mq (Macquarie) and sr (Sur) are new plates added to PB2002 (Bird, 2003) listed in Table 3.1.

2.1   Effect of plate geometry on the toroidal/poloidal ratio

Although toroidal and poloidal components represent the vorticity and the divergence/convergence of plate motions, respectively, yet not only plate motions but also plate geometry affects the ratio. As a previous work about the effect of plate geometry on the toroidal/poloidal ratio, Olson and Bercovici (1991) demonstrated that the aspect ratio of a plate (i.e., the ratio of the plate length along the plate motion L_p to the plate length normal to the motion L_n) has the following relationship with the toroidal/poloidal kinetic energy ratio γ:

$$\gamma \sim \left(\frac{L_p}{L_n}\right)^2. \tag{2.2}$$

Olson and Bercovici (1991) showed that there is a correlation between the plate aspect ratio and the induced toroidal/poloidal ratio in the 2D ideal square plate model. We here look at the effect of the plate geometry upon the toroidal/poloidal ratio to grasp the complex relationship between them. We impose straight or spin motion on a plate with an ideal geometries, circle or square. Accordingly, there are four simple examples: (a) a circular plate with a pure spin motion (left side of Figure 2.5), (b) a circular plate with a pure straight motion (right side of Figure 2.5), (c) a square plate with a pure spin motion (left side of Figure 2.6) and (d) a square plate with a pure straight motion (right side of Figure 2.6). In this model, we utilized the same-magnitude Euler pole (1°/Myr) and put it at the center of the plate to generate spin motion and at the North pole to generate straight motion. We calculate the power of toroidal-poloidal spectra to 100 degrees and the result is Figure 2.5 and 2.6. Whereas the circular plate with a pure spin motion possesses a dominant toroidal component and almost negligible poloidal component, the square plate with a pure spin motion demonstrates almost same toroidal-poloidal component or little higher poloidal component than toroidal one since the pure spin motion gen-

erates divergence and convergence motion along the plate boundary, indicating that the roundness of the plate geometry affects the toroidal/poloidal ratio. However, in the case of straight motion, the effect of roundness almost vanishes. It means that not a single effect but combination of effects including plate geometry and motion determine the toroidal-poloidal power and the ratio. It is true that the relationship is intricate, this result, especially the result of spin motions, clearly shows that the length of divergent or convergent plate boundary and that of transform fault are vital in toroidal/poloidal ratio. Based on this general result, we then analyze the effect of size, aspect ratio, roundness of the plate and we also compile the number of subduction zone, ridge and transform fault with those length in PB2002 in Appendix C.
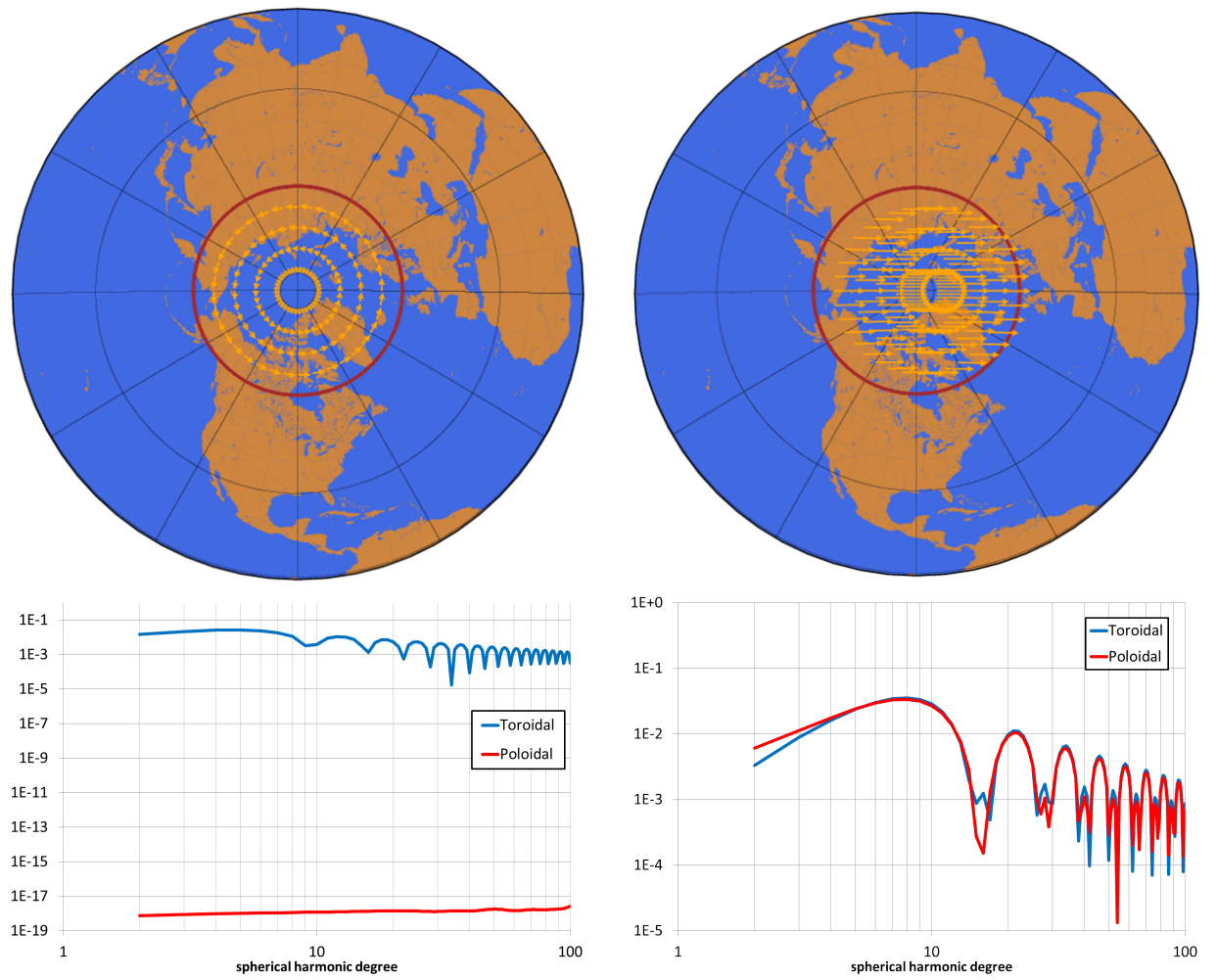
Fig. 2.5   Top: red line and orange vectors represent a model plate boundary and an imposed plate motion, respectively; bottom: blue and red lines show the toroidal and poloidal power induced by the plate motion, respectively. Left: a circular plate with a pure spin motion; right: a circular plate with a pure straight motion.
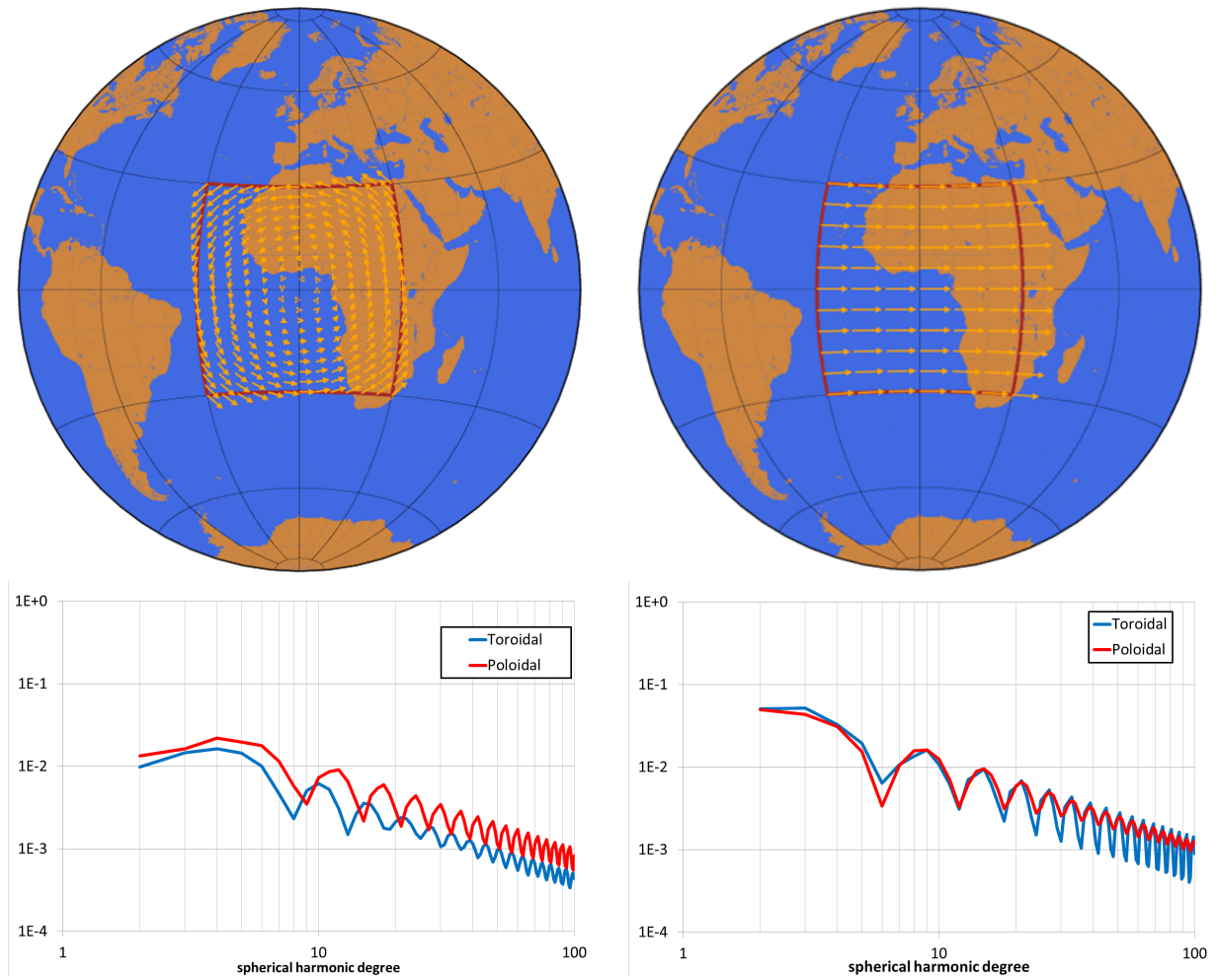
Fig. 2.6   Left: a square plate with a pure spin motion; right: a square plate with a pure straight motion. As for the explanation of the figure, please refer to Figure 2.5

2.2 Summary

The major aim of this chapter is the general comprehension of the toroidal/poloidal feature, particularly in high spherical harmonic degree, for which we conducted a detailed spherical harmonic expansion for the high-resolution plate models. With the detailed plate models, PB2002 and NNR-MORVEL, our result demonstrates the increase in toroidal/poloidal ratio at higher degrees for the first time. Although the toroidal/poloidal ratio are commonly used as a benchmark in a numerical simulation of a mantle convection (Tackley, 2000a,b; Richards et al., 2001) based on the notion that the toroidal/poloidal ratio is almost constant irrespective of spherical harmonic degrees. However, our result clearly demonstrates that the ratio is not constant, instead the spectrum should be examined. This new notion will be useful for those numerical simulations of mantle convection to understand plate tectonics-like motions through the comparison with our result, i.e., the increase in the ratio at high spherical harmonic degrees from approximately $l > 20$.

Whereas the increase in the toroidal/poloidal ratio is relevant to the plate motions and the configuration, the quantitative comprehension of the relationship is not trivial since all the effects associated with plate configuration and the motion are not independent but convoluted. However, in order to grasp the geometrical effect on the toroidal-poloidal power, we calculate toroidal/poloidal ratios with various geometries in Section 2.1 and Appendix C, which would also help to understand the nature of plate motion and the global toroidal/poloidal aspect, in both actual data and the numerical results.

Chapter 3

Driving force of plate spin motion

3.1 Division of plate motions

With the finer plate motion data than ever, we explore the driving force of plate spin motion. To contemplate the force of plate spin motion, we first extract spin motion of every individual plate from their observed motions. Hence, we divided plate motions into two types, spin motion and straight motion. To obtain the spin and straight motions of individual plates, we divided the Euler vector of each individual plate into two components: a vector that passes vertically through the geometric center of the plate, which is related to the spin motion and has a magnitude (i.e., angular velocity) defined as ω_C, and a vector perpendicular to the first vector, which passes through the Earth's center and is related to the motion along a great circle, and whose magnitude is defined as ω_G (Table 3.1). Since previous works have already suggested an active spin motions of a small plates (e.g., Schouten et al., 1993) and detailed plate model PB2002 can exhibit plate motions of such a small scale, we plots of ω_C and ω_G as functions of plate size (Figure 3.1). Figure 3.1 shows that ω_C generally decreases with increasing plate size, whereas ω_G is roughly constant between 0.1 and 1°/Myr. As a result, for plate sizes less than ∼ 1000 km, the difference between ω_C and ω_G is large (Figure 3.1). Based on these differential variations, we discuss the mechanisms and their corresponding force balance for the plate spin motions.
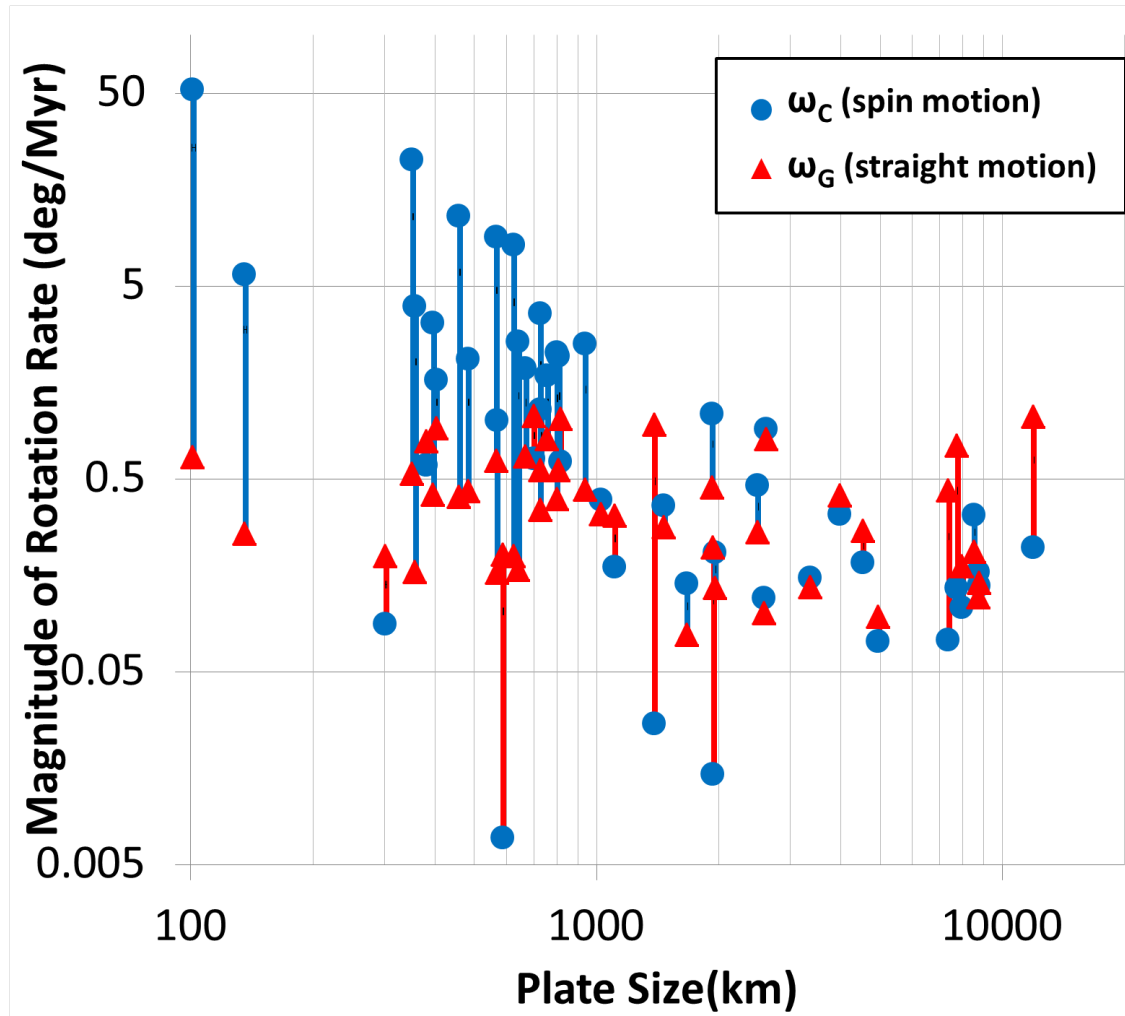
Fig. 3.1   Plate spin (ω_C) and straight (ω_G) motions as a function of plate size. Blue circles and red triangles represent ω_C and ω_G, respectively. The vertical lines between blue circles and red triangles connect a ω_C, ω_G pair for each plate, and the color of the line indicates a larger component of either ω_C (blue lines) or ω_G (red lines).

Table. 3.1 List of the plates and parameters for PB2002 in a hotspot reference frame. The plates in green cells and blue cells represent those containing orogen (deforming zone) and subduction zone as identified in PB2002 (Bird, 2003), respectively. In order to transform the data in the Pacific fixed frame, which PB2002 and GSRM v2.1 (Kreemer et al., 2014) originally use, to those in the hotspot reference frame, we have added the Euler vector of the Pacific plate (Gripp and Gordon, 2002). We also plot the data in no-net-rotation reference frames in Figure 3.3 and 3.5, based on NNR-MORVEL (Argus et al., 2011) and a part of the data from GSRM v2.1 expressed in a no-net-rotation reference frame (Appendix of Kreemer et al. (2014)). It is noted that, although GSRM v2.1 is mainly based on GPS data, the difference in plate spin motion among the three plate models is small as is discussed in this study. ★1: an excluded plate in Figure 3.3, 3.5, 3.8 and C.14. ★2: an excluded plate in Figure 3.3, 3.5 and 3.8. ∗: plate in deforming zones in GSRM v2.1 (Kreemer et al., 2014). †: positive and negative values mean counterclockwise and clockwise spin motions, respectively.

Plate Name	Abbreviation	Area (sterradian)	longitude (deg)	latitude (deg)	Rotation rate (deg/Ma)	Aspect ratio	(Lx/Ly)^2	ωG (deg/Myr)	ωC (deg/Myr)	ωC (deg/Myr)(†)	|ωC| (deg/Myr)	Plate Size (km)	Note
Amur	AM	0.1307	125.5994	46.1353	0.1553	1.6999	2.8897	0.0992	-0.1194	-0.1194	0.1194	2603	
Altiplano	AP	0.0205	-69.3627	-17.3932	0.5044	0.9432	0.8896	0.3251	0.3857	0.3857	0.3857	1029	*
Arabia	AR	0.1208	46.9935	23.6617	0.5270	1.7196	2.9570	0.2616	0.4575	0.4575	0.4575	2502	
Banda Sea	BS	0.0172	125.7963	-4.8658	2.5106	0.2214	0.0490	0.4358	2.4725	2.4725	2.4725	942	*
Burma	BU	0.0127	93.9626	8.9340	2.2091	3.1893	10.1717	0.5476	-2.1401	-2.1401	2.1401	810	
Easter	EA	0.0041	246.0617	-24.5666	11.4154	0.7466	0.5574	0.4003	-11.4083	-11.4083	11.4083	461	
Eurasia	EU	1.1963	58.2175	59.0394	0.2047	1.0784	1.1629	0.1745	0.1070	0.1070	0.1070	7992	
Galapagos	GP	0.0004	258.3357	1.9101	5.7036	0.8523	0.7264	0.2575	-5.6978	-5.6978	5.6978	136	
Juan Fernandez	JZ	0.0024	249.0957	-33.3961	22.3832	1.2752	1.6262	0.5266	-22.3770	-22.3770	22.3770	353	
Kermadec	KE	0.0125	180.6289	-33.0077	2.2652	1.6126	2.6004	0.3888	-2.2316	-2.2316	2.2316	802	*
Mariana	MA	0.0104	145.4523	17.8752	1.2627	0.9988	0.9975	0.5483	1.1374	1.1374	1.1374	732	
Manus	MN	0.0002	150.4469	-3.5286	51.6116	1.1007	1.2115	0.6417	51.6076	51.6076	51.6076	102	*
Maoke	MO	0.0028	138.0412	-3.4338	0.9678	0.5008	0.2508	0.7737	0.5814	0.5814	0.5814	383	*
North America	NA	1.3656	-85.9660	57.9100	0.3835	0.6498	0.4223	0.2081	-0.3222	-0.3222	0.3222	8560	
North Andes	ND	0.0239	-75.1636	6.4591	0.3629	0.7421	0.5507	0.3187	-0.1735	-0.1735	0.1735	1112	*
Niuafo'ou	NI	0.0031	184.2662	-16.6740	3.2220	0.5425	0.2944	0.4081	3.1960	3.1960	3.1960	398	
Okhotsk	OK	0.0748	148.9950	51.3285	0.2454	0.3391	0.1150	0.1346	-0.2052	-0.2052	0.2052	1968	
Okinawa	ON	0.0080	127.9723	27.3787	2.5439	0.8346	0.6965	0.1672	2.5384	2.5384	2.5384	644	
Panama	PM	0.0067	-81.1084	8.9424	0.1998	3.1109	9.6780	0.1997	-0.0068	-0.0068	0.0068	590	
Rivera	RI	0.0025	252.6082	20.0096	3.8881	1.0037	1.0073	0.1633	3.8847	3.8847	3.8847	359	
South Bismarck	SB	0.0076	148.7584	-5.0247	8.0525	0.7718	0.5958	0.1975	-8.0501	-8.0501	8.0501	628	*
Scotia	SC	0.0419	-50.4448	-57.2733	0.4549	1.6213	2.6285	0.2777	0.3603	0.3603	0.3603	1472	
Shetland	SL	0.0018	-58.9628	-61.9103	0.2151	2.3023	5.3006	0.1966	0.0872	0.0872	0.0872	303	
Somalia	SO	0.4719	48.4623	-13.0904	0.1192	0.9390	0.8817	0.0955	0.0714	0.0714	0.0714	4969	
Sandwich	SW	0.0045	-27.3949	-57.7719	2.1207	0.6234	0.3886	0.4291	2.0768	2.0768	2.0768	484	
Timor	TI	0.0087	125.7853	-8.6973	1.9539	0.2116	0.0448	0.6473	1.8436	1.8436	1.8436	671	*
Tonga	TO	0.0063	185.5500	-19.5057	8.9185	0.5618	0.3156	0.6145	-8.8973	-8.8973	8.8973	568	
Yangtze	YA	0.0543	116.1746	27.2661	0.1617	1.1617	1.3495	0.0766	0.1424	0.1424	0.1424	1675	
Accompanies subduction zone (PB2002)													
Africa	AF	1.4407	2.7972	-0.3702	0.1987	0.5843	0.3414	0.1430	0.1379	0.1379	0.1379	8801	★2
Antarctica	AN	1.4327	57.8220	-83.6032	0.2024	0.5349	0.2861	0.1206	0.1625	0.1625	0.1625	8776	★2
Australia	AU	1.1329	122.5524	-30.0032	0.7467	0.3592	0.1290	0.7346	0.1343	0.1343	0.1343	7771	★2
Birds Head	BH	0.0130	132.0359	-1.2503	1.1810	3.1578	9.9716	1.0115	0.6096	0.6096	0.6096	818	★2, *
Caribbean	CA	0.0730	-73.1960	15.0461	0.2196	3.1748	10.0795	0.2191	-0.0146	-0.0146	0.0146	1944	★2
Caroline	CL	0.0377	140.5311	3.1743	0.9482	1.8257	3.3330	0.9478	-0.0266	-0.0266	0.0266	1395	★2
Cocos	CO	0.0722	265.3846	8.3547	1.1621	0.5656	0.3199	0.4447	1.0737	1.0737	1.0737	1934	★2
India	IN	0.3064	77.5265	12.9913	0.5211	1.0859	1.1792	0.4074	0.3250	0.3250	0.3250	3995	★2
Juan de Fuca	JF	0.0063	232.4385	45.4255	0.1117	1.0131	1.0263	0.1609	-0.0988	-0.0988	0.0988	571	★2
Molucca Sea	MS	0.0103	123.5338	-1.1822	3.5820	1.6435	2.7011	0.3406	-3.5658	-3.5658	3.5658	730	★2, *
North Bismarck	MB	0.0096	148.5224	-2.4402	1.2242	3.4805	12.1137	1.0484	0.6320	0.6320	0.6320	703	★2
Nazca	NZ	0.3967	267.8410	-19.9015	0.3231	0.9588	0.9194	0.2672	0.1817	0.1817	0.1817	4551	★2
Pacific	PA	2.5769	202.7447	1.5806	1.0613	0.7815	0.6107	1.0385	-0.2190	-0.2190	0.2190	11974	★2
Philippine Sea	PS	0.1341	133.5124	18.3429	1.1198	0.8292	0.6875	0.7926	-0.8981	-0.8981	0.8981	2637	★2
South America	SA	1.0305	-46.2110	-21.5593	0.4358	0.7027	0.4938	0.0297	0.0726	0.0726	0.0726	7400	★2
Solomon Sea	SS	0.0032	152.5915	-7.2195	1.8422	0.6997	0.4895	0.9014	1.6066	1.6066	1.6066	405	★2
Sunda	SU	0.2197	111.0875	5.0221	0.2037	0.9350	0.8743	0.1360	-0.1516	-0.1516	0.1516	3379	★2
Woodlark	WL	0.0112	146.8990	-6.6110	1.8733	0.5093	0.2594	0.7987	1.6945	1.6945	1.6945	759	★2
Contains orogen (PB2002)													
Aegean Sea	AS	0.0079	25.0801	36.9215	0.4515	0.8918	0.7953	0.4464	-0.0682	-0.0682	0.0682	640	★1
Anatolia	AT	0.0142	32.9010	38.1892	1.1875	1.4583	2.1266	0.3485	1.1353	1.1353	1.1353	856	★1, *
Balmoral Reef	BR	0.0048	175.9764	-15.0746	0.8758	1.7677	3.1249	0.8294	0.2815	0.2815	0.2815	499	★1, *
Conway Reef	CR	0.0036	174.8188	-19.2054	3.9894	0.7422	0.5509	0.6632	3.9339	3.9339	3.9339	429	★1, *
Futuna	FT	0.0008	182.0526	-14.9751	5.1096	1.7339	3.0065	0.7317	5.0570	5.0570	5.0570	202	★1, *
New Hebrides	NH	0.0159	170.4681	-17.9497	2.5912	0.8197	0.6718	1.1587	-2.3177	-2.3177	2.3177	905	★1, *

3.2   Driving force of plate spin motion

The driving forces of plate motion are generally classified into three types (e.g., Forsyth and Uyeda, 1975; Becker and O'Connell, 2001) (Figure 1.2): body forces (e.g., slab-pull and ridge-push; hereafter expressed as T_{BD}), plate boundary forces (e.g., collision, suction, and shear forces between neighboring plates; T_{PB}), and resultant resistance forces (e.g., mantle drag and slab resistance; T_{RS}). Here, mantle drag (a component of T_{RS}) is treated as a resistive force rather than a driving force of plate spin motion, because the toroidal components in mantle convection are negligible (Hager and O'Connell, 1978) and are unlikely to excite the spin motion of plates. Of these, T_{BD}, in particular the slab-pull force, is the main driving force of the global plate system (Forsyth and Uyeda, 1975); T_{BD} contributes primarily to straight plate motion (Figure 1.3), whereas T_{PB} may cause spin motion when torque occurs around the center of the plate. However, the slab-pull force sometimes excites spin motion. One such example is the Cocos plate. Gorbatov and Fukao (2005) have shown that the northwestern part of the slab was torn away from the deeper Farallon slab. It induces the heterogeneity of the slab pull forces, including a strong northward force from the eastern part of the slab, which can lead to the observed counterclockwise spin motion. Another example is the Philippine Sea plate, which exhibits an active clockwise spin motion (Seno et al., 1993). (We consider the driving force through the shape of a part of the slab of the Philippine Sea plate in Chapter 4). Seno (2000) suggests that the spin motion results from the eastward mantle flow against the Philippine Sea slab subducted beneath the SW Japan-Ryukyu arc, which is indicated by the crustal stress variation (Seno, 1999), the electrical conductivity (Shimoizumi et al., 1997; Handa, 2005) and seismic observations (Sadeghi et al., 2000; Yoshizawa et al., 2010) in the Kyushu region. To exclude such complexities associated with slabs, we focused on plates without slabs (Table 3.1),

in which case the torque balance around the center of the plate can be described with relevant T_{PB} and T_{RS} forces, as discussed below.

We can express T_{PB} as the driving shear stress along a plate boundary σ_{PB} and the area receiving the stress S_{PB} as

$$T_{PB} = \sigma_{PB} S_{PB} R = \sigma_{PB} D_{PB} L_{PB} R = 2\pi\lambda\sigma_{PB} D_{PB} R^2 \tag{3.1}$$

where R is the plate radius, D_{PB} is the average depth of the plate boundary sustaining the shear stress, L_{PB} is the length of the plate boundary along which the driving force is applied, and λ is the ratio of L_{PB} to the total length of the plate boundary. In equation (3.1), we assume a planar plate for simplicity in the calculation of its radius and area (which does not affect the results significantly), and we can assume that the plate is circular rather than spherical shell because the difference in the result is not sufficiently significant (Figure 3.2), the length of the driving plate boundary is proportional to the plate size, and λ is constant. We also assume the presence of a low-viscosity layer (hereafter referred to as the asthenosphere) with constant Newtonian viscosity μ and thickness D_{RS}. Then, T_{RS} can be expressed as

$$T_{RS} = \int \sigma_{RS} r\, dS = \int_0^R \mu \frac{r\omega_C}{D_{RS}} 2\pi r^2\, dr = \frac{\pi\mu\omega_C}{2D_{RS}} R^4. \tag{3.2}$$

From the torque balance and equations (3.1) and (3.2), we obtain

$$\sigma_{PB} = \frac{\omega_C}{4\lambda D_{PB} D_{RS}} \mu R^2, \tag{3.3}$$

which indicates that σ_{PB} is proportional to R^2 and ω_C. In other words, equation (3.3) shows that (for a constant ω_C) as plate size increases (left to right in Figure 3.1), the driving shear stress increases such that it induces spin motion onto a larger plate.

In this context, ω_C of a slab-free plate, which is indicated by the blue circles in Figure 3.3, generally increases with decreasing plate size. Concerning the list of the plate utilized for this figure, please refer to Table 3.1. One notable feature in Figure 3.3 is the rapid change

2d/3d ratio of plate area
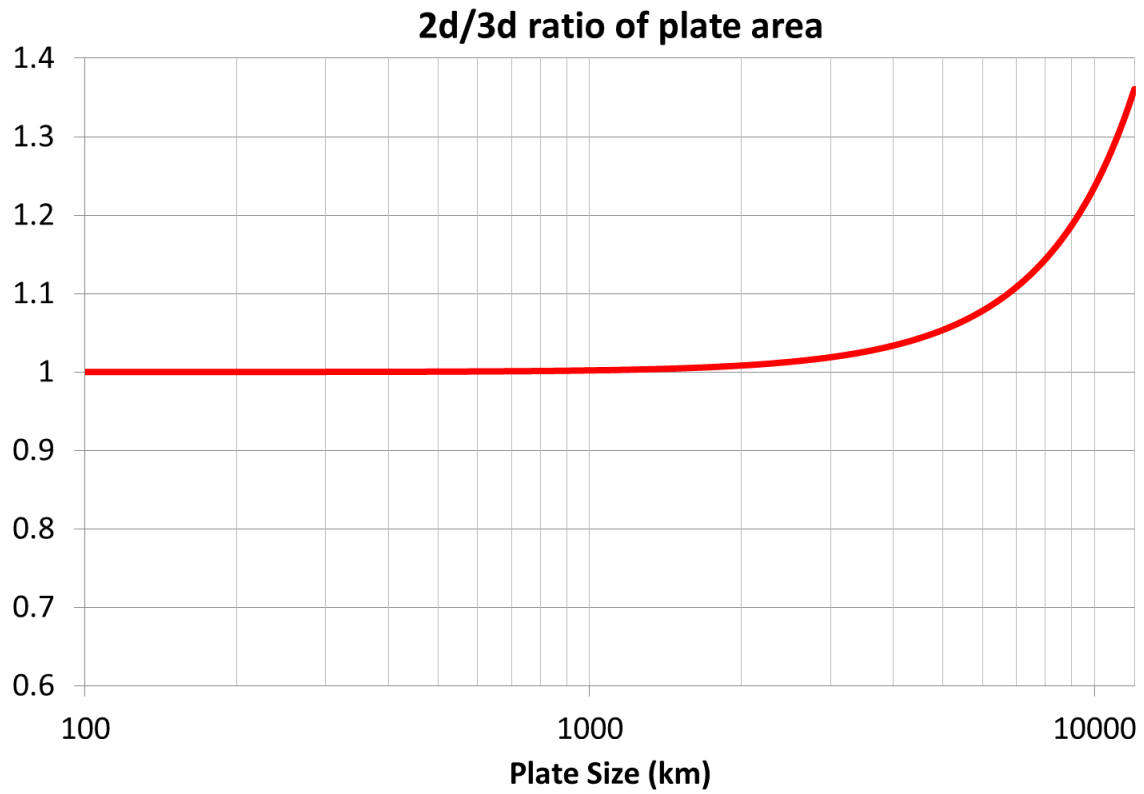
Fig. 3.2 $2D/3D$ ratio of plate area. This result shows that the areal difference is small; virtually none for plate size below 2000 km, which is the most important range in this study, and up to 25% difference even for the size of 10,000 km, having a negligible effect on the results and conclusions.

in ω_C around the critical plate size of ~ 1000 km: above the critical size, ω_C values are generally less than the average rotation rate of the global lithosphere (i.e., the net lithospheric rotation) (Ricard et al., 1991), of $\sim 0.43°$/Myr, as based on the hotspot reference frame utilized in this analysis (Gripp and Gordon, 2002); below the critical size, however, except for two plates, i.e., the Panama plate and the Shetland plate, the motions of which are not well-determined in PB2002 model, all ω_C values exceed 0.43 °/Myr.

It should be noted that the R-ω_C variation is not significantly affected by the choice of plate models as in Figure 3.3 (i.e., Pb2002 (Bird, 2003) (Figure 1.1), NNR-MORVLE (Argus et al., 2011) (Figure 2.4) and GSRM v2.1 (Kreemer et al., 2014) (Figure 3.4) that include both no-net-rotation and hotspot reference frames for the data acquired by several meth-
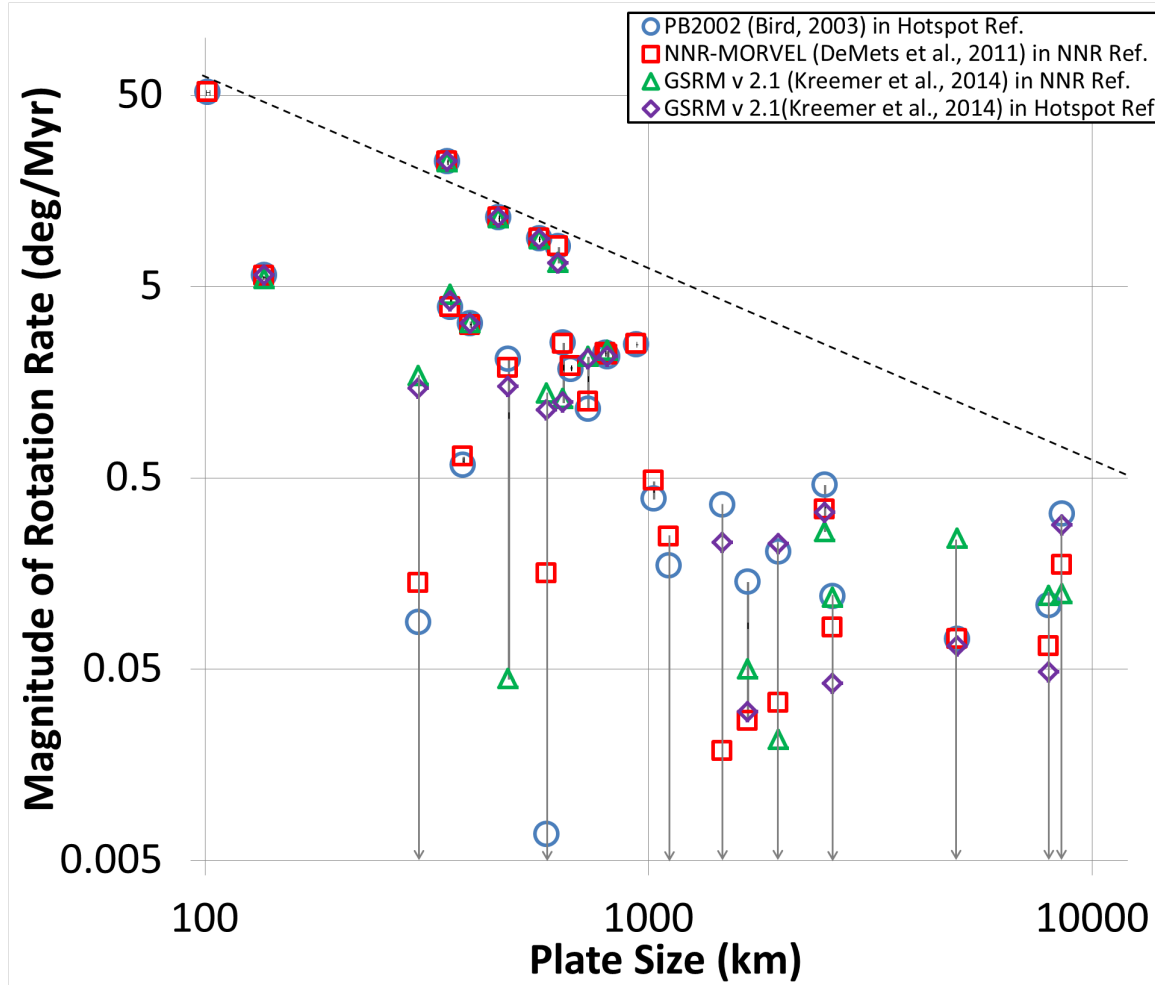
Fig. 3.3 Rotation rate and plate size. Blue circles, red squares, green triangles, and purple diamonds represent the data from three different models of PB2002 (Bird, 2003), NNR-MORVEL (Argus et al., 2011), GSRM v2.1 (Kreemer et al., 2014) in no-net-rotation, and hotspot reference frame, respectively (see Table 3.1 for the details). Vertical bars represent the difference in rotation rate of a plate among the three plate models and the downward arrows indicate that both clockwise and counterclockwise rotations occur depending on the plate models with different reference frames. The dashed line represents the expected rotation rate driven by the motion of the Pacific plate ($\sim$ 10 cm/yr).

ods representing different time-scales. see Table 3.1 for the details): i.e., almost all the large plates (plate size > 1000 km) show negligibly small ω_C less than the net-rotation rate (0.43°/Myr), and the rotation direction (clockwise or counterclockwise) of large plates varies depending on the reference frame chosen (as indicated by large error bars with downward arrows in Figure 3.3), whereas the large ω_C is seen only for small plates irre-
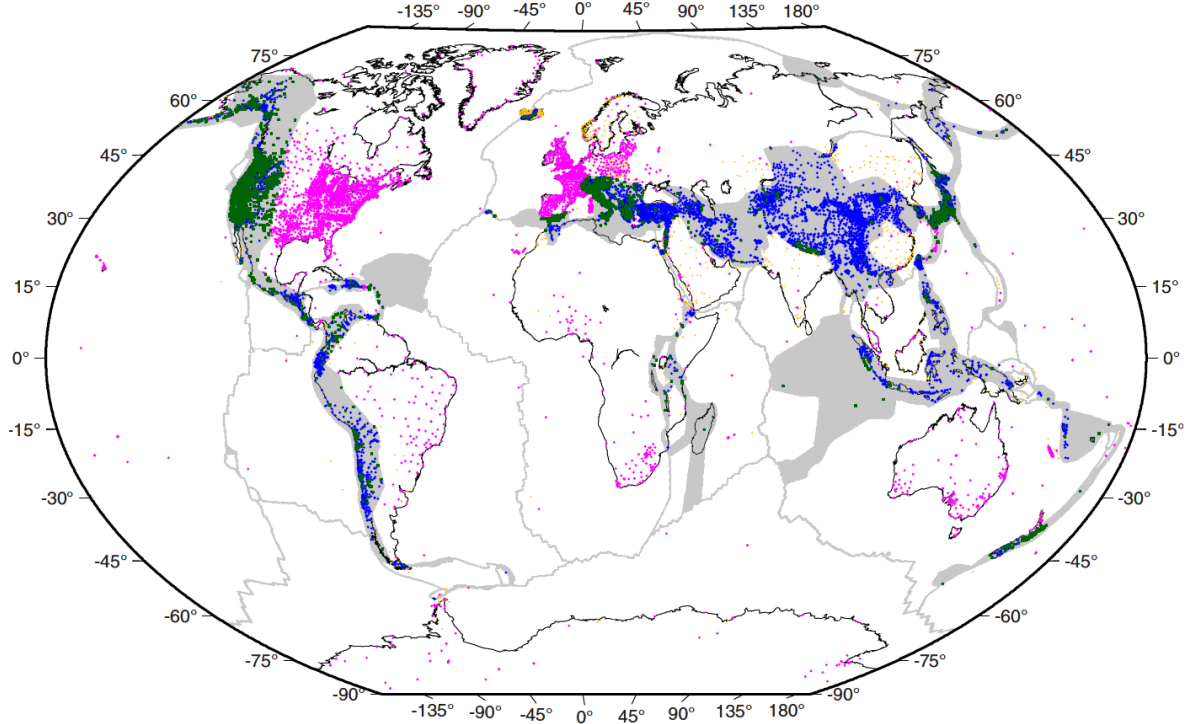
Fig. 3.4   The 50 plates of plate model GSRM v2.1 from Kreemer et al. (2014). Shaded areas represent the deformation zone, which we cannot deal with as a rigid plate.

spective of the chosen frame (Figure 3.3).

In Figure 3.3, the dashed line indicates the R-ω_C relation expected from the Pacific plate motion (i.e., assuming that a fast-moving plate drives the spin motion of the surrounding small plates via mechanical coupling at plate boundaries), which limits the upper bounds of high rate of the small plates. Within this context, there is a significant gap between the dashed line and ω_C of the plates larger than ~ 1000 km, indicating that a more rapid decrease in ω_C occurs around the plate size of ~ 1000 km than that expected from the dashed line. This may suggest a rapid change in the stress-strain-rate regime of plate boundary (e.g., yielding with viscoplastic rheology or shear weakening with pseudo-stick-slip rheology (Bercovici, 2003)).

In order to test such a possibility, we examine the relationship between R and σ_{PB} (the plate boundary shear stress driving the spin motion) based on equation (3.3) and observed
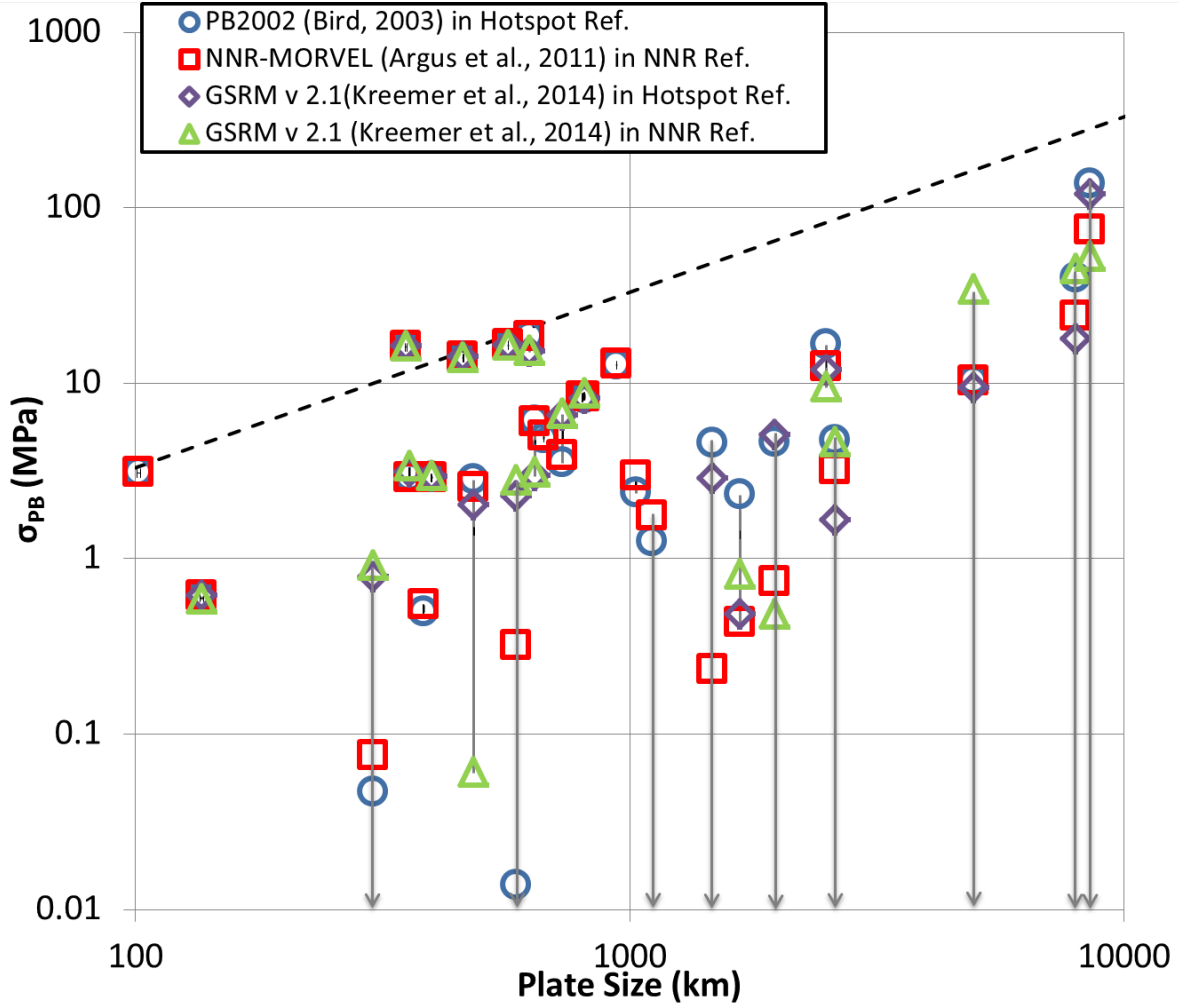
Fig. 3.5   The driving shear stress along a plate boundary σ_{PB} obtained from equation (3.3) as a function of plate size (=2R). The symbols and error bars are the same as in Figure 3.3. The dashed line is the expected driving stress induced by the motion of the Pacific plate (corresponding to the dashed line in Figure 3.3)

ω_C as shown in Figure 3.5, assuming $\mu = 10^{20}$ Pa s, D_{PB} = 40 km, D_{RS} = 60 km, and λ = 0.25. The uncertainties associated with these assumptions will be discussed later. It is worth noticing that σ_{PB} for plates with low rotation rates (the large plates, in general) have extremely large uncertainties, indicated by the error bars with downward arrows in Figure 3.5, and should be regarded as upper bounds.

The dashed line in Figure 3.5 represents the expected driving stress induced by the motion of the Pacific plate (corresponding to the dashed line in Figure 3.3), which limits

the upper bounds of σ_{PB} for the small plates; whereas for large plates, σ_{PB} is apprecia-bly lower than the prediction of the dashed line, indicating that rheological weakening or yielding operates on the boundaries of large plates, irrespective of the choice of reference frame (Figure 3.5).

For small plates (the plate size $<$ 1000 km, i.e., $R < 500$ km), the shear stress driving the spin motion increases with R (e.g., the dashed line in Figure 3.5), and above a critical size R_c, the stress becomes too large to transmit the stress across the boundary, causing rheological weakening or yielding. This critical stress is regarded as the strength of the plate boundary. From Figure 3.5, the critical stress is estimated to be $\sim 10 - 20$ MPa for plate sizes between $\sim 350 - 630$ km. Accordingly, the rotation rate of plates with $R > R_c$ is small as compared to the dashed line in Figure 3.3.

It can be confirmed that the spin rates of small plates are higher than those of large plates, which is the overall result, from Figure 3.6. Figure 3.6 shows that many small plates along the "sides" (i.e., along strike-slip boundaries) of large fast-moving plates have high spin rates with a rotation direction (clockwise or counterclockwise) consistent with the nearly straight motions of large plates that subduct along their margins. This mechanism has been suggested for several individual microplates (e.g., Schouten et al., 1993). Fig-ure 3.6, for example, demonstrates that in the southwestern Pacific, the Pacific plate (PA) excites spin motion of the Niuafo'ou plate (NI) and that the Australia plate (AU) induces spin motion of the Tonga plate (TO) and the Kermadec plate (KE). Along the East Pacific Rise, the Pacific plate and the Nazca plate (NZ) drive motions of the Easter plate (EA) and the Juan Fernandez plate (JZ). Although some of the abovelisted small plates, based on PB2002 plate model, are located within deforming zones identified by Kreemer et al. (2014) (shaded regions in Figure 3.4) and could be inappropriate to consider them as rigid plates to define the spin rate (e.g., KE), the overall configuration remains unchanged, including
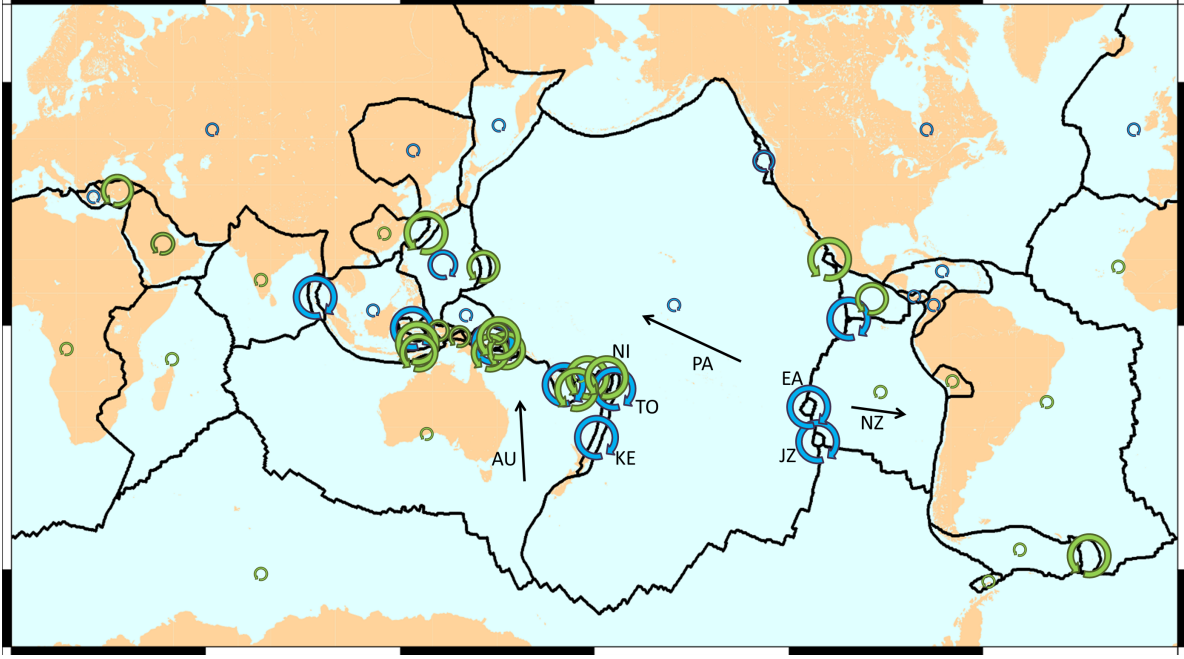
Fig. 3.6   Global geographical distribution of spin motion on a Mercator projection based on the plate model PB2002 (Bird, 2003). The blue and green curved vectors represent clockwise and counterclockwise spin motion, respectively. The radius of the vector is correlated with the rate of spin motion. Black vectors show the directions of plate motions of the Pacific plate (PA), the Australia plates (AU), and the Nazca plate (NZ). The two letters with each vector identify the plate, as follows. AU: Australia; EA: Easter; JZ: Juan Fernandez; KE: Kermadec; NZ: Nazca; NI: Niuafo'ou; PA: Pacific; TO: Tonga.

large spin motions of NI, EA, and JZ as shown in Figure 3.6.

These features, represented in Figure 3.6, suggest that although some regions (especially Southeast Asia) exhibit complex spin directions probably due to interactions among the small plates, the small islands and the intricate subduction zones, large fast-moving plates with subducting slabs induce spin motion in adjacent small plates through interactions along plate boundaries, which supports the idea presented above that T_{PB} drives the plate spin motions.

In addition, from equation (3.3) and Figure 3.5, we obtain a quantitative relationship between the viscosity of the asthenospheric mantle beneath the plates μ_a and the strength of the plate boundary σ_{st}. We substitute the constraints at the critical condition, as specified in Figure 3.5 (i.e., $\omega_C \approx 8°/\text{Myr}$, plate size ≈ 630 km and $\lambda \approx 0.25$, corresponding to the

South Bismarck Plate attaining the maximum σ_{PB}), and set $D_{PB} = 40$ km as the thickness of the plate boundary sustaining the shear stress (e.g., Kohlstedt et al., 1995). Then, we obtain the following equation,

$$\sigma_{st}(\text{MPa}) = \frac{1.1}{10^{17}} \frac{\mu_a(\text{Pa s})}{D_{RS}(\text{km})}, \tag{3.4}$$

which is the basis for Figure 3.7. There is an appreciable uncertainty with regard to the thickness of the asthenosphere beneath the oceanic plates, as it is dependent on the observational methods used for measurement (Karato, 2012); the asthenosphere is observed as a zone of low seismic velocity [e.g., ~ 120 km (Kawakatsu et al., 2009)], a high attenuation layer [e.g., ~ 140 km (Dziewonski and Anderson, 1981); ~ 60 km (Yingjie et al., 2007)] with significant seismic anisotropy [e.g., ~ 120 km (Beghein and Trampert, 2004)] and a high electrical conductivity layer [e.g., ~ 60 km (Evans et al., 2005)]. From these observations, we estimate the thickness of asthenosphere under the oceanic plates (D_{RS}) to be 60–140 km.

Equation (3.4) and Figure 3.7 impose several constraints on the plate-mantle dynamics. Substituting $\mu_a = 10^{21}$ Pa s, based on the representative viscosity of the upper mantle (Peltier, 1998), into equation (3.4), we obtain $\sigma_{st} = 78$–183 MPa for $D_{RS} \approx 60$–140 km. Considering a more realistic case and assuming a low-viscosity asthenosphere, which is estimated from post-glacial rebound, seismic data, and laboratory measurements as 10^{19}–10^{20} Pa s (e.g., Karato and Wu, 1993; Simons and Hager, 1997; Forte and Mitrovica, 2001), we substitute $\mu_a \approx 10^{19}$–10^{20} Pa s, which gives $\sigma_{st} \approx 0.78$–18 MPa. This estimate only considers the force along the fractional length of the plate boundary λ, as in equation (3.1). If we consider the resistive forces along the remainder of the plate boundary, with length $1 - \lambda$, we obtain

$$\sigma_{PB} = \frac{\omega_C}{4\lambda D_{PB} D_{RS}} \mu R^2 + \frac{1-\lambda}{\lambda} \sigma_R, \tag{3.5}$$

where σ_R is the average resistive stress along the plate boundary (which must be less than
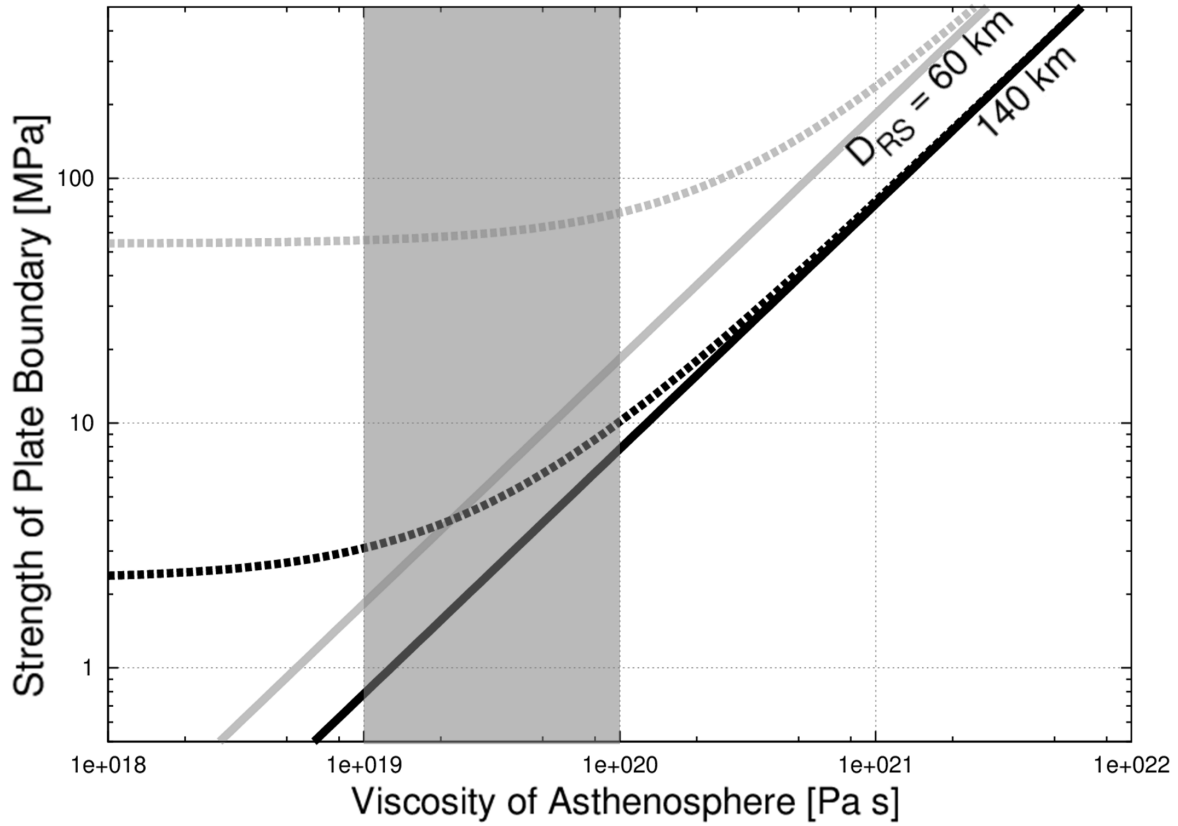
Fig. 3.7   Relationship between the strength of a plate boundary and the viscosity of
the asthenosphere. The solid black and gray lines are obtained from equation (3.4) for
D_{RS} = 140 and 60 km, respectively. The dotted black and gray lines are obtained on
the basis of equation (3.5), corresponding to the minimum and maximum estimates
for the strength of plate boundary, respectively. The shaded region shows the range of
viscosity of the asthenosphere estimated from postglacial rebound, seismic data, and
experimental data (e.g., Simons and Hager, 1997; Forte and Mitrovica, 2001; Karato and
Wu, 1993).

the strength of plate boundary σ_{st}). As a result, a lower viscosity μ_a is required to repro-

duce the same σ_{st}, as compared with the results of equation (3.4) (broken lines, Figure

3.7). Setting $\sigma_R (\leq \sigma_{st} \approx 0.78$–18 MPa), $\mu_a = 10^{19}$–10^{20} Pa s, and D_{RS} = 60–140 km, and

considering the uncertainty of plate size in plate model, we estimate $\sigma_{st} \approx 3$–75 MPa.

3.3   Discussion

3.3.1   Force balance in spin motion

Our analysis for the driving force of plate spin motion assumes the "rigid" plate and deformations are concentrated in the plate boundary. In fact, plate model PB2002 excludes the active deformation zones (orogens) and our analysis also deals with the other regions. However, the plates defined as rigid would also deform though the deformation is probably small. We here consider the effect of the deformation upon the dynamics of spin motion. With deformation, the driving force along plate boundary is used for the deformation of the plate as well as for the plate motion. As a result, the actual driving stress might be higher than the estimated driving force in this study, indicating a higher strength of plate boundary than our estimates.

In addition, for the force balance in the spin motion, we consider the force along plate boundary induced by the interaction with the motion of the neighboring plates and the resistive force resulted from the asthenosphere. Another conceivable force exciting plate spin motion is the "driving" drag force from the asthenospheric mantle flow. In order to exist such a mantle flow in asthenosphere, there must be the horizontal heterogeneity in the same scale to the plate size. However, any observation do not support the global heterogeneity just beneath the plate in the scale of one thousand or several hundred kilometers and mantle is mainly driven by the thermal convection, which generates poloidal motions instead of toroidal motions (Hager and O'Connell, 1978). In short, the forces we considered in the force balance of the spin motion seem sufficient to investigate the driving force for the spin motion.

Furthermore, in our analysis we estimated the magnitude of the conceivable forces within a certain range of several parameters which are poorly constrained, such as the vis-

cosity and the thickness of the asthenosphere. Another parameter which might vary is the thickness of plate boundary. We utilized the thickness of oceanic plate at the age of 60 Myr (Kohlstedt et al., 1995). Whereas the older oceanic plate than 60 Myr would not change the thickness substantially (Stein and Stein, 1992), there are several plates holding ridge along the plate boundary, which must contain the thinner plate along the ridge. Along such a plate boundary, the driving force is transmitted by the thinner plate boundary and the actual stress might be higher than our estimate. Nonetheless, the upward passive mantle flow to compensate the plate along the ridge might increase the temperature of the mantle beneath the plate, which may decrease the viscosity of the asthenosphere and the resistive force. Hence, while the existence of ridge will affect our analysis of the plate spin motion, the thin plate boundary and the soft asthenosphere might cancel the influence of the ridge upon the estimate of the strength of plate boundary and the difference in the estimate might be small.

3.3.2   Error of spin motion

Compiling the error of the plate motions of PB2002 in Table 1.1, here we consider the effect of the errors on our suggestion. We extract the error of the spin motion of a plate without a slab as we did in Figure 3.3. The result is Figure 3.8. Although there are plates, especially in Southeast Asia, in which the observation for the motion did not estimate the error (red cross in Figure 3.8), we instead estimate the minimum error by considering the total errors of the relative Euler poles to obtain the Euler pole of the plate. In other words, when we calculate the Euler pole of a plate, we start the most stable plate, the Pacific plate in PB2002, and move to one of the neighboring plates, in which we calculate the relative Euler pole between the neighbor and the Pacific plate, and we continue the movement to the neighboring plate and the calculation of the relative Euler pole until we arrive at the goal,
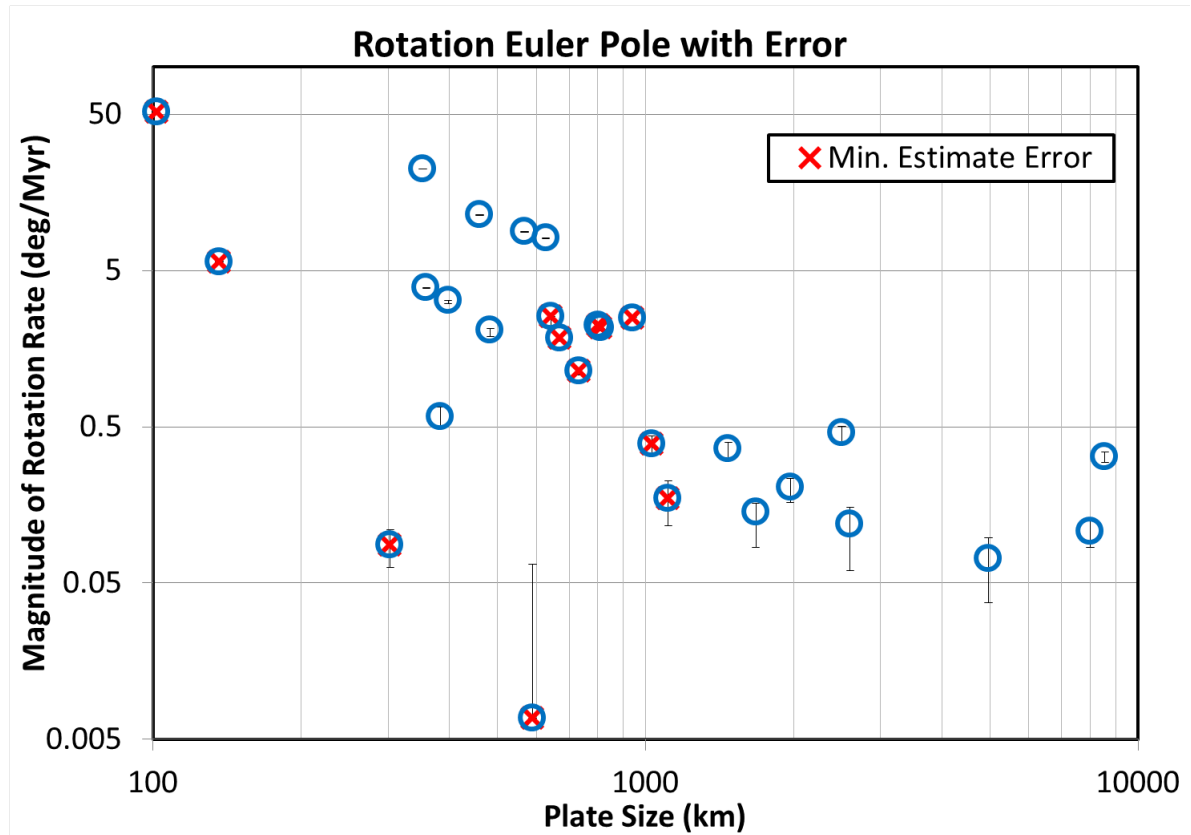
Fig. 3.8   Rotation rate of spin motion with error. Blue circles represent the spin motion of a plate without slab in PB2002 (Bird, 2003). The vertical bars shows the error from observation. The red cross represent the estimated minimum error. Regarding the detail, please read the text.

i.e., the plate that we would like to know the Euler pole. The minimum error represents the summation of the errors in those relative Euler poles. Figure 3.8 demonstrates that errors in spin motion do not deteriorate the main feature of the result, i.e., small plates spin actively and large plates hardly hold spin motions.

3.3.3   Effect of slab on geometrical center and Euler pole division

In this study, we calculate the geometrical center of the plate to obtain the spin Euler pole and the straight Euler pole from the observed Euler pole (Figure 3.1). Here, we consider the effect of the slab on geometrical center and the calculated Euler pole. We focus on a small subducting plate, the Cocos plate, because the smaller the plate, the larger the
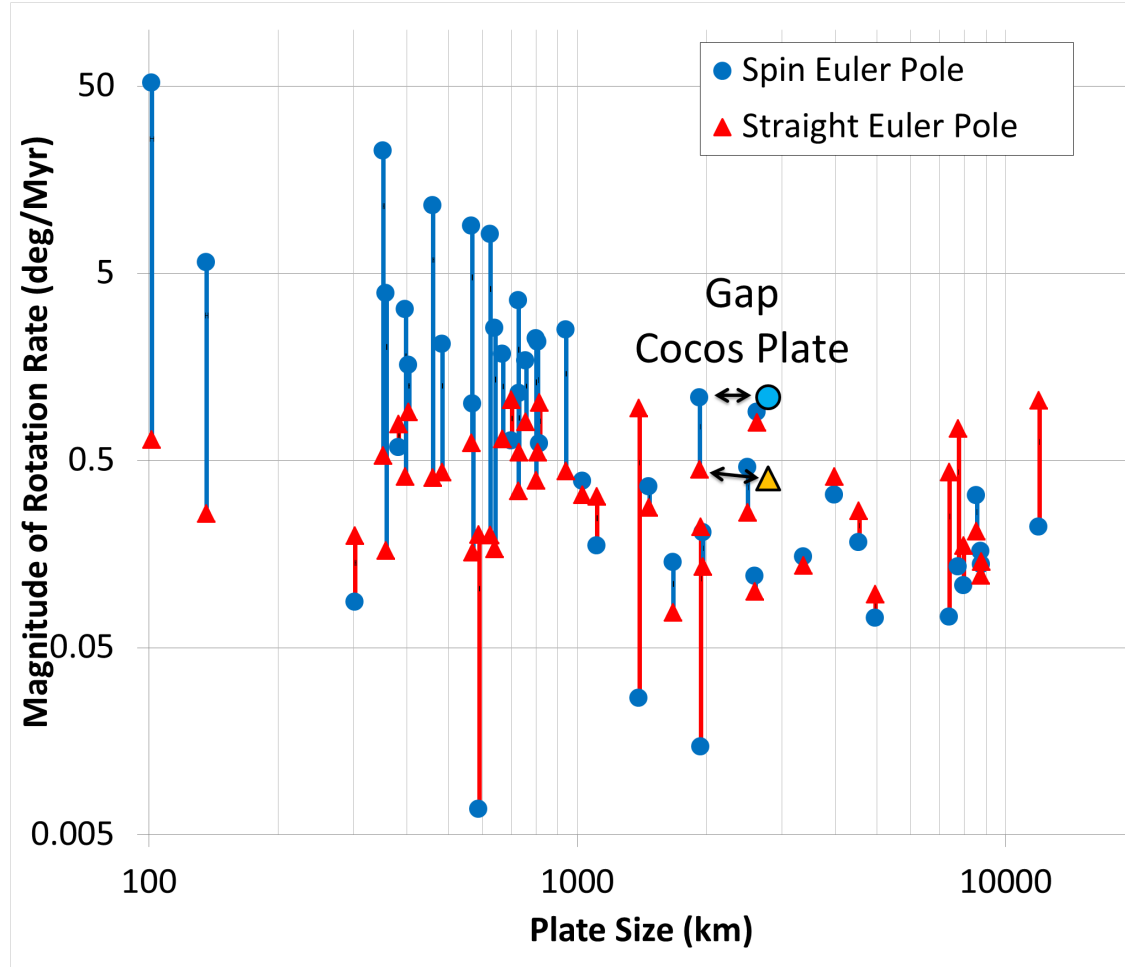
Fig. 3.9   The effect of slab on the plate spin (ω_C) and straight (ω_G) motions as a function of plate size. A light-blue circle and an orange triangle represent the spin and straight motion of the Cocos plate including the effect of the slab area. For the other explanation, please refer to Figure 3.1.

effect of the slab on the Euler pole division. With the tomography data of the Cocos plate (Gorbatov and Fukao, 2005), we estimate the area of the slab between the depth from 0 to 600 km in the upper mantle, and calculate the geometrical center and the divided two Euler poles. The obtained Euler poles are Figure 3.9. The result shows that the effect of the subducted slab on the geometrical center and the Euler pole division is almost ignorable.

3.3.4 Focal mechanism of earthquake and work of plate boundary

We found that the interaction between plates via plate boundary is essential for small-plate spin motion and especially a fast-moving plate drives the adjacent small plates through the drag along the plate boundary. In order to make sure the role of plate boundary of an active-spin plate, here we investigate the seismological data, particularly the focal mechanism, around the plate since those data contain the information about the stress distribution on the plate and the direction of the stress. The data of earthquakes were taken from CMT catalog between the date from 1976/1/1 to 2015/12/1 and at the depth shallower than 100 km to see the stress of the lithosphere (Dziewonski et al., 1981; Ekstrom et al., 2012).

First, we look at the seismicity around the Easter plate (EA) and the Juan Fernandez plate (JZ) because of the relatively simple circumstances where the Pacific plate (PA) and the Nazca plate (NZ) move westward and eastward, respectively, and excite the spin motion of the two micro plates (Schouten et al., 1993) (Figure 3.10). Along the northern and southern plate boundary of the two small plates, which are estimated as a driving plate boundary, there are strike-slip earthquakes and the direction of the imposed stress seems consistent with the plate spin motions. For instance, around the southern plate boundary of the Easter and Juan Fernandez plates there are right-lateral strike-slip faults, implying that the Pacific plate drag those two plates and induce the clockwise spin motions. Another notable characteristic about the focal mechanism is that the beach balls around the several other plate boundaries, such as the western plate boundary of the Easter plate, have the opposite stress direction to that along the driving plate boundary, i.e., left-lateral strike-slip faults, which indicates that those plate boundaries work as a resistive source.

Secondly, we investigate the focal mechanism around the Niuafo'ou plate (NI) off Fiji
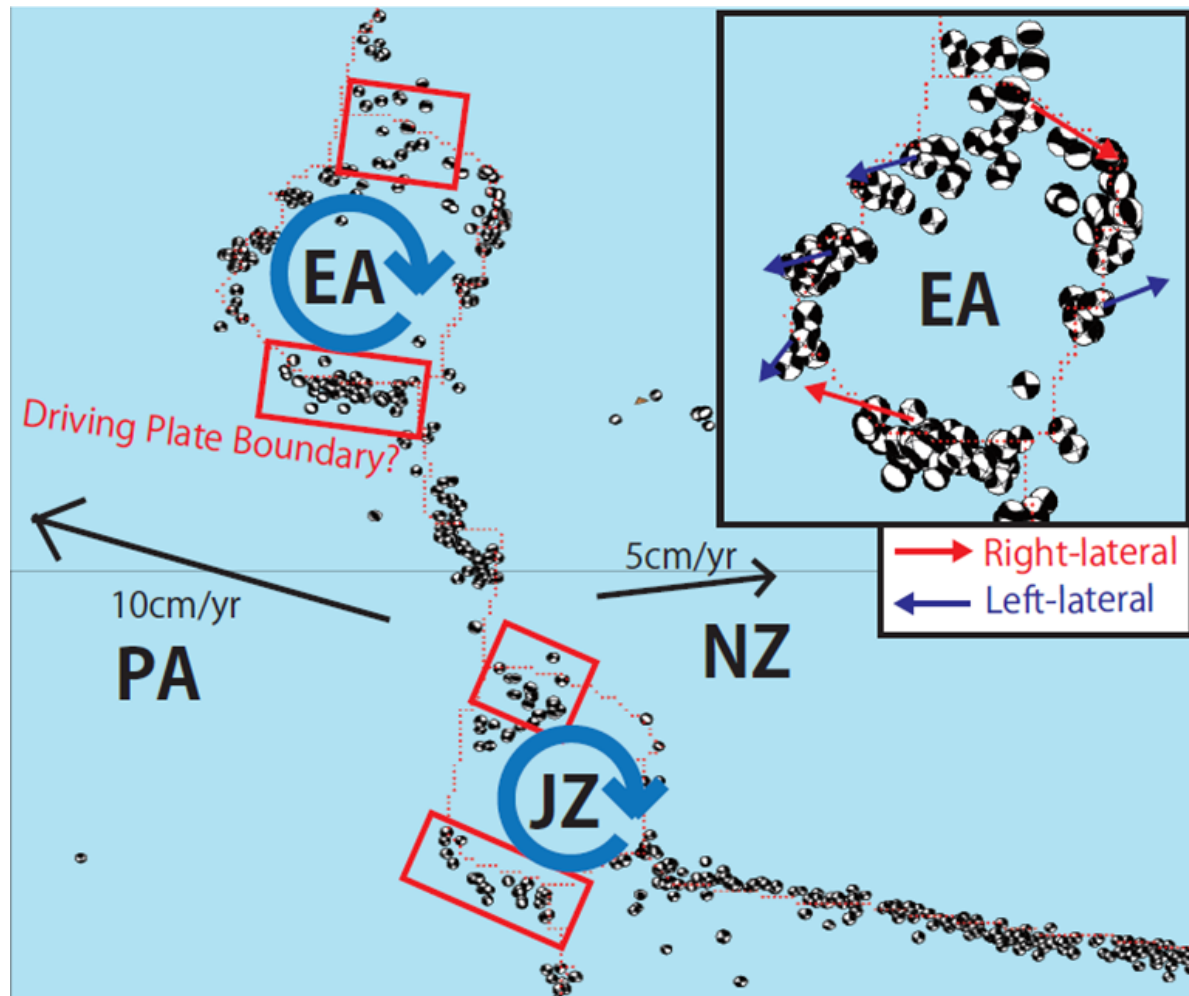
Fig. 3.10   Focal mechanism around the Easter and Juan Fernandez plate in the East Pacific Ocean. For the explanation, please read the text.

Islands in the South Pacific Ocean because the plate has a high spin motion and is also an oceanic plate like the Easter and Juan Fernandez plate. The result is Figure 3.11. The northern plate boundary of the Niuafo'ou plate, which seems the driving plate boundary based on the direction of the spin motion of the Niuafo'ou plate and the plate motion of the Pacific plate, shows consistent focal mechanisms, i.e., left-lateral strike-slip faults. In contrast, the southwestern plate boundary with the Australia plate (AU) exhibits the opposite fault, right-lateral strike-slip faults, suggesting that the plate boundary works as a resistive plate boundary. Another feature about the seismicity is that the earthquakes
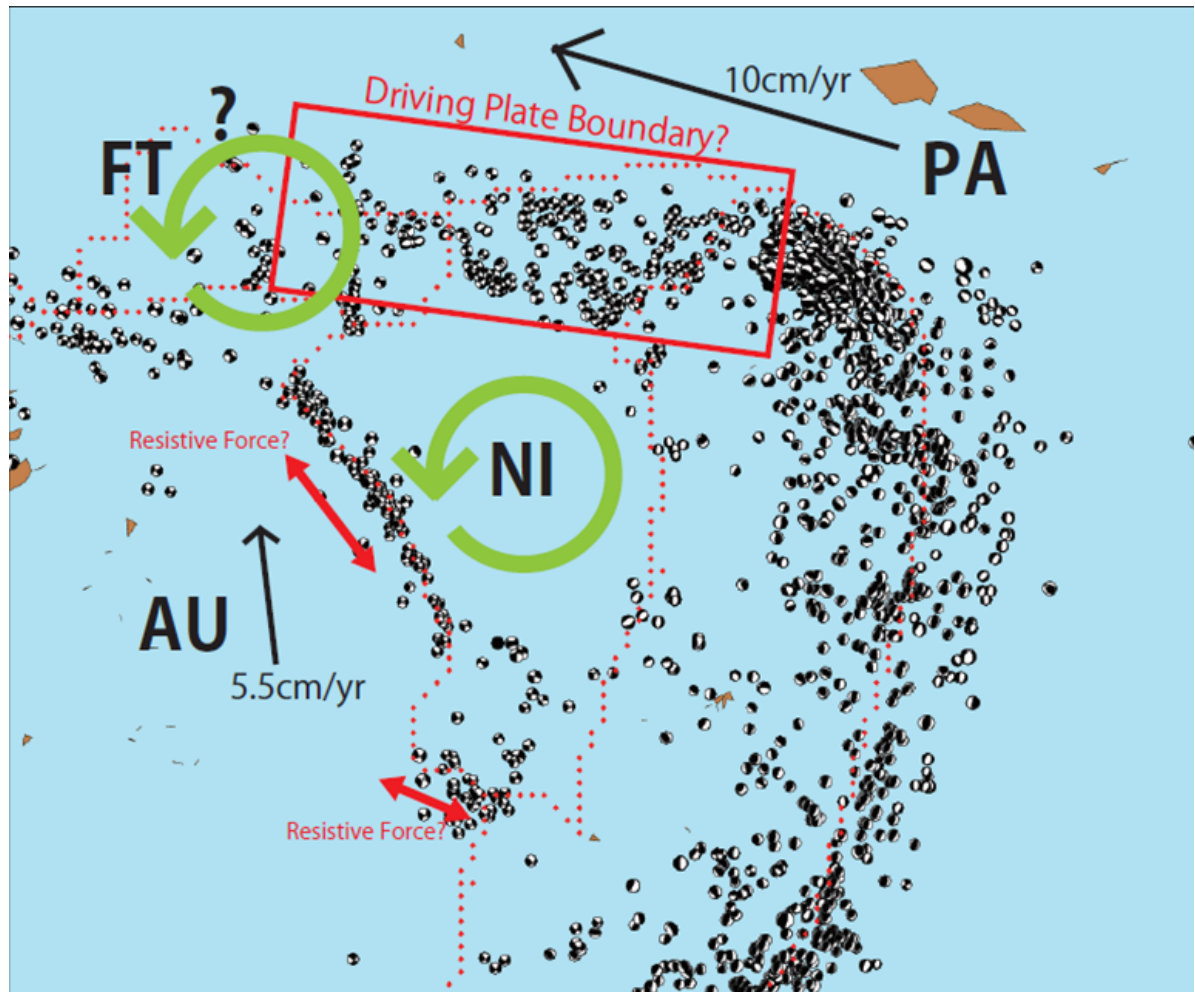
Fig. 3.11 Focal mechanism around the Niuafo'ou plate in the South Pacific Ocean. For the explanation, please read the text.

along the driving plate boundary are rather scattered and those along the resistive plate boundary are aligned with the line, which might indicate that the driving stress from the Pacific plate is supported by using the strength of the plate as well as the plate boundary. This observation implies that our estimates about the strength of the plate boundary, 3–75 MPa, partially represents the strength of the plate itself, which is estimated as 17–170 MPa (Tackley, 2000b) and 50–150 MPa (Richards et al., 2001) based on the numerical simulation of mantle convection.

Finally, we attempt to analyze a plate in Southeast Asia, which holds complicated small subduction zones and many small islands. Therefore, plates in this region may not be

suitable to be used as an oceanic plate like the examples above. The plate that we focus on is the South Bismarck plate (SB) (Figure 3.12). The northern plate boundary of the South Bismarck plate with the North Bismarck plate (NB) shows left-lateral strike-slip faults. However, from the direction of the spin motion, the plate boundary seems to work as a resistive plate boundary although the direction of the spin motion of the smallest plate in PB2002, the Manus plate (MN), is consistent with the focal mechanisms. As the driving plate boundary for the South Bismarck plate, a candidate is the southwestern plate boundary with the Woodlark plate (WL). Whereas there are some right-lateral strike-slip faults around the plate boundary, there is no clear driving plate boundary around the plate probably because the boundary exists on the islands and is different from the oceanic plate boundary that we mainly deal with in this study, particularly, in the point of the strength of the coupling because of the different structure (Kohlstedt et al., 1995). In addition, another plate model, GSRM v2.1 (Kreemer et al., 2014) defines Southeast Asia as an active deformation zones rather than rigid plates, suggesting that GSRM v2.1 defines plate configuration more accurately or at least more consistently to the seismological data than PB2002. But, please note that our suggestion about the driving force of the spin motion and the estimated strength of plate boundary is robust in both plate models (Figure 3.3 and 3.5).
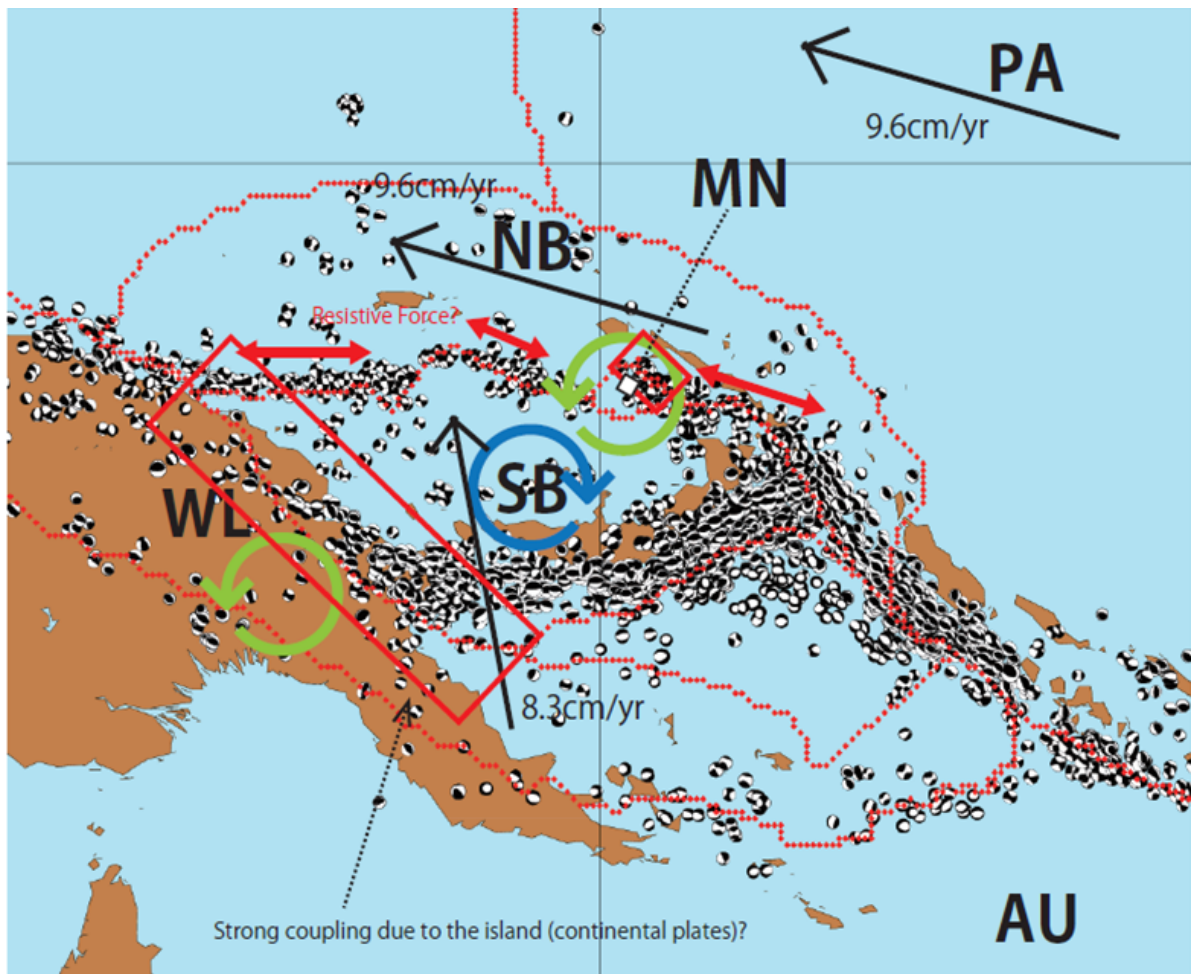
Fig. 3.12   Focal mechanism around the South Bismarck plate in Southeast Asia. For the explanation, please read the text.

3.3.5 Strength and rheology of plate and plate boundary

In previous studies, the strength of a plate boundary was estimated based on seismic observations, particularly the spatial mapping of earthquake focal mechanisms and their corresponding temporal changes before and after a large earthquake; e.g., Hasegawa et al. (2012) used high-resolution data on the approximately 4000 earthquake focal mechanisms in northeast Japan between 2003 and 2011, and found that the 2011 Tohoku earthquake almost completely released the accumulated stress along the plate boundary, and they estimated the stress at release to be as small as 5–15 MPa, suggesting that the presence of water weakened the plate boundary fault. Hardebeck and Hauksson (2001) used the focal mechanism data of approximately 50,000 earthquakes along the San Andreas Fault, mainly between 1981 and 1999, including the 1992 Landers earthquake, and estimated the strength of the fault to be about 10–30 MPa, due in part to the low mechanical strength of smectite (Carpenter et al., 2011). Compared with those previous studies, our obtained strength of plate boundary, 3–75 MPa, is consistent with a stress level deduced from high-resolution seismic observations of specific areas.

To naturally reproduce plate-like structures and motions as part of a mantle convection process, including the case of rigid plates with soft plate boundaries, three-dimensional numerical simulations have been used to investigate critical conditions and requirements, especially those concerning rock rheology. Tackley (2000b) and Richards et al. (2001) estimated the required yield stress of a plate to reproduce Earth-like plate motion on the basis of surface velocity fields, and obtained results of 17–170 MPa and 50–150 MPa, respectively. In addition, Bercovici (1993, 1995b, 2003) suggested that a pseudo-stick-slip rheology, in which the stress decreases with increasing strain rate after yielding, can reproduce plate-like motions, in particular a high toroidal/poloidal kinetic energy ratio of up to

0.8, which is consistent with ratios observed in previous studies (Hager and O'Connell, 1978; O'Connell et al., 1991; Bercovici and Wessel, 1994) as well as in this study (Fig.2.3). In this context, after exceeding the yield stress of plates, the strain can be concentrated to form a plate boundary composed of a "damaged" weak zone (e.g., Bercovici and Ricard, 2014), where the stress level is significantly reduced, possibly to the range estimated from seismology and this study, especially when water is present to weaken the plate boundary. However, as we showed in Section 3.3.4 and particularly in Figure 3.11, plate itself as well as plate boundary might sustain the stress to spin a plate by the interaction between the plates, which might indicate that we should deal with the driving force and plate motion in more general theory than conventional plate tectonics only with rigid plate and deforming narrow plate boundary.

Compared with those previous studies to estimate the strength of plate or plate boundary, seismology and numerical simulations, the uniqueness of our study is the following point; while the estimate of the strength of plate boundary from seismology contains a less errors than our estimate, they can only estimate the strength of limited plate boundary where large earthquakes were observed. In contrast, our analysis deals with observed global plate motions and, therefore, obtained value may be regarded as a globally averaged value for many plate boundaries based on observations instead of numerical simulations. In these point, our estimate about the strength of plate boundary has some significance compared with other estimates from different types of studies.

The exact rheology and the physical-chemical state of plate boundary is a vital problem that will help understand the mechanisms of plate tectonics (e.g., Gordon, 1998, 2000; Bercovici and Ricard, 2014). At present, it is difficult to constrain the exact rheology from the approach in this study; however, by combining with other approaches, such as seismic and geodetic observations on both rigid plates and deformation zones (Gordon, 1998,

2000; Kreemer et al., 2014), field and laboratory studies on rock and fault rheology (e.g., Kohlstedt et al., 1995; Sibson, 2003), and numerical simulation of combined plate motion and mantle convection (e.g., Tackley, 2000b; Richards et al., 2001; Bercovici, 2003), tighter constraints can be obtained to quantify the Earth's dynamics with regard to plate tectonics.

3.4 Summary

The main objective of this chapter was to constrain the driving forces of plate motion, especially the plate spin motion, for which we analyzed the spin motion of each individual plate as a function of plate size with detailed plate models. The following results were obtained. First, spin motion of plates without slabs decreases at plate sizes of ∼ 1000 km and greater (Figure 3.3), which indicates the strength for plate boundaries (Figure 3.5). Secondly, the geographical distribution of spin motion (Figure 3.6) suggests that large plates with subducting slabs drive the spin motion of surrounding smaller plates, similar to gears that transmit the shear stress induced by straight motion of large plates. Thirdly, seismicity and the focal mechanism indicates that the driving force to spin a small plate might be transmitted through not only the plate boundary but also plate itself (Figure 3.11). Finally, from the force balance of spin motion at the critical plate size, we obtain the relationship between the strength of the plate boundary and the viscosity of the asthenosphere (Figure 3.7). Assuming the viscosity and thickness of the asthenosphere to be 10^{19}–10^{20} Pa s and 60–140 km, respectively, we roughly estimated the strength of the plate boundary to be 3–75 MPa, which is comparable to the stress level estimated from several seismological observations, including those in NE Japan associated with the 2011 Tohoku earthquake.

Chapter 4

Spin motion and buckling of the Philippine Sea plate

4.1 Introduction

The Philippine Sea plate (hereafter referred to as PHS) is one of the two exceptional plates (i.e., PHS and the Cocos plate) in terms of the size-rotation rate relation as was discussed in Chapter 2 and 3. In this Chapter 4, we focus on PHS to investigate possible mechanism of its spin motion, since a number of observations have been made both on the motion and the stress applied to PHS more than the Cocos plate as will be stated below. We first describe a key feature near the northern edge of PHS, i.e., the slab geometry and stress for the subducted PHS slab beneath the southwestern Japan arc, and show evidences for east-west compression of the PHS slab, possibly an eastward applied stress. Based on the analysis, we then discuss the torque balance and spin motion of PHS.

Of the Japanese island arcs, the southwestern Japan arc exhibits a variety of unique characteristics associated with subduction of PHS; the Shikoku Basin is subducting along the Nankai Trough with an extinct ridge, the Kinan Seamount Chain (Okino et al., 1994, 1999) (Figure 4.1). Beneath the southwestern Japan arc, the subducted slab is aseismic due to its young and warm nature (Shiono, 1982), and deep-seated brines and gases with high

helium isotope ratios comparable to mantle values (Sano et al., 2009; Umeda et al., 2012; Kusuda et al., 2014), all of which are associated with the young warm slab of PHS. Another noticeable feature of the PHS slab is the wavy shape (e.g., Baba et al., 2002; Shiomi et al., 2004; Nakajima and Hasegawa, 2007; Hirose et al., 2008; Shiomi et al., 2008; Ueno et al., 2008; Iidaka et al., 2009) (Figure 4.2). As a previous work, Ide et al. (2010) investigated the slab shape assuming that the slab had deformed instantaneously in an elastic or brittle manner along an extinct ridge (i.e., the subducted Kinan Seamount Chain) due to a sudden change of the plate motion at 2 to 4 Ma, based on geological observations (Kimura et al., 2005; Ikeda et al., 2009).

In order to investigate a possible cause of enigmatic geometry of the PHS slab, we first quantify the slab geometry. Then, considering a buckling process as a possible mechanism of the wavy geometry of the PHS slab, we apply the theory of folding (e.g., Biot, 1957; 1961; Ramberg, 1959; Fletcher, 1974) to the slab geometry, based on which rheology, stress and buckling process of the PHS slab are discussed.
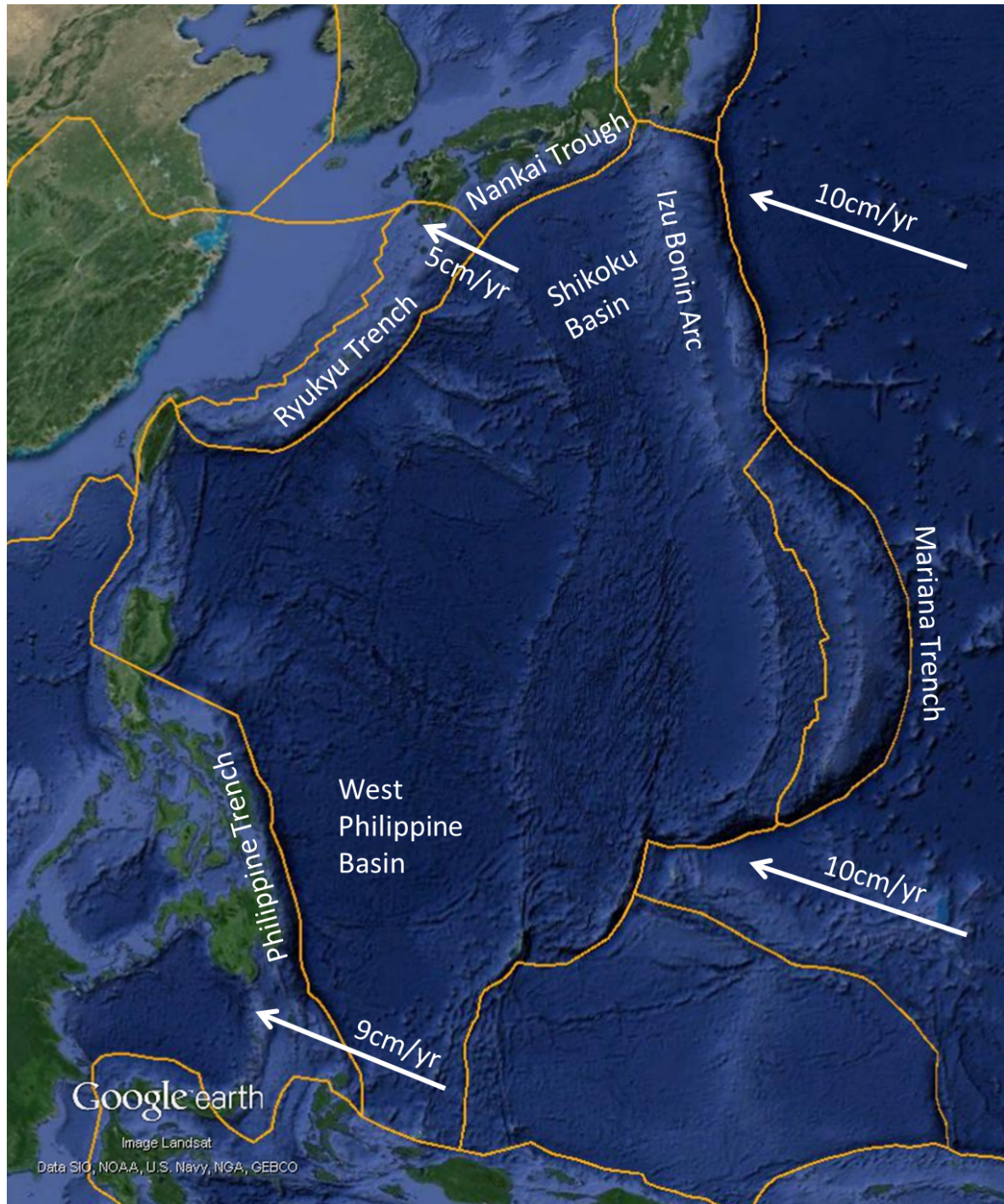
Fig. 4.1   Map of the Philippine Sea and the adjacent area. Orange lines and white arrows represent the plate boundary and the speed of the PHS and the Pacific plate (in reference frame of the Africa plate fixed) in PB2002 (Bird, 2003), respectively.
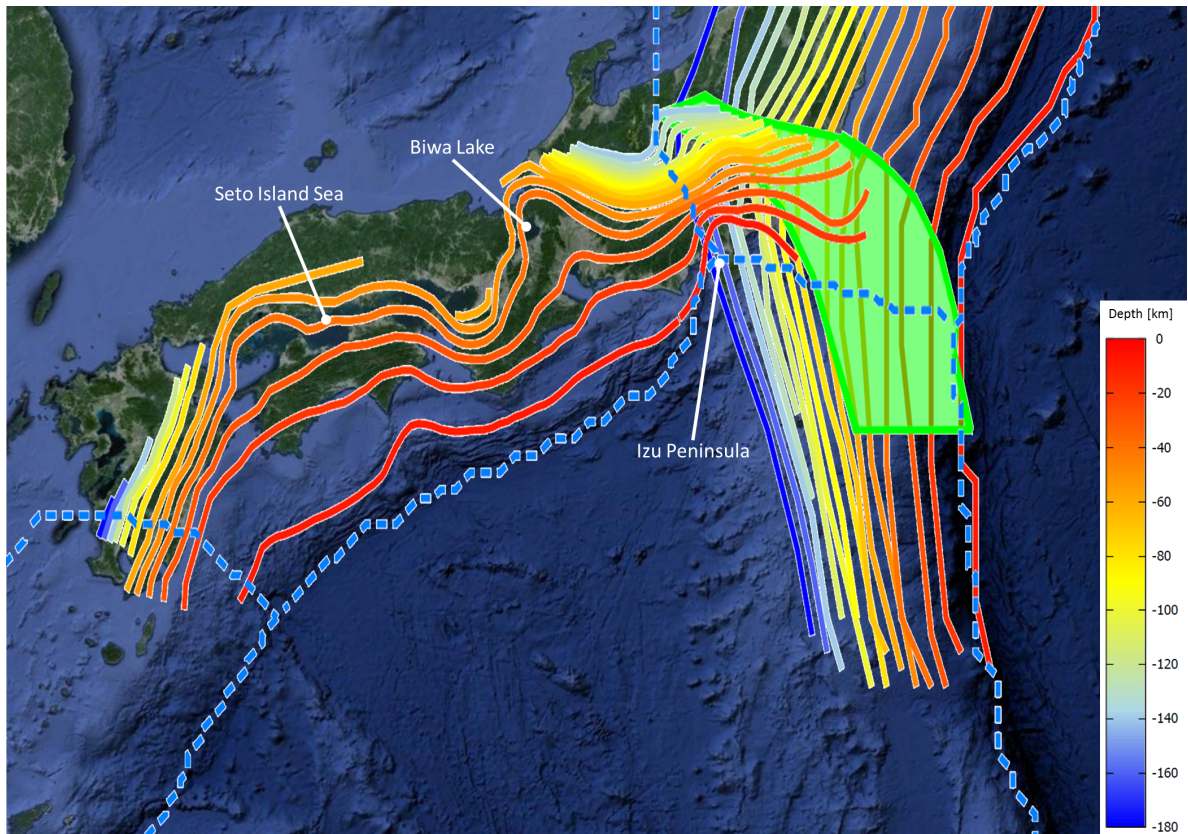
Fig. 4.2   Depth contour map of the PHS slab (Baba et al., 2002; Nakajima and Hasegawa, 2007; Hirose et al., 2008) and the Pacific slab (Nakajima and Hasegawa, 2006; Nakajima et al., 2009; Kita et al., 2010). Blue dashed lines represent the plate boundaries in PB2002 (Bird, 2003). Regarding the depth of the isodepth contour, please see the color bar in the figure. The green zone shows the contact area between the PHS slab and the upper surface of the Pacific slab beneath the Kanto district (Nakajima et al., 2009).

4.2 Analysis of slab geometry

We utilize the slab geometry acquired by seismicity data and seismic tomography (Baba et al., 2002; Nakajima and Hasegawa, 2007; Hirose et al., 2008) (Figure 4.2). The slab-surface geometry, in particular the wavy shape beneath the Shikoku district, is also supported by more recent study using the receiver function technique with spatially high-density seismic stations (Iidaka et al., 2009). The shape of the slab in Figure 4.2 has several notable features. First, the PHS slab is almost in contact with the upper surface of the Pacific slab beneath Kanto district (Nakajima et al., 2009) (represented by a green area in Figure 4.2). Secondly, the wavy shape has three peaks beneath the northern Izu Peninsula, the Biwa Lake and the western Seto Inland Sea (Figure 4.2). The easternmost peak beneath the northern Izu Peninsula is located at the triple junction among the PHS, the Eurasia (Amur) plate and the North America (Okhotsk) plate (Bird, 2003), where the Izu Bonin arc on PHS has thrusted beneath the Honshu arc since $\sim$ 17 Ma (Aoike, 1999) and now Izu Peninsula is colliding (e.g., Soh et al., 1998). The collision of the Izu Bonin arc distorted the slab shape beneath the Kanto district to Central Japan (e.g., Nakajima et al., 2009). In comparison with the easternmost peak, the other two peaks of the slab shape beneath the Biwa Lake and the Seto Inland Sea do not have such surface expression of collision or specific deformation features, suggesting that some slab-mantle interaction, e.g., mantle flow to cause east-west compression, could have been associated. In addition, compared with the small easternmost peak, the two western peaks are similar in size, repeating the folding-like shape, which has an affinity with buckling systems. For these reasons, we are going to develop analyses and modeling for the geometry including the two western peaks of subducted PHS slab, based on the theory of folding of strata/rocks and buckling.

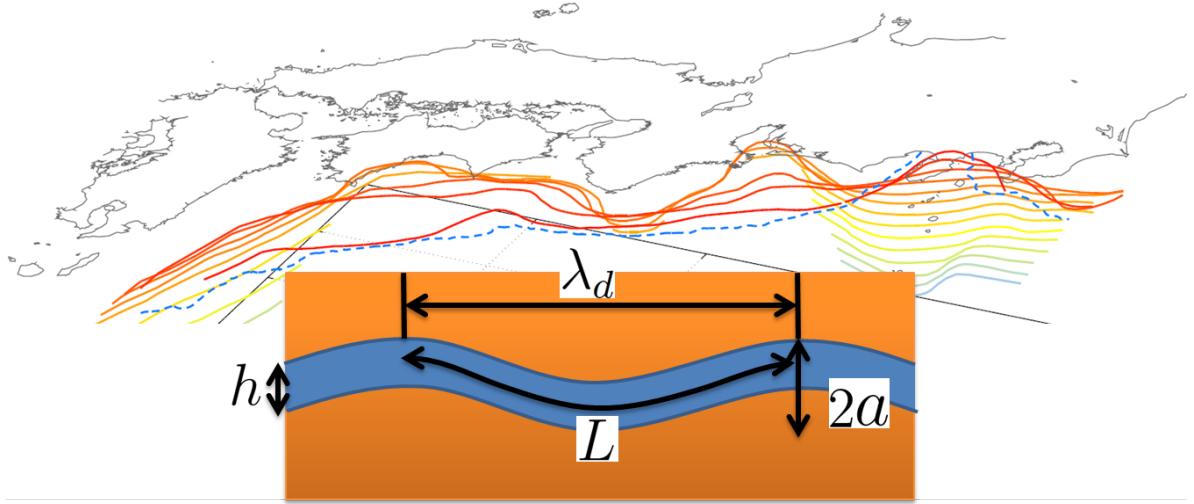In Figure 4.2 and 4.3, the geometry of the slab is shown vertically and obliquely to mea-

Fig. 4.3   Oblique view of depth contours of the PHS slab (Baba et al., 2002; Nakajima and Hasegawa, 2007; Hirose et al., 2008). Regarding blue dashed lines and the depth contours, please refer to Figure 4.2. From this geometry, we roughly estimate the dominant wavelength λ_d, arclength L and amplitude a.

sure the characteristic lengths (i.e., width and height) of the wavy geometry. From Figure 4.3, assuming the slab shape as sinusoidal, we estimate the dominant wavelength λ_d 400 km, arclength L 415 km and amplitude a 25 km. As regards the plate thickness, Yoshioka and Ito (2001) scrutinized the thickness of the PHS and its horizontal variation along the Nankai Trough taking into account the thick marine sediment, suggesting that the thickness h is approximately 25 to 35 km. With those parameters, we next apply the folding theory to this slab geometry.

4.3   Application of folding theory

Buckling is a dynamic instability as a result of series of folding, in which a layer in a media receives a layer-parallel compression (Biot, 1961; Hudleston and Treagus, 2010). The folding of the layer occurs due to the different physical properties between the layer and the media and the buckling can be observed in various conditions and scales (Figure 4.4). Since the first theory of folding and its applications to geology by Biot (1961), the theory has been improved to consider various rheologies of the layer and the surrounding media,
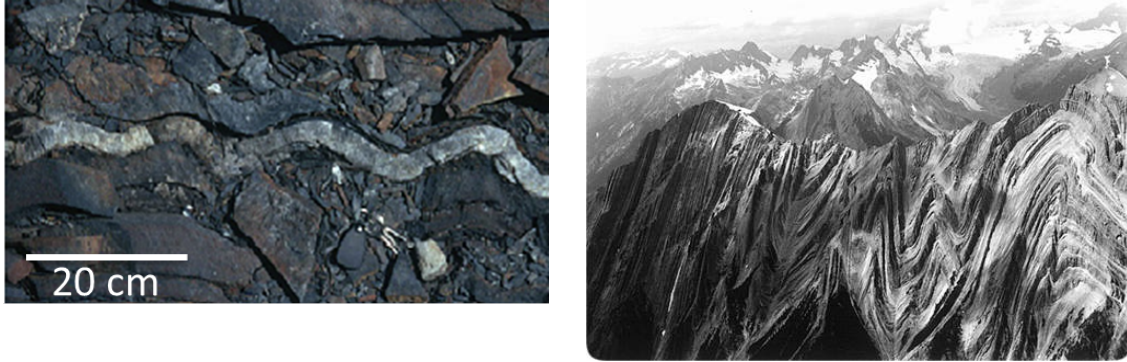
Fig. 4.4   Buckling/Folding in nature in various scales. Left figure: quartz vein in slate.
Right figure: mountains in British Columbia.

such as a Newtonian viscosity (Biot, 1961) and non-Newtonian rheology (e.g., Fletcher,
1974; Smith, 1975, 1977). In this study, we apply various theories, i.e., (i) elastic slab, (ii)
Newtonian slab, (iii) power-law slab and (iv) viscoelastic slab, to the PHS slab. Please note
that we assume Newtonian mantle, i.e., diffusion creep rheology in the surrounding man-
tle, rather than other complex rheologies, such as dislocation creep, which is adopted in a
high strain-rate region (Karato, 2010) (e.g., asthenospheric mantle beneath a fast-moving
plate). First, similarly to the analysis of Ide et al. (2010), we analyze the slab of PHS as an
elastic layer in a Newtonian viscous mantle.

4.3.1   Elastic slab

Here in this section, we consider an elastic slab, such as the outer rise of oceanic plates
(e.g., Caldwell and Turcotte, 1979). Buckling of an elastic layer in a Newtonian viscous
media is expressed by the following equation (Biot, 1961; Turcotte and Schubert, 2002)

$$\frac{\lambda_d}{h} = \pi \left(\frac{E_l}{\sigma \left(1 - v_l^2 \right)} \right)^{\frac{1}{2}}, \tag{4.1}$$

where λ_d, h, E_l, v_l and σ are the dominant wavelength, the thickness, the elastic moduli,
Poisson's ratio of the layer and the layer-parallel stress, respectively (Figure 4.5 (a)). Please
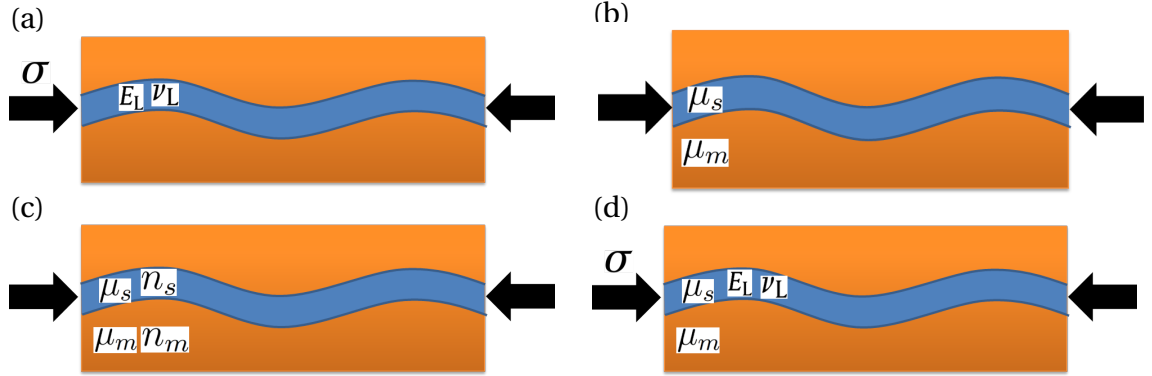note that in this case the equation is independent of the surrounding viscous media since

Fig. 4.5   Buckling with physical properties in various rheologies: (a) elastic, (b) Newtonian, (c) power-law rheology and (d) viscoelastic layer. As for physical properties, please refer to the text.

the elastic layer sustains the layer-parallel compression and controls the system. When we set E_l 65 GPa and ν_l 0.25 as representative properties of plate (e.g., Yoshioka and Ito, 2001; Turcotte and Schubert, 2002), substituting the slab geometry into λ_d and h yields $\sigma = 2.6$–5.2 GPa. However, when we estimate the negative buoyancy of the slab along the Nankai Trough, i.e., slab pull force, the net force is approximately 8×10^{17} N. In this estimate, we assume an average temperature gap between the PHS slab and the surrounding mantle: $\Delta T = 650$ K, slab thickness: $h = 25$ km, slab length: $L = 100$ km, mantle density: $\rho_m = 3300 \text{kg/m}^{-3}$, thermal expansivity: $\alpha = 2 \times 10^{-5}$ /K, and the length of the Nankai Trough from the Izu Peninsula to Kyushu district: $L_{trench} = 750$ km. Even when all the slab pull force is used only for the elastic buckling, the stress $\sigma \approx 0.3$ GPa, which is one order of magnitude less than the above estimate for elastic buckling. Therefore, hereafter we do not deal with the slab as an elastic layer in this analysis.

4.3.2   Newtonian slab

We next analyze the slab as a viscous layer, which is expected from relatively hot temperature of the young PHS (Okino et al., 1994, 1999; Yoshioka and Ito, 2001). When we assume a Newtonian viscous slab in a Newtonian viscous mantle, the viscosity contrast and the
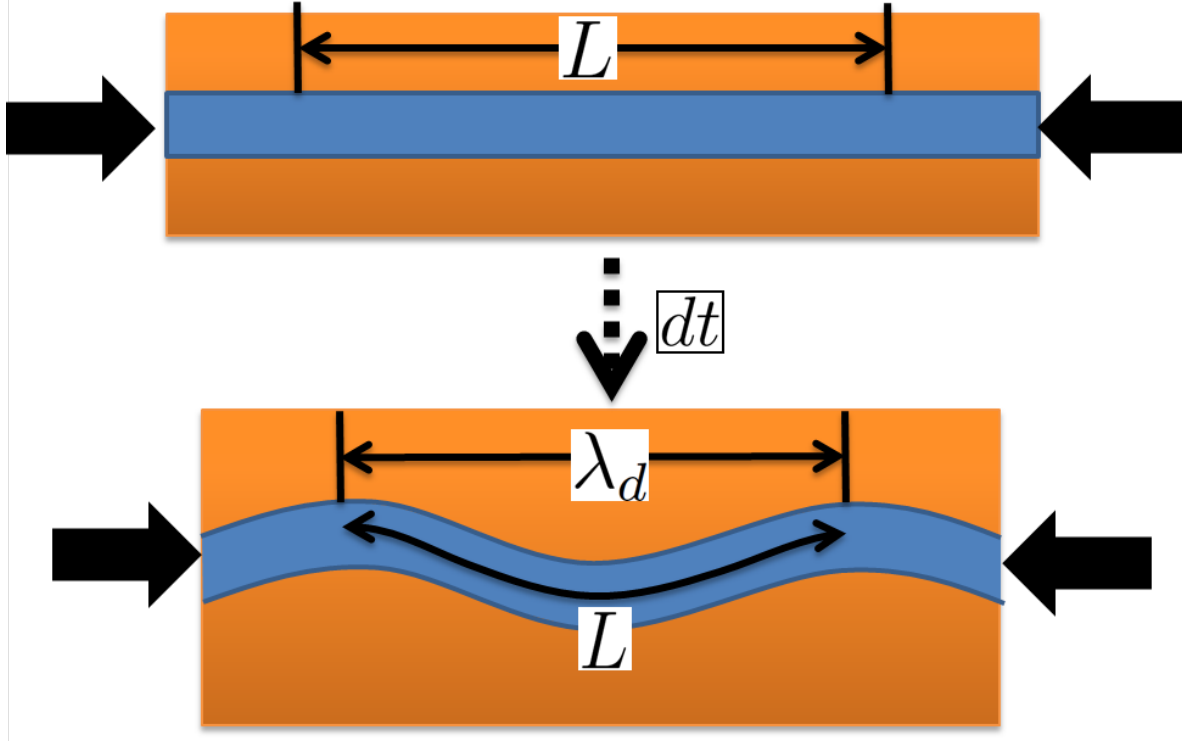
Fig. 4.6   The effect of mechanical shortening upon the dominant wavelength. At the initiation of compression, $\lambda_d = L$, however, as the strain accumulates, the dominant wavelength becomes short $\lambda_d < L$ and in folding theory we should utilize the initial dominant wavelength L.

slab geometry have the following relationship (Biot, 1961),

$$\frac{\lambda_d}{h} = 2\pi \left(\frac{\mu_s}{6\mu_m} \right)^{\frac{1}{3}}, \tag{4.2}$$

where μ_s and μ_m are the viscosity of the slab and the mantle, respectively (Figure 4.5 (b)). Substituting the slab geometry, we obtain the viscosity contrast between the PHS slab and the surrounding mantle approximately 36–100. More precisely, taking into account the effect of layer-parallel shortening by compression upon the dominant wavelength (Biot, 1965) (Figure 4.6), we substitute arclength L into wavelength λ_d in equation (4.2) as the initial wavelength and obtain the viscosity contrast 40–110.

4.3.3   Power-law (dislocation creep) slab

Next, we deal with the slab as an Non-Newtonian layer, in this case, a layer of power-law rheology. When we adopt power-law rheology, the relationship between the geometry of slab and the viscosity contrast becomes (Fletcher, 1974)

$$\frac{\lambda_d}{h} = 2\pi \left(\frac{\mu_s}{6\mu_m} \frac{n_m^{\frac{1}{2}}}{n_s} \right)^{\frac{1}{3}},$$

(4.3)

where n_s and n_m are the power-law exponents for the slab and the mantle, respectively (Figure 4.5 (c)). Setting $n_s = 3.5$ as dislocation creep rheology and $n_m = 1$ as diffusion creep rheology (Karato et al., 2001) yields $\mu_s/\mu_m = 130$–350. Including the mechanical shortening by compression as we did for a Newtonian slab, we obtain $\mu_s/\mu_m = 140$–390.

4.3.4   Viscoelastic slab

Next we consider the combination of two rheologies we analyzed above, i.e., viscoelastic rheology. In the case of a viscoelastic layer in a Newtonian viscous media (Figure 4.5 (d)), buckling is controlled mainly by one of the two rheologies, which is determined by the competition of the physical properties as follows (Schmalholz and Podladchikov, 1999): if

$$2 \left(\frac{\mu_s}{6\mu_m} \right)^{\frac{1}{3}} < \left(\frac{E_l}{\sigma \left(1 - \nu_l^2\right)} \right)^{\frac{1}{2}},$$

(4.4)

then the viscous rheology dominates buckling and we can adopt only viscous rheology and vice versa. In other words, the smaller dominant wavelength generated by viscous rheology or elasticity determines the buckling geometry. Setting E_l 65 GPa and ν_l 0.25 as representative properties and putting $\mu_s/\mu_m \equiv \Delta\mu$, we find the condition for the elasticity-dominant buckling as

$$\sigma \Delta\mu^{\frac{2}{3}} > 5.7 \times 10^{10}.$$

(4.5)

From our estimates of the viscous layers, substituting the viscosity contrast between the slab and the mantle $\Delta\mu \approx 40$–110 in Newtonian slab into equation (4.5) yields $\sigma > 2.5$–5

GPa, which is about one order higher than the stress induced by the slab pull force $\sigma \approx 0.3$ GPa as was discussed. This means that, even if the PHS slab has viscoelastic rheology, the slab is likely to behave viscously during buckling. Based on the buckling analyses with various rheologies, we suggest that the PHS slab has undergone viscous deformation rather than elastic one. Next, we constrain the viscosity of the slab based on the obtained viscosity contrast.

4.4   Viscosity of slab

Regarding the viscosity contrast between slab (or lithosphere) and the surrounding mantle $\mu_s/\mu_m(\mu_l/\mu_m)$, numerical simulations and model experiments have estimated $\mu_l/\mu_m = 500$–2000 (Di Giuseppe et al., 2008), $\mu_l/\mu_m = 150$–5000 (Newtonian plate) (Funiciello et al., 2008), $\mu_s/\mu_m = 100$–300 (Schellart, 2008), $\mu_s/\mu_m = 100$–700 (Schellart, 2009). From observed slab stress conditions and fluid modelling, Alpert et al., (2010) put forward the general viscosity contrast between slabs and upper mantle as $\mu_s/\mu_m = 10$–100. In our study, analyzing the horizontal wavy shape of the PHS slab, we constrain the viscosity contrast between the slab and the mantle as $\mu_s/\mu_m \approx 40$–110 for Newtonian rheology and $\mu_s/\mu_m \approx 140$–390 for power-law rheology. It is noted that old and cold plates, such as the Pacific plate beneath the Tohoku district, might be more viscous than our estimates whereas the effect of water in cold slab and slow grain-growth due to the low temperature may compensate the increase in viscosity (Karato and Wu, 1993; Karato et al., 2001).

With regard to the estimate of the slab viscosity from the viscosity contrast, we assume that the mantle wedge (the mantle above the slab) is softer than the suboceanic mantle (the mantle beneath the slab) due to the fluid derived from the slab and melting of the mantle in mantle wedge (e.g., Iwamori, 1998; Iwamori and Zhao, 2000; Iwamori et al., 2007; Hall, 2012) and also assume that the harder suboceanic mantle controls the system.

Then, adopting the representative viscosity 2.6×10^{21} Pa s (Simons and Hager, 1997), we estimates the slab viscosity as

$$\mu_s = 1 \sim 3 \times 10^{23} \; [\text{Pa s}] \qquad (\text{Newtonian}) \tag{4.6}$$

$$\mu_s = 3 \sim 14 \times 10^{23} \; [\text{Pa s}] \qquad (\text{power} - \text{law}). \tag{4.7}$$

We now investigate the time required to generate the observed strain (i.e., amplitude of folding) . Buckling of a Newtonian layer and power-law layer are expressed as (Biot, 1961; Fletcher, 1974; Turcotte and Schubert, 2002)

$$\sigma = 4\mu_s \left(\frac{\varepsilon}{\Delta t} \right) \qquad (\text{Newtonian}) \tag{4.8}$$

$$\sigma = 4\frac{\mu_s}{n_s} \left(\frac{\varepsilon}{\Delta t} \right) \qquad (\text{power} - \text{law}) \tag{4.9}$$

σ, ε and Δt are the layer-parallel compressive stress, strain and the time taken for the deformation, respectively. As for the strain ε, regarding amplitude/wavelength $= a/\lambda_d << 1$ gives the strain $\varepsilon \approx (L - \lambda_d)/L \approx 0.036$. In the unconstrained parameters, σ and Δt, we estimate the compressive stress σ from the spin motion of PHS because the active clockwise spin motion (Section 3 and Figure 4.7) results in the collision between the slab of the PHS and the Pacific plate (Figure 4.2) (Nakajima et al., 2009) and the driving force for the spin motion can be regarded as the compressive stress for the buckling. For this reason, next we estimate the driving force of the spin motion of the PHS in a simple torque analysis.

4.5   Force balance for the motion of the Philippine Sea plate

4.5.1   Euler pole analysis of the Philippine Sea plate

In plate tectonics, slab pull force is the most essential driving force (e.g., Forsyth and Uyeda, 1975; Conrad and Lithgow-Bertelloni, 2002) and PHS accompanies the Nankai Trough, the Ryukyu Trench and the Philippine Trench, all of which induce a straight motion toward the trench but cannot generate a significant spin motion (Figure 1.3). Seno
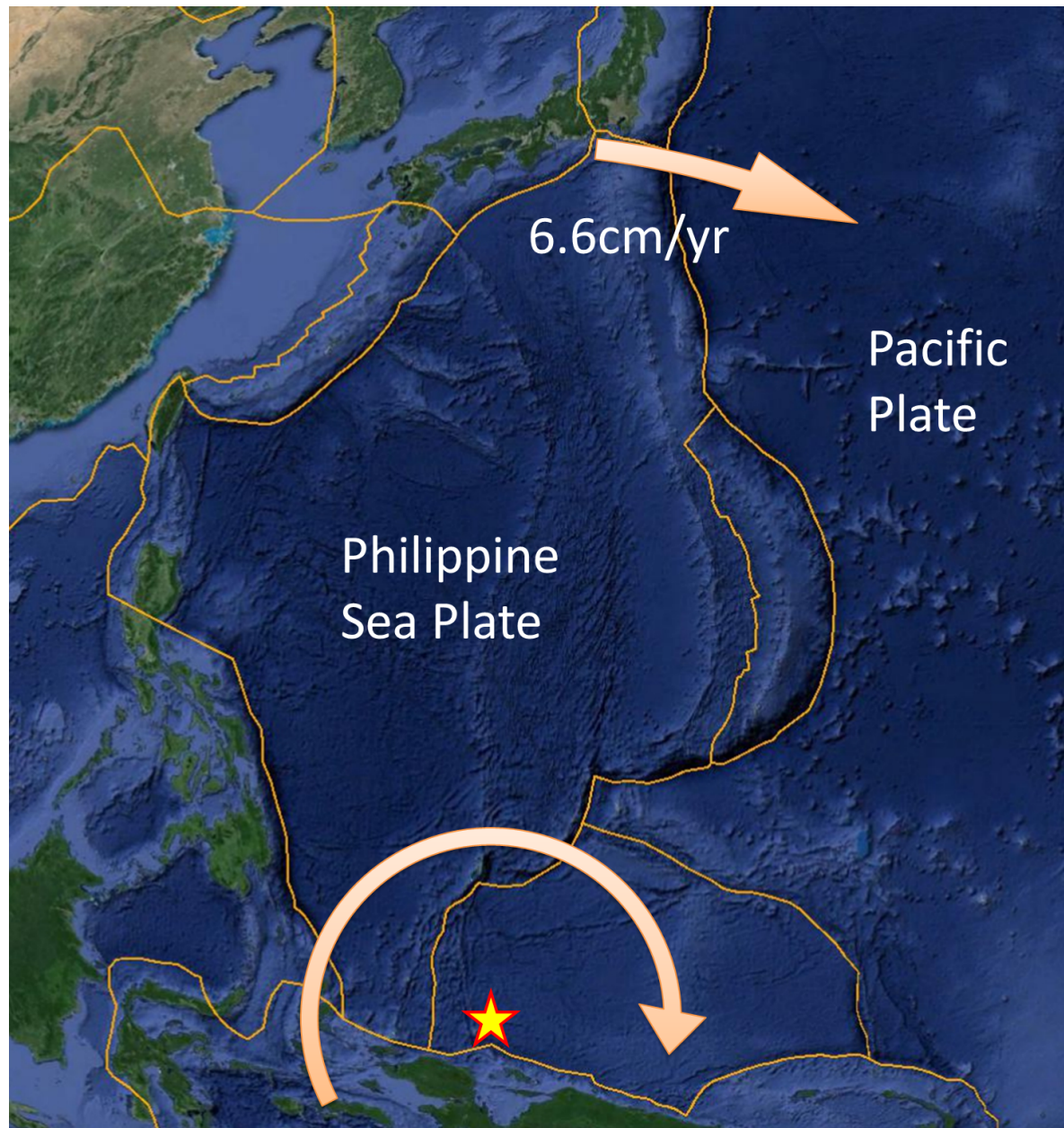
Fig. 4.7   Relative motion between the PHS and the Pacific plate in PB2002 (Bird, 2003). The yellow star represent the relative Euler pole between the PHS and the Pacific plate and, in the Pacific plate fixed reference frame, therefore, the PHS moves along the orange vector, indicating a strong collision between the two plates at the northern part of the PHS.

(1999) investigated the crustal stress variation in Japan and suggested that the Kyushu district has a clear variation in the horizontal stress. He argued that beneath the Kyushu region there is a eastward mantle flow derived from a mantle upwelling off the west coast of Kyushu, which is supported by the electrical conductivity (Shimoizumi et al., 1997; Handa, 2005) and seismic observations (Sadeghi et al., 2000; Yoshizawa et al., 2010). We utilized the above two driving forces, the slab pull and the trench-parallel force beneath the southwestern Japan arc, to simulate the observed Euler pole of the PHS in a simple torque model and compare them to estimate the driving force for the spin motion.

Utilizing the plate model PB2002 (Bird, 2003), we impose uniform forces normal to the subduction zone of PHS as an "effective" slab pull force (light blue vectors in Figure 4.8). The effective slab pull is the net force of the slab pull force and the slab resistance and the magnitude of the force is approximately one order lower than the original slab pull force (Forsyth and Uyeda, 1975). Then, we put another force along the Nankai Trough as the stress suggested by Seno (1999, 2000) (pink vectors in Figure 4.8) and chose the direction and magnitude of the force so as to generate the observed Euler pole. Here we assume that those considered forces are dominant and determine the direction of the plate motion, which is justified by the previous studies of torque analysis (e.g., Forsyth and Uyeda, 1975). The ideal vector is acquired in the almost eastward direction at the magnitude of 2.7 larger than the effective slab pull force. In this calculation, we put the density of mantle $\rho = 3300 kg/m^3$, the difference in temperature between mantle and slab $\Delta T \sim 500$ K, thermal expansivity $\alpha = 2 \times 10^{-5}$, gravitational acceleration $g = 9.8 kg/m^3$, the representative vertical length L_r and thickness h_r of the PHS slab $L_r \sim 250$ km and $h_r \sim 35$ km (Yoshioka and Ito, 2001; Becker and O'Connell, 2001; Turcotte and Schubert, 2002). Assuming that the obtained stresses along the Nankai Trough is applied to the compression of the slab buckling beneath southwestern Japan (Seno, 1999, 2000), the imposed stress on the

slab becomes 4 to 40 MPa, which is in the range of our estimate for the strength of plate boundary in Chapter 3, 3 to 75 MPa. Although the meaning of this consistent result is not so clear, yet it might imply that the PHS also has a high spin motion because the driving stress can be sustained by the strength of the plate boundary or slab. From equation (4.8) and (4.9), the time of buckling is

$$\Delta t = 4.6 \sim 13 \; [\text{Myr}] \qquad (\text{Newtonian}) \tag{4.10}$$
$$\Delta t = 4.0 \sim 19 \; [\text{Myr}] \qquad (\text{power} - \text{law}). \tag{4.11}$$

With this result, next we discuss the history of the PHS motion and the dynamics.

4.5.2   History of the Philippine Sea plate

The history of PHS motion has been investigated in many previous works to understand the geological and tectonic events around the Japan arcs for the last several tens of million years, such as opening of the Japan Sea and the collision of the Izu arc, although there are large uncertainties (e.g., Seno and Maruyama, 1984; Hall et al., 1995; Hall, 2002; Kimura et al., 2005; Gaina and Muller, 2007; Yamazaki et al., 2010). We here raise one unique event in the history and propose a possibility of the buckling to understand the cause of the unique wavy shape of the PHS slab and discuss the tectonic evolution with our buckling analysis.

It is suggested that PHS changed its motion at 2 to 4 Ma based on the geological evidences of temporal change in the regional stress field around the Honshu arc (Takahashi, 2006), the spatio-temporal change of volcanic front in the Chugoku district (Kimura et al., 2005), the distribution of active fault along the Median Tectonic Line (Ikeda et al., 2009), and plate reconstruction (e.g., Hall, 2002; Gaina and Muller, 2007). The abrupt event changed the PHS motion from northward to northwestward and slowed down the clockwise spin motion (Seno and Maruyama, 1984; Hall et al., 1995; Seno et al., 1993; Kimura et al., 2005; Gaina and Muller, 2007; Yamazaki et al., 2010), which indicates that
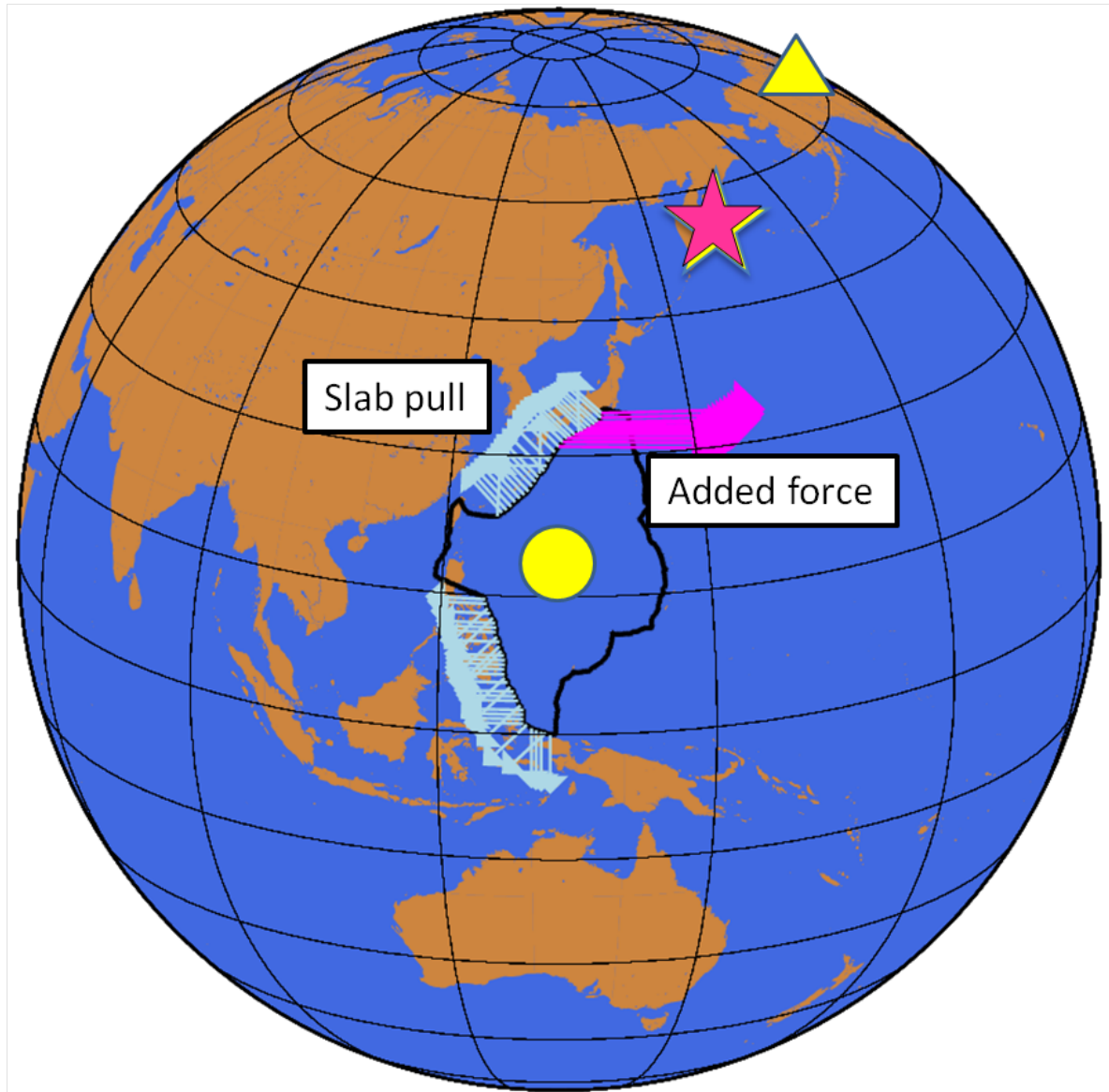
Fig. 4.8   Euler pole analysis of the PHS on a Lambert projection. Black line is the plate boundary of the PHS. Yellow star, triangle, and circle represent the observed Euler pole, the straight Euler pole, and the spin Euler pole, respectively. Light blue vectors are imposed a uniform effective slab pull. Pink vector is the added force arbitrarily chosen to reproduce the observed Euler pole. The vector length represented in this picture is arbitrary, yet the relative length between the blue and pink vectors is correct. All the Euler poles depicted here are negative Euler poles. For the observed Euler poles, hotspot reference frame is utilized (Gripp and Gordon, 2002).

some eastward force was applied along the northern edge of PHS. In addition, seismic observations revealed the contact zone between the PHS slab and the upper surface of the Pacific slab beneath the Kanto district (Nakajima et al., 2009), which might represent collision of the PHS slab to the Pacific slab around 3 Ma, having led to the significant deformation of the PHS slab beneath Kanto. This quick change of the plate motion might have caused the unique shape of the PHS slab, as was pointed out by Ide et al. (2010). However, during the continuous clockwise spin motion before the abrupt change, the PHS slab had received the driving force for the spin motion and therefore the slab deformation must have continued for a much longer period of time. Although the initiation age of the spin motion is not well resolved, a long-term tectonic reconstruction (e.g., Hall, 2002), including several events around PHS, such as the opening of the Japan sea, especially the clockwise motion of the southwestern Japan ($\sim$ 15 Ma) (e.g., Sato, 1994; Jolivet et al., 1994; Maruyama et al., 1997), the collision of the Izu arc into the Kanto district dated back to at least $\sim$ 17 Ma (Aoike, 1999), and the initiation of the subduction of the northern PHS plate ($\sim$ 20 Ma) (Hall, 2002) are consistent with our rough estimate of age, $\Delta t = 4$ to 19 Myr, and might be related to the initiation of slab buckling.

4.6   Discussion

4.6.1   Validity of torque analysis for the Philippine Sea plate

In our torque analysis for the PHS, we first imposed the uniform slab pull force based on the notion that the slab pull force generally succeed in simulating the observed Euler Pole (Forsyth and Uyeda, 1975; Becker and O'Connell, 2001). Actually, as we already stated above (Chapter 1), slab pull can simulate the observed Euler poles of almost all the plates and the straight motion of the other plates, such as the Philippine Sea and Cocos plate. For this reason, we first adopted the slab pull force. In addition, Forsyth and Uyeda (1975) and

Becker and O'Connell (2001) consider uniform slab pull force along the subduction zone and according to their analysis we also impose uniform slab pull force. The reason that the uniform slab pull force can generate the observed Euler pole might be associated with a mechanism in which the slab resistance increases as the increase in the driving slab pull. Then, to generate the PHS spin motion, we need to add a torque which has not been considered in the previous works (Forsyth and Uyeda, 1975; Becker and O'Connell, 2001). As the driving force Seno (2000) raised a mantle upwelling off the west coast of Kyushu, which is indicated based on the crustal stress variation in Kyushu region (Seno, 1999), the electrical conductivity (Shimoizumi et al., 1997; Handa, 2005) and seismic observations (Sadeghi et al., 2000; Yoshizawa et al., 2010), though he also suggested that the estimated magnitude of the torque caused by the upwelling may not be sufficient to simulate the observed plate spin motions and another driving force might be necessary. Another conceivable candidate for the driving force is the collision of the Caroline plate (Figure 4.9). The westward motion seems to push the southern part of the PHS and to induce the clockwise spin motion. However, the southern plate boundary between the two plates is ridge and the speed of westward motion of the PHS is faster than that of the Caroline plate. Thus, the Caroline plate cannot be a driving force for the spin motion of the PHS. Based on these considerations, we imposed uniform slab pull force along the subduction zone and added another force suggested by Seno (1999, 2000) in the torque analysis of the PHS.

4.6.2   Other possibilities of the wavy slab geometry

Although we assumed the wavy slab geometry as a buckling and applied the folding theory to the geometry, here we consider another possibility to induce the geometry of the PHS slab beneath the southwestern Japan. One candidate is the wavy plate boundary when the plate was subducting. Looking at the slab geometry, generally the geometry is the same as
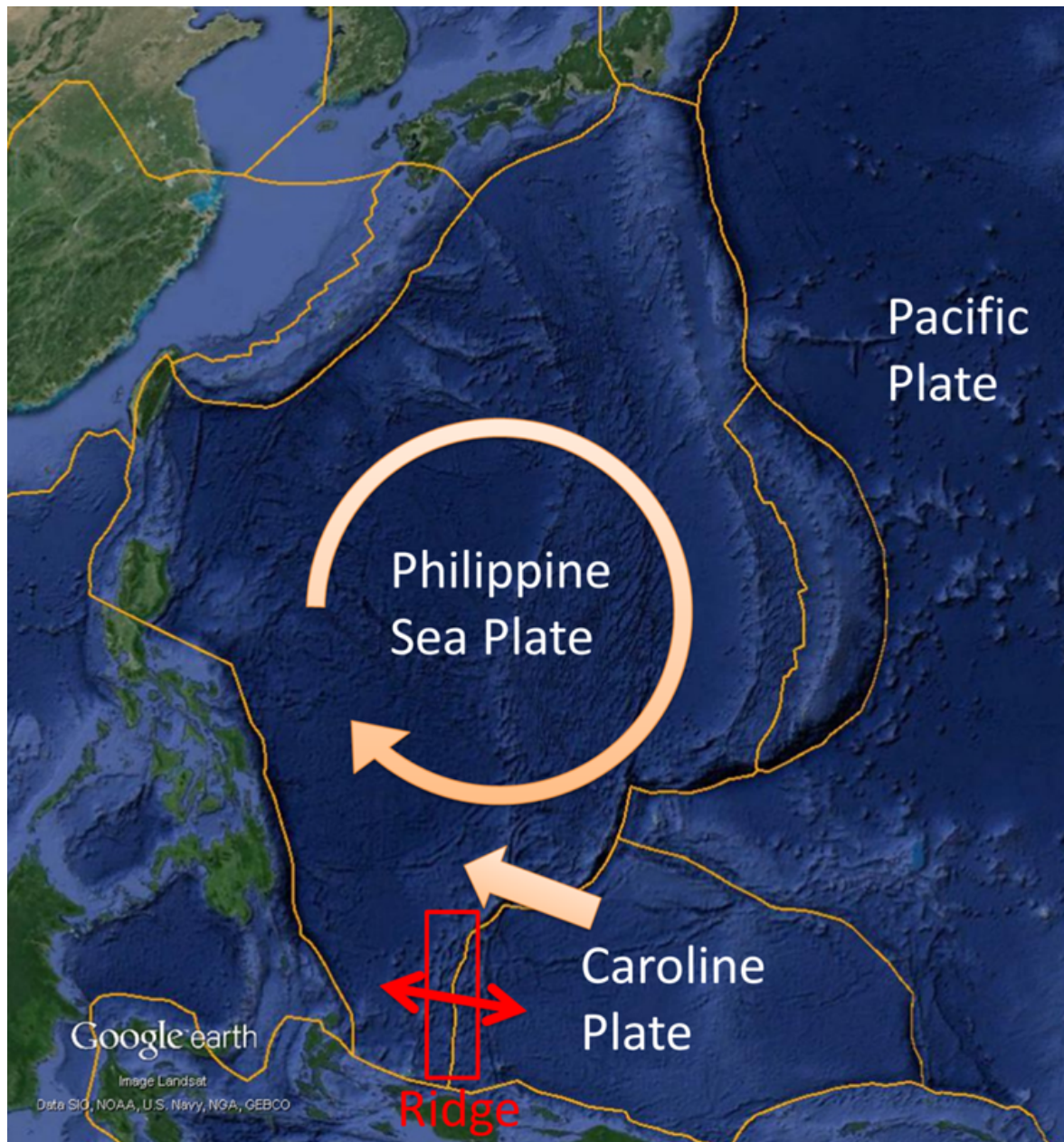
Fig. 4.9   Plate motion of the Caroline plate. Although the Caroline plate moves west-
ward, the westward motion of the Philippine Sea plate is faster and as a result, the plate
boundary between the two plates becomes ridge.

the shape of the plate boundary (Hayes et al., 2012). In fact, due to the collision of the PHS

at the Izu peninsula the plate boundary deforms and the slab subducted there has similar

geometry (Figure 4.2). However, the locations we focus on to analyze the slab geometry,

such as around Biwa Lake and Seto Island Sea, are not suggested to deform in these several

million years; therefore, it is not conceivable that a wavy plate boundary generated the current deformed slab geometry.

As regards the cause of the wavy slab, Ide et al. (2010) analyzed the slab geometry by dealing with the slab as an elastic media and suggested that the folding occurred sometime between 2–4 Ma, causing the split of the slab which they claimed to be observed in the current seismicity. Although they did not maintain the mechanism to split the slab suddenly, our analysis showed that approximately a few GPa (approximately one order higher than that of slab pull stress (Section 4.3.1)) is necessary to deform the elastic slab and it is difficult to think about any conceivable driving force in the interior of the Earth. For this reason, we suggest that the slab deformed after the subduction due to the buckling as a viscous media rather an elastic one.

4.6.3 Thermal condition of southwestern subduction zone and rheology of slab

Whereas we suggested that the slab beneath the southwestern Japan deforms as a viscous media, here we discuss the thermal condition of the subduction zone to consider whether or not the slab can behave as a viscous material in the circumstances. Compared with other subduction zone such as the northeastern Japan, the subduction zone of the southwestern Japan is suggested to be relatively "hotter" (Peacock and Wang, 1999; Iwamori, 2007) and the temperature of the slab at the depth of 40–60 km, at which the deformation of the PHS slab is largest (Figure 4.2), is estimated as approximately 500°C or more (500–600°C at the bottom of the oceanic crust (Peacock and Wang, 1999); 400–600°C along the slab-wedge interface (Iwamori, 2007)). Moreover, the thickness of a plate in which the lithosphere behaves as an elastic plate, i.e., the elastic thickness, accords the isotherm of 600°C (Watts and Zhong, 2000). Thus, the lithosphere of less than 600°C behaves elastically in a short time scale and viscously in a long time scale and that of more than 600°C

exhibits a viscous characteristic. Consequently, it is enough conceivable that the relatively hot slab beneath the southwestern Japan deformed as a viscous media to yield the current wavy geometry. We estimate the viscosity contrast between the slab and the mantle by theoretical formulation of rheology (Karato and Wu, 1993; Korenaga and Karato, 2008). In a simple case, in which we set temperature 500°C for the slab surface and 1000°C for the surrounding mantle, the depth 50km and the both rheologies wet diffusion creep, the viscosity contrast becomes roughly 10^9–10^{13} (Karato and Wu, 1993; Korenaga and Karato, 2008; Karato, 2010, 2011). The estimated viscosity contrast is large, yet several effects, such as water and the grain size, might play an important role to reduce such a large viscosity contrast.

4.7　Summary

We analyzed the geometry of the PHS slab beneath southwestern Japan using the theory of folding. We found that during the buckling process, the slab behaves as a viscous media, such as Newtonian or power-law, rather than an elastic slab and the viscosity of the slab is approximately 1–14×10^{23} Pa s. The simple Euler pole analysis provides an estimate on the driving force of the PHS spin motion, i.e., the eastward force of approximately 4–40 MPa. This range is within the stress level that can be sustained by the plate boundary as was discussed in Chapter 3, although the exact relation between the two estimates are not clear at present. While there is a large uncertainty of our estimate of the time took for the buckling ($\Delta t = 4$–19 Myr), important events around the PHS, including the quick change of the PHS motion (~ 4 Ma), the clockwise motion of the southwestern Japan for the opening of the Japan Sea (~ 15 Ma) (e.g., Sato, 1994; Jolivet et al., 1994), the collision of the Izu arc into the Kanto district (~ 17 Ma) (Aoike, 1999), and the initiation of the subduction of the northern PHS plate (~ 20 Ma) (Hall, 2002), may be important to understand the evolution

of the PHS and slab, as well as tectonic evolution around the Japan arcs.

Chapter 5

Summary and conclusion

In previous works, numerical simulations of mantle convection have been used to examine the extent to which toroidal velocity components are naturally generated on the surface, by varying key parameters, notably the rheological properties of plates and plate boundaries. Here, we took the reverse approach and performed analysis of observed plate motions with high-resolution plate models to constrain the physical properties and to comprehend the dynamics of plate motions. We analyzed (i) toroidal/poloidal ratio of global plate motion, (ii) spin motions of individual plates without a slab and (iii) the Philippine Sea plate with both a high spin rate and subducting slab.

In the toroidal-poloidal analysis, although previous works (e.g., O'Connell et al., 1991) suggested the toroidal/poloidal ratio is almost constant (~ 0.8) for both low and high degrees of spherical harmonic expansion, our detailed analysis up to much higher degrees than ever demonstrated that there is an increase in the ratio especially from 1000 km in the scale of motion (Figure 2.3), which results from the plate motion, in particular, spin motion of small plate, and the plate geometrical configuration as shown in Appendix C.

To comprehend the driving force of plate spin motions, which have not been explained in previous works (Forsyth and Uyeda, 1975; Becker and O'Connell, 2001), we analyzed individual plate spin motions. Focusing on the plates without a subducting slab, we found

that there is a rapid change in the rotation rate of spin motion around 1000 km in plate size. Since a fast-moving plate drives the adjacent small plates via the mechanical interaction at plate boundaries, as is seen in the global geographical distribution of spin motion (Figure 3.6), this quantitative relationship constrains strength of the plate boundaries as 3 to 75 MPa (Figure 3.7), which is consistent with several seismological observations, including those from the northeastern Japan arc associated with the 2011 Tohoku earthquake.

Finally, we investigated forces driving the motion of the Philippine Sea plate (PHS) with both a relatively high spin rate and subducting slabs. By applying the theory of folding to explain the wavy geometry of the subducted PHS slab beneath the southwestern Japan arc, we found that the slab behaves as a viscous layer during the deformation with viscosity to be 1 to 14×10^{23} Pa s. Assuming a mantle flow beneath the Kyushu district as the source of driving force for slab deformation as well as the spin motion of PHS (Seno, 2000), we estimated the stress to be 4 to 40 MPa, which is within our estimate on the strength of plate boundaries, suggesting a relatively weak regime for the overall driving force of plate motions.

Acknowledgements

I would like to express my sincere gratitude to my supervisor, Professor Hikaru Iwamori for his advices and encouragement throughout this study. I would also like to show my appreciation to Professor Hideo Tsunakawa, Professor Taishi Nakamoto, Professor Jun'ichi Nakajima and Professor Yuichiro Ueno for their critical and constructive comments which significantly improved this thesis. Moreover, I am deeply grateful to all the people in Iwamori Laboratory for their fruitful comments and kind cooperation to my study. Furthermore, I would like to offer my special thanks to all the students and the stuffs in this department, Department of Earth and Planetary Sciences. With them, I really enjoyed my best school life. Finally, I owe my deepest gratitude to my family for their thoughtful consideration to my circumstances.

Without one of them, I could not complete my doctoral degree. I would like to show my greatest appreciation to all of them.

Bibliography

Anderson-Fontana, S., Engeln, J. F., Lundgren, P., Larson, R. L., and Stein, S. (1986). Tectonics and evolution of the juan fernandez microplate at the pacific-nazca-antarctic triple junction. *Journal of Geophysical Research: Solid Earth*, 91(B2):2005–2018.

Aoike, K. (1999). Tectonic evolution of the izu collision zone. *Research Report of the Kanagawa Prefectural Museum of Natural History*, 9:111–151.

Argus, D. F., Gordon, R. G., and DeMets, C. (2011). Geologically current motion of 56 plates relative to the no-net-rotation reference frame. *Geochemistry, Geophysics, Geosystems*, 12.

Baba, T., Tanioka, Y., Cummins, P. R., and Uhira, K. (2002). The slip distribution of the 1946 nankai earthquake estimated from tsunami inversion using a new plate model. *Physics of the Earth and Planetary Interiors*, 132:59 – 73. Subduction Zone Structure and Megathrust Earthquakes.

Becker, T. and O'Connell, R. (2001). Predicting plate velocities with mantle circulation models. *Geochemistry, Geophysics, Geosystems*, 2:2001GC000171.

Beghein, C. and Trampert, J. (2004). Probability density functions for radial anisotropy: implications for the upper 1200 km of the mantle. *Earth Planet. Sci. Lett.*, 217:151–162.

Benard, H. (1901). Les tourbillons cellulaires dans une nappe liquide. - methodes optiques d'observation et d'enregistrement. *J. Phys. Theor. Appl.*, 10(1):254–266.

Bercovici, D. (1993). A simple model of plate generation from mantle convection. *Geophys. J. Int.*, 114:635–650.

Bercovici, D. (1995a). On the purpose of toroidal motion in a convecting mantle. *Geophys. Res. Lett.*, 22:3107–3110.

Bercovici, D. (1995b). A source-sink model of the generation of plate tectonics from non-newtonian mantle flow. *J. Geophys. Res.*, 100:2013–2030.

Bercovici, D. (2003). The generation of plate tectonics from mantle convection. *Earth Planet. Sci. Lett.*, 205:107–121.

Bercovici, D. and Ricard, Y. (2014). Plate tectonics, damage and inheritance. *Nature*, 508:513–516.

Bercovici, D. and Wessel, P. (1994). A continuous kinematic model of plate-tectonic motions. *Geophys. J. Int.*, 119:595–610.

Biot, M. A. (1961). Theory of folding of stratified viscoelastic media and its implications in tectonics and orogenesis. *Geological Society of America Bulletin*, 72(11):1595–1620.

Biot, M. A. (1965). Further development of the theory of internal buckling of multilayers. *Geological Society of America Bulletin*, 76(7):833–840.

Bird, P. (2003). An updated digital model of plate boundaries. *Geochemistry, Geophysics, Geosystems*, 4(3):1027.

Caldwell, J. G. and Turcotte, D. L. (1979). Dependence of the thickness of the elastic oceanic lithosphere on age. *Journal of Geophysical Research: Solid Earth*, 84(B13):7572–7576.

Carpenter, B. M., Marone, C., and Saffer, D. M. (2011). Weakness of the san andreas fault revealed by samples from the active fault zone. *Nature Geoscience*, 4:251–254.

Chandrasekhar, S. (1961). *Hydrodynamic and Hydromagnetic Stability*. University Press, Oxford.

Chu, D. and Gordon, R. G. (1999). Evidence for motion between nubia and somalia along the southwest indian ridge. *Nature*, 398(6722):64–67.

Circum-Pacific Map Project (1986). *Plate-Tectonic Map of the Circum-Pacific Region.* edited by M. T. halbouty et al., 5 sheets at 1:10,000,000 and 1 sheet at 1:20,000,000, Amer. Assoc. Petr. Geol., Tulsa, Okla.

Conrad, C. P. and Lithgow-Bertelloni, C. (2002). How mantle slabs drive plate tectonics. *Science*, 298(5591):207–209.

Cook, D. B., Fujita, K., and McMullen, C. A. (1986). Proceedings of the symposium polar geophysics present-day plate interactions in northeast asia: North american, eurasian, and okhotsk plates. *Journal of Geodynamics*, 6(1):33 – 51.

DeMets, C., Gordon, R. G., Argus, D. F., and Stein, S. (1994). Effect of recent revisions to the geomagnetic reversal time scale on estimates of current plate motions. *Geophysical Research Letters*, 21(20):2191–2194.

DeMets, C. and Traylen, S. (2000). Motion of the rivera plate since 10 ma relative to the pacific and north american plates and the mantle. *Tectonophysics*, 318:119 – 159.

Di Giuseppe, E., van Hunen, J., Funiciello, F., Faccenna, C., and Giardini, D. (2008). Slab stiffness control of trench motion: Insights from numerical models. *Geochemistry, Geophysics, Geosystems*, 9(2). Q02014.

Dziewonski, A. and Anderson, D. (1981). Preliminary reference earth model. *Phys. Earth Planet. Inter.*, 25:297–356.

Dziewonski, A. M., Chou, T.-A., and Woodhouse, J. H. (1981). Determination of earthquake source parameters from waveform data for studies of global and regional seismicity. *J. Geophys. Res.*, 86:2825–2852.

Ekstrom, G., Nettles, M., and Dziewonski, A. M. (2012). The global cmt project 2004-2010: Centroid-moment tensors for 13,017 earthquakes. *Physics of the Earth and Planetary Interiors*, 200-201:1 – 9.

Engeln, J. F. and Stein, S. (1984). Tectonics of the easter plate. *Earth and Planetary Science*

Letters, 68(2):259 – 270.

Evans, R. L., Hirth, G., Baba, K., Forsyth, D., Chave, A., and Mackie, R. (2005). Geophysical evidence from the melt area for compositional controls on oceanic plates. *Nature*, 437:249–252.

Fletcher, R. C. (1974). Wavelength selection in the folding of a single layer with power-law rheology. *American Journal of Science*, 274(9):1029–1043.

Forsyth, D. and Uyeda, S. (1975). On the relative importance of the driving forces of plate motion. *Geophys. J. R. astr. Soc.*, 43:163–200.

Forte, A. and Mitrovica, J. (2001). Deep-mantle high-viscosity flow and thermochemical structure inferred from seismic and geodynamic data. *Nature*, 410:1049–1056.

Funiciello, F., Faccenna, C., Heuret, A., Lallemand, S., Giuseppe, E. D., and Becker, T. (2008). Trench migration, net rotation and slab-mantle coupling. *Earth and Planetary Science Letters*, 271:233 – 240.

Gaina, C. and Muller, D. (2007). Cenozoic tectonic and depth/age evolution of the indonesian gateway and associated back-arc basins. *Earth-Science Reviews*, 83:177 – 203.

Gorbatov, A. and Fukao, Y. (2005). Tomographic search for missing link between the ancient farallon subduction and the present cocos subduction. *Geophysical Journal International*, 160(3):849–854.

Gordon, R. (1998). The plate tectonic approximation: Plate nonrigidity, diffuse plate boundaries, and global plate reconstructions. *Annual Review of Earth and Planetary Science*, 26:615–642.

Gordon, R. (2000). Diffuse oceanic plate boundaries: Strain rates, vertically averaged rheology and comparisons with narrow plate boundaries and stable interiors. In Richards, M., Gordon, R., and van der Hilst, R., editors, *History and Dynamics of Global Plate Motions*, pages 143–159. American Geophysical Union, Washington, DC.

Gripp, A. and Gordon, R. (2002). Young track of hotspots and current plate velocities. *Geophys. J. Int.*, 150:321–361.

Hager, B. and O'Connell, R. (1978). Subduction zone dip angles and flow driven by plate motion. *Tectonophysics*, 50:111–133.

Hall, P. S. (2012). On the thermal evolution of the mantle wedge at subduction zones. *Physics of the Earth and Planetary Interiors*, 198-199:9 – 27.

Hall, R. (2002). Cenozoic geological and plate tectonic evolution of se asia and the sw pacific: computer-based reconstructions, model and animations. *J. Asian Earth Sci.*, 20:353–431.

Hall, R., Ali, J. R., Anderson, C. D., and Baker, S. J. (1995). Origin and motion history of the philippine sea plate. *Tectonophysics*, 251:229 – 250. Southeast Asia Structure and Tectonics.

Handa, S. (2005). Electrical conductivity structures estimated by thin sheet inversion, with special attention to the beppu-shimabara graben in central kyushu, japan. *Earth, Planets and Space*, 57(7):605–612.

Hardebeck, J. L. and Hauksson, E. (2001). Crustal stress field in southern california and its implications for fault mechanics. *J. Geophys. Res.*, 106:21859–21882.

Hasegawa, A., Yoshida, K., Asano, Y., Okada, T., Iinuma, T., and Ito, Y. (2012). Change in stress field after the 2011 great tohoku-oki earthquake. *Earth and Planetary Science Letters*, 355-356:231 – 243.

Hayes, G. P., Wald, D. J., and Johnson, R. L. (2012). Slab1.0: A three-dimensional model of global subduction zone geometries. *Journal of Geophysical Research: Solid Earth*, 117(B1). B01302.

Heki, K., Miyazaki, S., Takahashi, H., Kasahara, M., Kimata, F., Miura, S., Vasilenko, N. F., Ivashchenko, A., and An, K.-D. (1999). The amurian plate motion and current plate kine-

matics in eastern asia. *Journal of Geophysical Research: Solid Earth*, 104(B12):29147–29155.

Hirose, F., Nakajima, J., and Hasegawa, A. (2008). Three-dimensional seismic velocity structure and configuration of the philippine sea slab in southwestern japan estimated by double-difference tomography. *Journal of Geophysical Research: Solid Earth*, 113(B9). B09315.

Holmes, A. (1928). *The nomenclature of petrology, with references to selected literature.* Thomas Murby anc Co, London, 2nd edition edition.

Hudleston, P. J. and Treagus, S. H. (2010). Information from folds: A review. *Journal of Structural Geology*, 32(12):2042 – 2071. Structural Diagenesis.

Ide, S., Shiomi, K., Mochizuki, K., Tonegawa, T., and Kimura, G. (2010). Split philippine sea plate beneath japan. *Geophysical Research Letters*, 37(21). L21304.

Iidaka, T., Igarashi, T., and Iwasaki, T. (2009). Configuration of the subducting philippine sea slab in the eastern part of southwestern japan with seismic array and hi-net data. *Gondwana Research*, 16:504 – 511.

Ikeda, M., Toda, S., Kobayashi, S., Ohno, Y., Nishizaka, N., and Ohno, I. (2009). Tectonic model and fault segmentation of the median tectonic line active fault system on shikoku, japan. *Tectonics*, 28(5). TC5006.

Iwamori, H. (1998). Transportation of h2o and melting in subduction zones. *Earth and Planetary Science Letters*, 160:65 – 80.

Iwamori, H. (2007). Transportation of h2o beneath the japan arcs and its implications for global water circulation. *Chemical Geology*, 239:182 – 198. Geochemical processes responsible for element mobility from the slab to the surfaceSelected papers from the 15th Goldschmidt Conference held at Moscow, Idaho, USA, 20 - 25 May 2005.

Iwamori, H., Richardson, C., and Maruyama, S. (2007). Numerical modeling of thermal

structure, circulation of h2o, and magmatism-metamorphism in subduction zones: Implications for evolution of arcs. *Gondwana Research*, 11:109 – 119. Island Arcs: Past and Present.

Iwamori, H. and Zhao, D. (2000). Melting and seismic structure beneath the northeast japan arc. *Geophysical Research Letters*, 27(3):425–428.

Jolivet, L., Tamaki, K., and Fournier, M. (1994). Japan sea, opening history and mechanism: A synthesis. *Journal of Geophysical Research: Solid Earth*, 99(B11):22237–22259.

Karato, S. (2010). Rheology of the deep upper mantle and its implications for the preservation of the continental roots: A review. *Tectonophysics*, 481:82 – 98. Insights into the Earth's Deep Lithosphere.

Karato, S. (2011). Water distribution across the mantle transition zone and its implications for global material circulation. *Earth and Planetary Science Letters*, 301:413 – 423.

Karato, S. (2012). On the origin of the asthenosphere. *Earth Planet. Sci. Lett.*, 321-322:95– 103.

Karato, S., Riedel, M. R., and Yuen, D. A. (2001). Rheological structure and deformation of subducted slabs in the mantle transition zone: implications for mantle circulation and deep earthquakes. *Physics of the Earth and Planetary Interiors*, 127:83 – 108. Processes and Consequences of Deep Subduction.

Karato, S. and Wu, P. (1993). Rheology of the upper mantle: a synthesis. *Science*, 260:771– 778.

Kato, T., Kotake, Y., Nakao, S., Beavan, J., Hirahara, K., Okada, M., Hoshiba, M., Kamigaichi, O., Feir, R. B., Park, P. H., Gerasimenko, M. D., and Kasahara, M. (1998). Initial results from wing, the continuous gps network in the western pacific area. *Geophysical Research Letters*, 25(3):369–372.

Kawakatsu, H., Kumar, P., Takei, Y., Shinohara, M., Kanazawa, T., Araki, E., and K., S. (2009).

Seismic evidence for sharp lithosphere   asthenosphere boundaries of oceanic plates. *Science*, 324:499–502.

Kellogg, J. N., Vega, V., Stailings, T. C., Aiken, C. L., and Kellogg, J. N. (1995). Tectonic development of panama, costa rica, and the colombian andes: Constraints from global positioning system geodetic studies and gravity. *Geological Society of America Special Papers*, 295:75–90.

Kimura, J.-I., Stern, R. J., and Yoshida, T. (2005). Reinitiation of subduction and magmatic responses in sw japan during neogene time. *Geological Society of America Bulletin*, 117(7-8):969–986.

Kita, S., Okada, T., Hasegawa, A., Nakajima, J., and Matsuzawa, T. (2010). Anomalous deepening of a seismic belt in the upper-plane of the double seismic zone in the pacific slab beneath the hokkaido corner: Possible evidence for thermal shielding caused by subducted forearc crust materials. *Earth and Planetary Science Letters*, 290:415 – 426.

Kohlstedt, D., Evans, B., and Mackwell, S. (1995). Strength of the lithosphere: constraints imposed by laboratory measurements. *J. Geophys. Res.*, 100:17587–17602.

Korenaga, J. and Karato, S.-I. (2008). A new analysis of experimental data on olivine rheology. *Journal of Geophysical Research: Solid Earth*, 113(B2). B02403.

Kreemer, C., Blewitt, G., and Klein, E. C. (2014). A geodetic plate motion and Global Strain Rate Model. *Geochemistry, Geophysics, Geosystems*, 15(10):3849–3889.

Kusuda, C., Iwamori, H., Nakamura, H., Kazahaya, K., and Morikawa, N. (2014). Arima hot spring waters as a deep-seated brine from subducting slab. *Earth, Planets and Space*, 66(1):119.

Lamb, S. (2000). Active deformation in the bolivian andes, south america. *Journal of Geophysical Research: Solid Earth*, 105(B11):25627–25653.

Laravie, J. A. (1975). Geometry and lateral strain of subducted plates in island arcs. *Geol-*

ogy, 3(9):484–486.

Lithgow-Bertelloni, C. and Richards, M. (1993). Toroidal-poloidal partitioning of plate motions since 120 ma. *Geophys. Res. Lett.*, 20:375–378.

Lonsdale, P. (1988). Structural pattern of the galapagos microplate and evolution of the galapagos triple junctions. *Journal of Geophysical Research: Solid Earth*, 93(B11):13551–13574.

Martinez, F. and Taylor, B. (1996). Backarc spreading, rifting, and microplate rotation, between transform faults in the manus basin. *Marine Geophysical Researches*, 18(2):203–224.

Maruyama, S., Isozaki, Y., Kimura, G., and Terabayashi, M. (1997). Paleogeographic maps of the japanese islands: Plate tectonic synthesis from 750 ma to the present. *Island Arc*, 6(1):121–142.

McClusky, S., Balassanian, S., Barka, A., Demir, C., Ergintav, S., Georgiev, I., Gurkan, O., Hamburger, M., Hurst, K., Kahle, H., Kastens, K., Kekelidze, G., King, R., Kotzev, V., Lenk, O., Mahmoud, S., Mishin, A., Nadariya, M., Ouzounis, A., Paradissis, D., Peter, Y., Prilepin, M., Reilinger, R., Sanli, I., Seeger, H., Tealeb, A., Toksoz, M. N., and Veis, G. (2000). Global positioning system constraints on plate kinematics and dynamics in the eastern mediterranean and caucasus. *Journal of Geophysical Research: Solid Earth*, 105(B3):5695–5719.

McKenzie, D. and Bickle, M. J. (1988). The volume and composition of melt generated by extension of the lithosphere. *Journal of Petrology*, 29(3):625–679.

Morgan, W. J. (1972). Plate motions and deep mantle convection. *Geological Society of America Memoirs*, 132:7–22.

Nakajima, J. and Hasegawa, A. (2006). Anomalous low-velocity zone and linear alignment of seismicity along it in the subducted pacific slab beneath kanto, japan: Reactivation

of subducted fracture zone? *Geophysical Research Letters*, 33(16). L16309.

Nakajima, J. and Hasegawa, A. (2007). Subduction of the philippine sea plate beneath southwestern japan: Slab geometry and its relationship to arc magmatism. *Journal of Geophysical Research: Solid Earth*, 112(B8). B08306.

Nakajima, J., Hirose, F., and Hasegawa, A. (2009). Seismotectonics beneath the tokyo metropolitan area, japan: Effect of slab-slab contact and overlap on seismicity. *Journal of Geophysical Research: Solid Earth*, 114(B8). B08309.

O'Connell, R., Gable, C., and Hager, B. (1991). Toroidal-poloidal partitioning of lithospheric plate motion. In Sabadini, R., Lambeck, K., and Boschi, E., editors, *Glacial Isostasy, Sea Level and Mantle Rheology*, pages 535–551. Springer Netherlands, Dordrecht.

Okino, K., Ohara, Y., Kasuga, S., and Kato, Y. (1999). The philippine sea: New survey results reveal the structure and the history of the marginal basins. *Geophysical Research Letters*, 26(15):2287–2290.

Okino, K., Shimakawa, Y., and Nagaoka, S. (1994). Evolution of the shikoku basin. *Journal of geomagnetism and geoelectricity*, 46(6):463–479.

Oldenburg, D. W. and Brune, J. N. (1972). Ridge transform fault spreading pattern in freezing wax. *Science*, 178(4058):301–304.

Olson, P. and Bercovici, D. (1991). On the equipartition of kinetic energy in plate tectonics. *Geophys. Res. Lett.*, 18:1751–1754.

Peacock, S. M. and Wang, K. (1999). Seismic consequences of warm versus cool subduction metamorphism: Examples from southwest and northeast japan. *Science*, 286(5441):937–939.

Pelayo, A. M. and Wiens, D. A. (1989). Seismotectonics and relative plate motions in the scotia sea region. *Journal of Geophysical Research: Solid Earth*, 94(B6):7293–7320.

Peltier, W. R. (1998). Postglacial variations in the level of the sea: Implications for climate dynamics and solid-earth geophysics. *Rev. Geophys.*, 36:603–689.

Perry, J. (1895a). On the age of the earth. *Nature*, 51:224–227.

Perry, J. (1895b). On the age of the earth. *Nature*, 51:341–342.

Perry, J. (1895c). On the age of the earth. *Nature*, 51:582–585.

Rangin, C., Le Pichon, X., Mazzotti, S., Pubellier, M., Chamot-Rooke, N., Aurelio, M., Walpersdorf, A., and Quebral, R. (1999). Plate convergence measured by gps across the sundaland/philippine sea plate deformed boundary: the philippines and eastern indonesia. *Geophysical Journal International*, 139(2):296–316.

Ricard, Y., Doglioni, C., and Sabadini, R. (1991). Differential rotation between lithosphere and mantle: a consequence of lateral mantle viscosity variations. *J. Geophys. Res.*, 96:8407–8415.

Richards, M., Yang, W., Baumgardner, J., and Bunge, H. (2001). Role of a low-viscosity zone in stabilizing plate tectonics: Implications for comparative terrestrial planetology. *Geochemistry, Geophysics, Geosystems*, 3:2000GC000115.

Sadeghi, H., Suzuki, S., and Takenaka, H. (2000). Tomographic low-velocity anomalies in the uppermost mantle around the northeastern edge of okinawa trough, the backarc of kyushu. *Geophysical Research Letters*, 27(2):277–280.

Sano, Y., Kameda, A., Takahata, N., Yamamoto, J., and Nakajima, J. (2009). Tracing extinct spreading center in sw japan by helium-3 emanation. *Chemical Geology*, 266:50 – 56. Geochemical Applications of Noble Gases.

Sato, H. (1994). The relationship between late cenozoic tectonic events and stress field and basin development in northeast japan. *Journal of Geophysical Research: Solid Earth*, 99(B11):22261–22274.

Schellart, W. (2009). Evolution of the slab bending radius and the bending dissipation in

three-dimensional subduction models with a variable slab to upper mantle viscosity ratio. *Earth and Planetary Science Letters*, 288:309 – 319.

Schellart, W. P. (2008). Kinematics and flow patterns in deep mantle and upper mantle subduction models: Influence of the mantle depth and slab to mantle viscosity ratio. *Geochemistry, Geophysics, Geosystems*, 9(3). Q03014.

Schmalholz, S. M. and Podladchikov, Y. (1999). Buckling versus folding: Importance of viscoelasticity. *Geophysical Research Letters*, 26(17):2641–2644.

Schouten, H., Klitgord, K., and Gallo, D. (1993). Edge-driven microplate kinematics. *J. Geophys. Res.*, 98:6689–6701.

Seno, T. (1999). Syntheses of the regional stress fields of the japanese islands. *Island Arc*, 8(1):66–79.

Seno, T. (2000). Why the philippine sea plate moves as it does. *J. Geol. Soc. Phil.*, 55:105–117.

Seno, T. and Maruyama, S. (1984). Paleogeographic reconstruction and origin of the philippine sea. *Tectonophysics*, 102:53 – 84. Geodynamics of Back-Arc Regions.

Seno, T., Stein, S., and Gripp, A. E. (1993). A model for the motion of the philippine sea plate consistent with nuvel-1 and geological data. *Journal of Geophysical Research: Solid Earth*, 98(B10):17941–17948.

Shimoizumi, M., Mogi, T., Nakada, M., Yukutake, T., Handa, S., Tanaka, Y., and Utada, H. (1997). Electrical conductivity anomalies beneath the western sea of kyushu, japan. *Geophysical Research Letters*, 24(13):1551–1554.

Shiomi, K., Matsubara, M., Ito, Y., and Obara, K. (2008). Simple relationship between seismic activity along philippine sea slab and geometry of oceanic moho beneath southwest japan. *Geophysical Journal International*, 173(3):1018–1029.

Shiomi, K., Sato, H., Obara, K., and Ohtake, M. (2004). Configuration of subducting philip-

pine sea plate beneath southwest japan revealed from receiver function analysis based on the multivariate autoregressive model. *Journal of Geophysical Research: Solid Earth*, 109(B4). B04308.

Shiono, K. (1982). Frontal shape of the seismic slab by normal subduction of a dead spreading axis and a preliminary application to southwest japan. *Journal of geosciences, Osaka City University*, 25:19–33.

Sibson, R. H. (2003). Thickness of the seismic slip zone. *Bulletin of the Seismological Society of America*, 93(3):1169–1178.

Simons, M. and Hager, B. (1997). Localization of the gravity field and the signature of glacial rebound. *Nature*, 390:500–504.

Smith, R. B. (1975). Unified theory of the onset of folding, boudinage, and mullion structure. *Geological Society of America Bulletin*, 86(11):1601–1609.

Smith, R. B. (1977). Formation of folds, boudinage, and mullions in non-newtonian materials. *Geological Society of America Bulletin*, 88(2):312–320.

Soh, W., Nakayama, K., and Kimura, T. (1998). Arc-arc collision in the izu collision zone, central japan, deduced from the ashigara basin and adjacent tanzawa mountains. *Island Arc*, 7(3):330–341.

Stein, C. A. and Stein, S. (1992). A model for the global variation in oceanic depth and heat flow with lithospheric age. *Nature*, 359(6391):123–129.

Strutt John William (Lord Rayleigh) (1916). Lix. on convection currents in a horizontal layer of fluid, when the higher temperature is on the under side. *Philosophical Magazine Series 6*, 32(192):529–546.

Tackley, P. (2000a). Self-consistent generation of tectonic plates in time-dependent, three-dimensional mantle convection simulations 1. pseudoplastic yielding. *Geochemistry, Geophysics, Geosystems*, 1:2000GC000036.

Tackley, P. (2000b). Self-consistent generation of tectonic plates in time-dependent, three-dimensional mantle convection simulations 2. strain weakening and asthenosphere. *Geochemistry, Geophysics, Geosystems*, 1:2000GC000043.

Takahashi, M. (2006). Tectonic development of the japanese islands controlled by philippine sea plate motion. *Journal of Geography (Chigaku Zasshi)*, 115(1):116–123.

Tregoning, P., Jackson, R. J., McQueen, H., Lambeck, K., Stevens, C., Little, R. P., Curley, R., and Rosa, R. (1999). Motion of the south bismarck plate, papua new guinea. *Geophysical Research Letters*, 26(23):3517–3520.

Tregoning, P., Lambeck, K., Stolz, A., Morgan, P., McClusky, S. C., van der Beek, P., McQueen, H., Jackson, R. J., Little, R. P., Laing, A., and Murphy, B. (1998). Estimation of current plate motions in papua new guinea from global positioning system observations. *Journal of Geophysical Research: Solid Earth*, 103(B6):12181–12203.

Trenkamp, R., Kellogg, J. N., and Freymueller, J. T. (1996). Transect of nazca-south america plate boundary in ecuador and colombia - 8 years of casa gps results (abstract). *Eos, Transactions American Geophysical Union*, 77(46).

Turcotte, D. L. and Oxburgh, E. R. (1972). Mantle convection and the new global tectonics. *Annual Review of Fluid Mechanics*, 4(1):33–66.

Turcotte, D. L. and Schubert, G. (2002). *Geodynamics.* Cambridge University Press, New York, 2nd edition edition.

Ueno, T., Shibutani, T., and Ito, K. (2008). Configuration of the continental moho and philippine sea slab in southwest japan derived from receiver function analysis: Relation to subcrustal earthquakes. *Bulletin of the Seismological Society of America*, 98(5):2416–2427.

Umeda, K., Kusano, T., Asamori, K., and McCrank, G. F. (2012). Relationship between 3he/4he ratios and subduction of the philippine sea plate beneath southwest japan.

Journal of Geophysical Research: Solid Earth, 117(B10). B10204.

Watts, A. B. and Zhong, S. (2000). Observations of flexure and the rheology of oceanic lithosphere. *Geophysical Journal International*, 142(3):855–875.

Weber, J. C., Dixon, T. H., DeMets, C., Ambeh, W. B., Jansma, P., Mattioli, G., Saleh, J., Sella, G., Bilham, R., and Perez, O. (2001). Gps estimate of relative motion between the caribbean and south american plates, and geologic implications for trinidad and venezuela. *Geology*, 29(1):75–78.

Wilson, D. S. (1988). Tectonic history of the juan de fuca ridge over the last 40 million years. *Journal of Geophysical Research: Solid Earth*, 93(B10):11863–11876.

Wu, X., Collilieux, X., Altamimi, Z., Vermeersen, B. L. A., Gross, R. S., and Fukumori, I. (2011). Accuracy of the international terrestrial reference frame origin and earth expansion. *Geophysical Research Letters*, 38(13). L13304.

Yamazaki, T., Takahashi, M., Iryu, Y., Sato, T., Oda, M., Takayanagi, H., Chiyonobu, S., Nishimura, A., Nakazawa, T., and Ooka, T. (2010). Philippine sea plate motion since the eocene estimated from paleomagnetism of seafloor drill cores and gravity cores. *Earth, Planets and Space*, 62(6):495–502.

Yingjie, Y., Forsyth, D. W., and Weeraratne, D. S. (2007). Seismic attenuation near the east pacific rise and the origin of the low-velocity zone. *Earth Planet. Sci. Lett.*, 258:260–268.

Yoshioka, S. and Ito, Y. (2001). Lateral variations of effective elastic thickness of the subducting philippine sea plate along the nankai trough. *Earth, Planets and Space*, 53(4):261–273.

Yoshizawa, K., Miyake, K., and Yomogida, K. (2010). 3d upper mantle structure beneath japan and its surrounding region from inter-station dispersion measurements of surface waves. *Physics of the Earth and Planetary Interiors*, 183:4 – 19. Special Issue on Deep Slab and Mantle Dynamics.

Zellmer, K. E. and Taylor, B. (2001). A three-plate kinematic model for lau basin opening. *Geochemistry, Geophysics, Geosystems*, 2(5). 1020.

Appendix A

Theory of spherical harmonic expansion

A.1 Condition of toroidal-poloidal decomposition

The condition for the toroidal-poloidal decomposition is that the divergence is zero everywhere in the vector field. In fact, the divergence of toroidal-poloidal flow becomes

$$\operatorname{div} \boldsymbol{u} = \operatorname{div} (\boldsymbol{u}_T + \boldsymbol{u}_P) = \operatorname{div} \boldsymbol{u}_T + \operatorname{div} \boldsymbol{u}_P = 0,$$

where

$$
\begin{aligned}
\operatorname{div} \boldsymbol{u}_T &= \frac{1}{r^2} \frac{\partial \left(r^2 u_{Tr} \right)}{\partial r} + \frac{1}{r \sin\theta} \frac{\partial \left(\sin\theta\, u_{T\theta} \right)}{\partial \theta} + \frac{1}{r \sin\theta} \frac{\partial u_{T\phi}}{\partial \phi} \\
&= \frac{1}{r^2} \frac{\partial 0}{\partial r} + \frac{1}{r \sin\theta} \frac{\partial}{\partial \theta} \left(\frac{1}{r} \frac{\partial \Psi}{\partial \phi} \right) + \frac{1}{r \sin\theta} \frac{\partial}{\partial \phi} \left(-\frac{1}{r} \frac{\partial \Psi}{\partial \theta} \right) \\
&= 0 + \frac{1}{r^2 \sin\theta} \frac{\partial^2 \Psi}{\partial \theta \partial \phi} - \frac{1}{r^2 \sin\theta} \frac{\partial^2 \Psi}{\partial \phi \partial \theta} \\
&= 0
\end{aligned}
$$

and

$$\text{div}\,\boldsymbol{u}_P = \frac{1}{r^2}\frac{\partial\left(r^2 u_{Pr}\right)}{\partial r} + \frac{1}{r\sin\theta}\frac{\partial\left(\sin\theta\, u_{P\theta}\right)}{\partial\theta} + \frac{1}{r\sin\theta}\frac{\partial u_{P\phi}}{\partial\phi}$$

$$= \frac{1}{r^2}\frac{\partial\left(-r^2\Delta_H\Phi\right)}{\partial r} + \frac{1}{r\sin\theta}\frac{\partial}{\partial\theta}\left(\frac{\sin\theta}{r}\frac{\partial}{\partial\theta}\left(\frac{\partial\Phi}{\partial r}\right)\right) + \frac{1}{r\sin\theta}\frac{\partial}{\partial\phi}\left(\frac{1}{r\sin\theta}\frac{\partial}{\partial\phi}\left(\frac{\partial\Phi}{\partial r}\right)\right)$$

$$= \frac{1}{r^2}\frac{\partial}{\partial r}\left(-r^2\left[\frac{1}{r^2\sin\theta}\frac{\partial}{\partial\theta}\left(\sin\theta\frac{\partial\Phi}{\partial\theta}\right) + \frac{1}{r^2\sin^2\theta}\frac{\partial^2\Phi}{\partial\phi^2}\right]\right)$$

$$+ \frac{1}{r^2\sin\theta}\frac{\partial}{\partial\theta}\left(\sin\theta\frac{\partial^2\Phi}{\partial\theta\partial r}\right) + \frac{1}{r^2\sin^2\theta}\frac{\partial^3\Phi}{\partial\phi^2\partial r}$$

$$= -\frac{1}{r^2\sin\theta}\frac{\partial}{\partial\theta}\left(\sin\theta\frac{\partial^2\Phi}{\partial\theta\partial r}\right) - \frac{1}{r^2\sin^2\theta}\frac{\partial^3\Phi}{\partial\phi^2\partial r} + \frac{1}{r^2\sin\theta}\frac{\partial}{\partial\theta}\left(\sin\theta\frac{\partial^2\Phi}{\partial\theta\partial r}\right) + \frac{1}{r^2\sin^2\theta}\frac{\partial^3\Phi}{\partial\phi^2\partial r}$$

$$= 0.$$

Here, Ψ and Φ are toroidal and poloidal components, respectively. However, in our analysis, we did not use the radial velocity, u_{Pr}, and utilized only the horizontal velocity field on the surface of the Earth to obtain the toroidal-poloidal power, which is justified since to obtain the power of poloidal component, b_l^m, we calculate

$$b_l^m = \frac{r^2(2l+1)(l-m)!}{2\pi l(l+1)(l+m)!}\int_0^{2\pi}\int_0^{\pi}\boldsymbol{u}\cdot\mathbf{B_l^m}^*\sin\theta\,d\phi\,d\theta,$$

where

$$\mathbf{B_l^m} = \frac{1}{r}\left(0, B_{l\theta}^m, B_{l\phi}^m\right).$$

Hence, we do not need the radial velocity to calculate toroidal-poloidal power yet the calculation still meets the condition for the toroidal-poloidal decomposition.

Moreover, considering the summation of divergence in the whole vector field, the condition for the toroidal-poloidal decomposition is achieved when the net mass subducted into the Earth at subduction zone balances with that generated at ridge. It means that the expansion and the contraction of the Earth are almost ignorable. This is proven by a precise observation, such as satellite laser ranging (SLR), Very Long Baseline Interferometry (VLBI), Global Positioning System (GPS), and Doppler Orbitography and Radiopositioning Integrated by Satellite (DORIS), demonstrating that the mean radius of the Earth is not changing to within 1σ measurement uncertainty of 0.2 mm/yr (Wu et al., 2011). Therefore,

the expansion/contraction of the Earth is ignorable and the toroidal-poloidal decomposition is validate.

A.2   How we obtain toroidal-poloidal components

In polar coordinates, assuming $u_r = 0$, we obtain plate motion divided into toroidal and poloidal parts,

$$\boldsymbol{u} = \boldsymbol{u}_T + \boldsymbol{u}_P = \left(0, u_{T\theta}, u_{T\phi}\right) + \left(0, u_{P\theta}, u_{P\phi}\right) \tag{A.1}$$

where $u_{T\theta}, u_{p\phi}, u_{P\theta}$, and $u_{P\phi}$ are toroidal plate motions and poloidal plate motions in the theta and phi direction, respectively. With toroidal Component Ψ and poloidal component Φ, we can also describe plate motion as

$$\boldsymbol{u} = \boldsymbol{u}_T + \boldsymbol{u}_P = (\nabla \times \Psi) + (\nabla \times \nabla \times \Phi). \tag{A.2}$$

Our goal is to calculate the magnitude of vector fields of toroidal motion and poloidal motion. For the goal, we can expand both of them with harmonics, which shows the magnitude of each motion at a certain degree. Because we conduct the expansion on a sphere, we have to utilize spherical harmonics called Legendre polynomial, P_l^m where l and m are degree and order ($0 \le m \le l$), rather than Fourier series for the plane surface.

For instance, expanding a certain scalar function, $f(\theta, \phi)$, on a sphere provides

$$f(\theta, \phi) = \sum_l^\infty \sum_m^l P_l^m (\cos\theta) \left(c_{c,l}^{\ m} \cos m\phi + c_{s,l}^{\ m} \sin m\phi \right) \tag{A.3}$$

where $c_{s,l}$ and $c_{s,l}$ are the coefficients at degree l and order m. We can obtain the magnitude of the scalar function at a degree l, $\sigma(l)$, as

$$\sigma(l) = \left(c_{c,l}^{\ m} \right)^2 + \left(c_{s,l}^{\ m} \right)^2. \tag{A.4}$$

Therefore, calculating two coefficients $c_{s,l}$ and $c_{s,l}$ is our objective.

Nevertheless, the function which we deal with is plate motion on the sphere, that is, "vector fields". For this reason, spherical harmonic expansion of plate motion to calcu-

late its magnitude needs some techniques. Therefore, we carry out the following way as previous works did (e.g., Hager and O'Connell, 1978).

Regarding toroidal motion $\boldsymbol{u}_T$, from the definition:

$$\boldsymbol{u}_T = \left(0, \ \frac{1}{r\sin\theta}\frac{\partial\Psi}{\partial\phi}, \ -\frac{1}{r}\frac{\partial\Psi}{\partial\theta}\right), \tag{A.5}$$

setting $\Psi \equiv a\,f(\theta,\phi)$, where a and f are constant independent of θ and ϕ and scalar function, respectively, provides

$$\begin{aligned}
\boldsymbol{u}_T &= \left(0, \ \frac{a}{r\sin\theta}\frac{\partial f}{\partial\phi}, \ -\frac{a}{r}\frac{\partial f}{\partial\theta}\right) \\
&= a\left(0, \ \frac{1}{r\sin\theta}\frac{\partial f}{\partial\phi}, \ -\frac{1}{r}\frac{\partial f}{\partial\theta}\right).
\end{aligned}$$

When f is normalized, a decides the magnitude of toroidal motion. Consequently, in order to evaluate the magnitude of toroidal motion, we have to expand toroidal component Ψ like

$$\Psi = \sum_l^\infty \sum_m^l P_l^m(\cos\theta)\left(c_{c,l}^m\cos m\phi + c_{s,l}^m\sin m\phi\right) \tag{A.6}$$

and all we have to do is to calculate $\sigma(l)$.

With regard to poloidal motion $\boldsymbol{u}_P$, from the definition:

$$\begin{aligned}
\boldsymbol{u}_P &= \nabla\times\nabla\times(\Phi\mathbf{r}) \\
&= \nabla\times\left(0, \ \frac{1}{r\sin\theta}\frac{\partial\Phi}{\partial\phi}, \ -\frac{1}{r}\frac{\partial\Phi}{\partial\theta}\right) \\
&= \left(-\Delta_H\Phi = 0, \ -\frac{1}{r}\frac{\partial}{\partial r}\left(r\left[-\frac{1}{r}\frac{\partial\Phi}{\partial\theta}\right]\right), \ \frac{1}{r}\frac{\partial}{\partial r}\left(r\frac{1}{r\sin\theta}\frac{\partial\Phi}{\partial\phi}\right)\right) \\
&= \left(0, \ \frac{1}{r}\frac{\partial}{\partial\theta}\left(\frac{\partial\Phi}{\partial r}\right), \ \frac{1}{r\sin\theta}\frac{\partial}{\partial\phi}\left(\frac{\partial\Phi}{\partial r}\right)\right),
\end{aligned}$$

setting $\partial\Phi/\partial r \equiv b\,g(\theta,\phi)$, where b and g are constant independent of θ and ϕ and scalar function, respectively, offers

$$\begin{aligned}
\boldsymbol{u}_P &= \left(0, \ \frac{b}{r}\frac{\partial g}{\partial\theta}, \ \frac{b}{r\sin\theta}\frac{\partial g}{\partial\phi}\right) \\
&= b\left(0, \ \frac{1}{r}\frac{\partial g}{\partial\theta}, \ \frac{1}{r\sin\theta}\frac{\partial g}{\partial\phi}\right).
\end{aligned}$$

(Note that we are setting $\Psi \equiv af$ in toroidal motion and $\partial\Phi/\partial r \equiv bg$ in poloidal motion due to the difference in dimension). When g is normalized, b determines the magnitude of poloidal motion. As a result, for earning the magnitude of toroidal motion, we have to expand the partial derivative of poloidal component $\partial\Phi/\partial r$ as

$$\frac{\partial\Phi}{\partial r} = \sum_{l}^{\infty} \sum_{m}^{l} P_l^m (\cos\theta) \left(c_{c,l}^m \cos m\phi + c_{s,l}^m \sin m\phi \right). \tag{A.7}$$

In conclusion, we succeed in expansion of vector fields on the sphere, plate motion, both for toroidal component and poloidal component. We next express expanded forms of toroidal and poloidal motions with their expanded components.

A.3   Spherical harmonic expansion for toroidal term

Regarding toroidal motion $\boldsymbol{u}_T$, we conduct spherical harmonic expansion for it as follows. First of all, as we did in the last section, we expand toroidal component Ψ with spherical harmonics Y_l becomes

$$\Psi \equiv c_0 Y_0 \left(\theta, \phi\right) + c_1 Y_1 \left(\theta, \phi\right) + \cdots = \sum_{l=0}^{\infty} c_l Y_l(\theta, \phi) \tag{A.8}$$

where Y_l and c_l are spherical harmonics and the coefficient at degree l, respectively. Furthermore, we can write the spherical harmonics at degree l, Y_l, with Legendre polynomial $P_l^m(\cos\theta)$ as

$$c_l Y_l \left(\theta, \phi\right) = c_l^0 P_l^0(\cos\theta) + \sum_{m=1}^{l} c_{c,l}^m P_l^m(\cos\theta) \left(\cos m\phi\right) + \sum_{m=1}^{l} c_{s,l}^m P_l^m(\cos\theta) \left(\sin m\phi\right)$$

$$= \sum_{m=0}^{l} P_l^m(\cos\theta) \left(c_{c,l}^m \cos m\phi + c_{s,l}^m \sin m\phi \right). \tag{A.9}$$

Substituting the equation (A.9) into the equation (A.8) provides

$$\Psi = \sum_{l=0}^{\infty} \sum_{m=0}^{l} P_l^m(\cos\theta) \left(c_{c,l}^m \cos m\phi + c_{s,l}^m \sin m\phi \right). \tag{A.10}$$

As a result, toroidal motion:

$$\boldsymbol{u}_T = \nabla \times \Psi = \left(0, \frac{1}{r\sin\theta} \frac{\partial\Psi}{\partial\phi}, -\frac{1}{r} \frac{\partial\Psi}{\partial\theta} \right) \tag{A.11}$$

is

$$
\boldsymbol{u}_T = \sum_{l=0}^{\infty} \sum_{m=0}^{l} \frac{1}{r} \left(0, \frac{m}{\sin\theta} \, P_l^m(\cos\theta) \left(-c_{c,l}^{\,m} \sin m\phi + c_{s,l}^{\,m} \cos m\phi \right), \right.
$$
$$
\left. -\frac{\partial P_l^m(\cos\theta)}{\partial\theta} \left(c_{c,l}^{\,m} \cos m\phi + c_{s,l}^{\,m} \sin m\phi \right) \right).
$$

For complex expression, setting

$$
c_l^m \equiv c_{c,l}^{\,m} - i\, c_{s,l}^{\,m} \tag{A.12}
$$

$$
\mathbf{C_l^m} \equiv \frac{1}{r} \left(0, \frac{m}{\sin\theta} P_l^m(\cos\theta) \left(i \cos m\phi - \sin m\phi \right), -\frac{\partial P_l^m(\cos\theta)}{\partial\theta} \left(\cos m\phi + i \sin m\phi \right) \right) \tag{A.13}
$$

,where i is imaginary unit and c_l^m and $\mathbf{C_l^m}$ are the complex coefficient and the complex vector at degree l and order m, respectively, yields

$$
c_l^m \mathbf{C_l^m} = \frac{1}{r} \left(0, \frac{m}{\sin\theta} P_l^m(\cos\theta) \left(-c_{c,l}^{\,m} \sin m\phi + c_{s,l}^{\,m} \cos m\phi \right), \right.
$$
$$
\left. -\frac{\partial P_l^m(\cos\theta)}{\partial\theta} \left(c_{c,l}^{\,m} \cos m\phi + c_{s,l}^{\,m} \sin m\phi \right) \right)
$$
$$
+ i \, \mathrm{Im}\left\{ c_l^m \mathbf{C_l^m} \right\}.
$$

Consequently, using c_l^m and $\mathbf{C_l^m}$, we can describe complex expression of toroidal motion $\boldsymbol{u}_T$ as

$$
\boldsymbol{u}_T = \sum_{l=0}^{\infty} \sum_{m=0}^{l} \mathrm{Re}\left\{ c_l^m \mathbf{C_l^m} \right\}. \tag{A.14}
$$

Similarly, we will obtain poloidal motion in the next section.

A.4   Spherical harmonic expansion for poloidal term

Concerning poloidal motion, $\boldsymbol{u}_P$, we expand it with spherical harmonics Y_l and Legendre polynomial $P_l^m(\cos\theta)$. To begin with, we substitute expanding $\partial\Phi/\partial r$

$$
\frac{\partial\Phi}{\partial r} \equiv b_0 \, Y_0(\theta,\phi) + b_1 \, Y_1(\theta,\phi) + \cdots = \sum_{l=0}^{\infty} b_l \, Y_l(\theta,\phi)
$$
$$
= \sum_{l=0}^{\infty} \sum_{m=0}^{l} P_l^m(\cos\theta) \left(b_{c,l}^{\,m} \cos m\phi + b_{s,l}^{\,m} \sin m\phi \right)
$$

into the following equation of poloidal motion, $\boldsymbol{u}_P$,

$$\boldsymbol{u}_P = \nabla \times \nabla \times (\Phi \mathbf{r})$$

$$= \nabla \times \left(0, \frac{1}{r \sin\theta} \frac{\partial \Phi}{\partial \phi} - 0, 0 - \frac{1}{r} \frac{\partial \Phi}{\partial \theta} \right)$$

$$= \left(\frac{1}{r \sin\theta} \left[\frac{\partial}{\partial \theta} \left(-\frac{1}{r} \frac{\partial \Phi}{\partial \theta} \sin\theta \right) - \frac{\partial}{\partial \phi} \left(\frac{1}{r \sin\theta} \frac{\partial \Phi}{\partial \phi} \right) \right], \right.$$

$$\left. 0 - \frac{1}{r} \frac{\partial}{\partial r} \left[r \left(-\frac{1}{r} \frac{\partial \Phi}{\partial \theta} \right) \right], \frac{1}{r} \frac{\partial}{\partial r} \left[r \frac{1}{r \sin\theta} \frac{\partial \Phi}{\partial \phi} \right] - 0 \right)$$

$$= \left(-\Delta_H \Phi = 0, \frac{1}{r} \frac{\partial}{\partial r} \left(\frac{\partial \Phi}{\partial \theta} \right), \frac{1}{r \sin\theta} \frac{\partial}{\partial r} \left(\frac{\partial \Phi}{\partial \phi} \right) \right)$$

$$= \left(0, \frac{1}{r} \frac{\partial}{\partial \theta} \left(\frac{\partial \Phi}{\partial r} \right), \frac{1}{r \sin\theta} \frac{\partial}{\partial \phi} \left(\frac{\partial \Phi}{\partial r} \right) \right)$$

$$= \sum_{l=0}^{\infty} \sum_{m=0}^{l} \left(0, \frac{1}{r} \frac{\partial}{\partial \theta} \left[P_l^m(\cos\theta) \left(b_{c,l}^{\ m} \cos m\phi + b_{s,l}^{\ m} \sin m\phi \right) \right], \right.$$

$$\left. \frac{1}{r \sin\theta} \frac{\partial}{\partial \phi} \left[P_l^m(\cos\theta) \left(b_{c,l}^{\ m} \cos m\phi + b_{s,l}^{\ m} \sin m\phi \right) \right] \right)$$

$$= \sum_{l=0}^{\infty} \sum_{m=0}^{l} \left(0, \frac{1}{r} \left(\frac{\partial P_l^m(\cos\theta)}{\partial \theta} \right) \left(b_{c,l}^{\ m} \cos m\phi + b_{s,l}^{\ m} \sin m\phi \right), \right.$$

$$\left. \frac{m}{r \sin\theta} P_l^m(\cos\theta) \left(-b_{c,l}^{\ m} \sin m\phi + b_{s,l}^{\ m} \cos m\phi \right) \right)$$

where the Δ_H is horizontal Laplacian operator and we here assume that the radial velocity of plates is 0. Furthermore, setting

$$b_l^m = b_{c,l}^{\ m} - i b_{s,l}^{\ m}$$

$$\mathbf{B_l^m} = \frac{1}{r} \left(0, \left(\frac{\partial P_l^m(\cos\theta)}{\partial \theta} \right) (\cos m\phi + i \sin m\phi), \frac{m}{\sin\theta} P_l^m(\cos\theta) \left(i \cos m\phi - \sin m\phi \right) \right)$$

generates

$$\boldsymbol{u}_P = \sum_{l=0}^{\infty} \sum_{m=0}^{l} \frac{1}{r} \left(0, \left(\frac{\partial P_l^m(\cos\theta)}{\partial \theta} \right) \left(b_{c,l}^{\ m} \cos m\phi + b_{s,l}^{\ m} \sin m\phi \right), \right.$$

$$\left. \frac{m}{\sin\theta} P_l^m(\cos\theta) \left(-b_{c,l}^{\ m} \sin m\phi + b_{s,l}^{\ m} \cos m\phi \right) \right)$$

$$= \sum_{l=0}^{\infty} \sum_{m=0}^{l} \mathrm{Re} \left\{ b_l^m \mathbf{B_l^m} \right\}.$$

We are finally successful in spherical harmonic expansion for poloidal motion. In the next section, to obtain the toroidal coefficients of spherical harmonics, c_l^m, we will see an inte-

gral corresponding to Fourier transform in Fourier series expansion.

A.5   Calculation of the coefficient of toroidal motion

For the coefficients of toroidal motion, c_l^m, we calculate the following integral

$$\int_0^{2\pi} d\phi \int_0^{\pi} d\theta\, \boldsymbol{u} \cdot \mathbf{C_{l'}^{m'}}^* \sin\theta \tag{A.15}$$

where the superscript * represents the conjugate complex number and l' and m' are degree and order ($0 \le m' \le l'$). For the integral, we first consider the integrand, $\boldsymbol{u} \cdot \mathbf{C_{l'}^{m'}}^*$. As regards $\mathbf{C_{l'}^{m'}}^*$,

$$\mathbf{C_{l'}^{m'}}^* = \frac{1}{r}\left(0,\, \frac{m'}{\sin\theta} P_{l'}^{m'}(\cos\theta)\left(i\cos m'\phi - \sin m'\phi\right)^*,\, -\frac{\partial P_{l'}^{m'}(\cos\theta)}{\partial\theta}\left(\cos m'\phi + i\sin m'\phi\right)^*\right)$$

$$= \frac{1}{r}\left(0,\, \frac{m'}{\sin\theta} P_{l'}^{m'}(\cos\theta)\left(-i\cos m'\phi - \sin m'\phi\right),\, -\frac{\partial P_{l'}^{m'}(\cos\theta)}{\partial\theta}\left(\cos m'\phi - i\sin m'\phi\right)\right).$$

Substituting $\mathbf{C_{l'}^{m'}}^*$ into $\boldsymbol{u} \cdot \mathbf{C_{l'}^{m'}}^*$ gives (we omit $(\cos\theta)$ of $P_l^m(\cos\theta)$ for clarity)

$$\boldsymbol{u} \cdot \mathbf{C_{l'}^{m'}}^{*} \tag{A.16}$$

$$= (\boldsymbol{u}_T + \boldsymbol{u}_P) \cdot \mathbf{C_{l'}^{m'}}^{*}$$

$$= \sum_{l=0}^{\infty} \sum_{m=0}^{l} \mathrm{Re}\left\{ c_l^m \mathbf{C_l^m} + b_l^m \mathbf{B_l^m} \right\} \cdot \mathbf{C_{l'}^{m'}}^{*}$$

$$= \sum_{l=0}^{\infty} \sum_{m=0}^{l} \frac{1}{r^2}\Bigg\{ \Bigg(0,$$

$$\frac{m}{\sin\theta} P_l^m \left(-c_{c,l}^{\,m} \sin m\phi + c_{s,l}^{\,m} \cos m\phi \right) + \left(\frac{\partial P_l^m}{\partial\theta} \right) \left(b_{c,l}^{\,m} \cos m\phi + b_{s,l}^{\,m} \sin m\phi \right),$$

$$- \left(\frac{\partial P_l^m}{\partial\theta} \right) \left(c_{c,l}^{\,m} \cos m\phi + c_{s,l}^{\,m} \sin m\phi \right) + \frac{m}{\sin\theta} P_l^m \left(-b_{c,l}^{\,m} \sin m\phi + b_{s,l}^{\,m} \cos m\phi \right) \Bigg) \Bigg\}$$

$$\cdot \left(0, \frac{m'}{\sin\theta} P_{l'}^{m'} \left(-i \cos m'\phi - \sin m'\phi \right), -\left(\frac{\partial P_{l'}^{m'}}{\partial\theta} \right) \left(\cos m'\phi - i \sin m'\phi \right) \right)$$

$$= \sum_{l=0}^{\infty} \sum_{m=0}^{l} \frac{1}{r^2}\Bigg\{ \frac{mm'}{\sin^2\theta} P_l^m P_{l'}^{m'} \left(c_{s,l}^{\,m} \cos m\phi - c_{c,l}^{\,m} \sin m\phi \right) \left(-i \cos m'\phi - \sin m'\phi \right)$$

$$+ \left(\frac{\partial P_l^m}{\partial\theta} \right) \left(\frac{\partial P_{l'}^{m'}}{\partial\theta} \right) \left(c_{c,l}^{\,m} \cos m\phi + c_{s,l}^{\,m} \sin m\phi \right) \left(\cos m'\phi - i \sin m'\phi \right)$$

$$+ \frac{m'}{\sin\theta} \left(\frac{\partial P_l^m}{\partial\theta} \right) P_{l'}^{m'} \left(b_{c,l}^{\,m} \cos m\phi + b_{s,l}^{\,m} \sin m\phi \right) \left(-i \cos m'\phi - \sin m'\phi \right)$$

$$- \frac{m}{\sin\theta} P_l^m \left(\frac{\partial P_{l'}^{m'}}{\partial\theta} \right) \left(b_{s,l}^{\,m} \cos m\phi - b_{c,l}^{\,m} \sin m\phi \right) \left(\cos m'\phi - i \sin m'\phi \right) \Bigg\}. \tag{A.17}$$

To obtain the coefficients, c_l^m, we integral the equation (A.17), i.e., calculate the equation (A.15). Concerning the integration, we will show two facts: (i) when $m \neq m'$, $\int_0^{2\pi} \boldsymbol{u} \cdot \mathbf{C_{l'}^{m'}}^{*} d\phi$ becomes zero and (ii) operating $\int_0^{\pi} \sin\theta\, d\theta$ on the equation (A.17) vanishes the terms of $\left(\partial P_l^m / \partial\theta \right) P_l^m$

(i) when $m \neq m'$, $\int_0^{2\pi} \boldsymbol{u} \cdot \mathbf{C_{l'}^{m'}}^{*} d\phi$ becomes zero

We are demonstrating that for $m \neq m'$, $\int_0^{2\pi} \boldsymbol{u} \cdot \mathbf{C_{l'}^{m'}}^{*} d\phi$ becomes zero. First, we integral the products of sin and cos in the equation (A.17)

$$\int_0^{2\pi} \cos m\phi \sin m'\phi\, d\phi = \frac{1}{2} \int_0^{2\pi} \left(\sin\left(m' + m \right)\phi + \sin\left(m' - m \right)\phi \right) d\phi$$

$$= \begin{cases} \frac{1}{2} \left[\frac{-1}{m'+m} \cos\left(m' + m \right)\phi + \frac{-1}{m'-m} \cos\left(m' - m \right)\phi \right]_0^{2\pi} = 0 & (m \neq m') \\ \frac{1}{2} \left[\frac{-1}{m'+m} \cos\left(m' + m \right)\phi \right]_0^{2\pi} = 0 & (m = m'). \end{cases}$$

This means that all the terms containing the products of *sin* and *cos* always become zero.

Similarly, the integrals of products of *cos* and *cos* and those of *sin* and *sin* are

$$\int_0^{2\pi} \cos m\phi \cos m'\phi \, d\phi = \frac{1}{2} \int_0^{2\pi} \left(\cos\left(m' - m\right)\phi + \cos\left(m' + m\right)\phi \right) d\phi$$

$$= \begin{cases} \frac{1}{2} \left[\frac{1}{m'-m} \sin\left(m' - m\right)\phi + \frac{1}{m'+m} \sin\left(m' + m\right)\phi \right]_0^{2\pi} = 0 & (m \neq m') \\ \frac{1}{2} \left[\phi + \frac{1}{m'+m} \sin\left(m' + m\right)\phi \right]_0^{2\pi} = \pi & (m = m') \end{cases}$$

$$\int_0^{2\pi} \sin m\phi \sin m'\phi \, d\phi = \frac{1}{2} \int_0^{2\pi} \left(\cos\left(m' - m\right)\phi - \cos\left(m' + m\right)\phi \right) d\phi$$

$$= \begin{cases} \frac{1}{2} \left[\frac{1}{m'-m} \sin\left(m' - m\right)\phi - \frac{1}{m'+m} \sin\left(m' + m\right)\phi \right]_0^{2\pi} = 0 & (m \neq m') \\ \frac{1}{2} \left[\phi - \frac{1}{m'+m} \sin\left(m' + m\right)\phi \right]_0^{2\pi} = \pi & (m = m'). \end{cases}$$

In summary, for $m \neq m'$, all the terms become zero and for $m = m'$, only the terms including $\cos^2 m\phi$ or $\sin^2 m\phi$ becomes π though the others become zero.

Now the result of integration of the equation (A.17) becomes

$$\int_0^{2\pi} d\phi \int_0^{\pi} d\theta \, \boldsymbol{u} \cdot \mathbf{C}_{\mathbf{l'}}^{\mathbf{m'}\,*} \sin\theta$$

$$= \sum_{l=0}^{\infty} \int_0^{\pi} \frac{\pi}{r^2} \left\{ \frac{m^2}{\sin^2\theta} P_l^m P_{l'}^m \left(-i c_{s,l}^m + c_{c,l}^m \right) + \left(\frac{\partial P_l^m}{\partial\theta} \right)\left(\frac{\partial P_{l'}^m}{\partial\theta} \right)\left(c_{c,l}^m - i c_{s,l}^m \right) \right.$$

$$\left. + \frac{m}{\sin\theta}\left(\frac{\partial P_l^m}{\partial\theta} \right) P_{l'}^m \left(-i b_{c,l}^m - b_{s,l}^m \right) - \frac{m}{\sin\theta} P_l^m \left(\frac{\partial P_{l'}^m}{\partial\theta} \right)\left(b_{s,l}^m + i b_{c,l}^m \right) \right\} \sin\theta \, d\theta.$$

(A.18)

(ii) operating $\int_0^{\pi} \sin\theta \, d\theta$ on the equation (A.17) vanishes the terms of $\left(\partial P_l^m / \partial\theta \right) P_l^m$

We, next, prove the fact that operating $\int_0^{\pi} \sin\theta \, d\theta$ on the equation (A.17) vanishes the terms of $\left(\partial P_l^m / \partial\theta \right) P_l^m$. To begin with, using the integration by parts yields

$$\int_0^{\pi} \frac{1}{\sin\theta}\left(\frac{\partial P_l^m}{\partial\theta} \right) P_{l'}^m \sin\theta \, d\theta = \int_0^{\pi} \left(\frac{\partial P_l^m}{\partial\theta} \right) P_{l'}^m \, d\theta = \left[P_l^m P_{l'}^m \right]_0^{\pi} - \int_0^{\pi} P_l^m \left(\frac{\partial P_{l'}^m}{\partial\theta} \right) d\theta$$

$$= 0 - \int_0^{\pi} P_l^m \left(\frac{\partial P_{l'}^m}{\partial\theta} \right) d\theta \qquad (\text{for } m \neq 0)$$

where $\left[P_l^m P_{l'}^m \right]_0^\pi$ vanishes because Legendre polynomial contains $(\sin m\theta)$. This calculation means for $m \neq 0$

$$\int_0^\pi \left(\left(\frac{\partial P_l^m}{\partial \theta} \right) P_{l'}^m + P_l^m \left(\frac{\partial P_{l'}^m}{\partial \theta} \right) \right) d\theta = 0. \tag{A.19}$$

At $m = 0$, in addition, the terms about $P_l^m \partial P_l^m / \partial \theta$ in (A.18) becomes zero because the terms contain m. Considering the result, (A.18) finally becomes

$$\int_0^\pi \int_0^{2\pi} \boldsymbol{u} \cdot \mathbf{C_{l'}^{m'}}^* \sin\theta \, d\phi d\theta$$

$$= \sum_{l=0}^\infty \int_0^\pi \frac{\pi}{r^2} \left\{ \frac{m^2}{\sin^2\theta} P_l^m P_{l'}^m \left(c_{c,l}^m - i c_{s,l}^m \right) + \left(\frac{\partial P_l^m}{\partial \theta} \right) \left(\frac{\partial P_{l'}^m}{\partial \theta} \right) \left(c_{c,l}^m - i c_{s,l}^m \right) + 0 \right\} \sin\theta \, d\phi d\theta$$

$$= \sum_{l=0}^\infty \frac{\pi}{r^2} \int_0^\pi \left[\frac{m^2}{\sin\theta} P_l^m P_{l'}^m + \sin\theta \left(\frac{\partial P_l^m}{\partial \theta} \right) \left(\frac{\partial P_{l'}^m}{\partial \theta} \right) \right] \left(c_{c,l}^m - i c_{s,l}^m \right) d\theta$$

$$= \frac{\pi}{r^2} c_l^m \frac{2(l+m)! \, l(l+1)}{(l-m)!(2l+1)} \tag{A.20}$$

where we use a formula of Legendre polynomial:

$$\int_0^\pi \left[\frac{m^2}{\sin\theta} P_n^m(\cos\theta) P_l^m(\cos\theta) + \sin\theta \frac{dP_n^m(\cos\theta)}{d\theta} \frac{dP_l^m(\cos\theta)}{d\theta} \right] d\theta = \begin{cases} 0 & [n \neq l] \\ \frac{2l(l+1)(l+m)!}{(2l+1)(l-m)!} & [n = l] \end{cases}. \tag{A.21}$$

In conclusion, we acquire

$$\int_0^\pi \int_0^{2\pi} \boldsymbol{u} \cdot \mathbf{C_{l'}^{m'}}^* \sin\theta \, d\phi d\theta = \frac{2\pi}{r^2} \frac{(l+m)! \, l(l+1)}{(l-m)!(2l+1)} c_l^m. \tag{A.22}$$

Similarly, we calculate $\int_0^{2\pi} d\phi \int_0^\pi d\theta \, \boldsymbol{u} \cdot \mathbf{B_l^m}^* \sin\theta$ for the poloidal coefficient b_l^m.

A.6   Calculation of the coefficient of poloidal motion

For the coefficients of poloidal motion, b_l^m, we calculate the following integral

$$\int_0^{2\pi} d\phi \int_0^\pi d\theta \, \boldsymbol{u} \cdot \mathbf{B_{l'}^{m'}}^* \sin\theta. \tag{A.23}$$

First of all, $\mathbf{B_{l'}^{m'}}^*$ is

$$\mathbf{B_{l'}^{m'}}^{*} = \frac{1}{r}\left(0,\left(\frac{\partial P_{l'}^{m'}(\cos\theta)}{\partial\theta}\right)(\cos m'\phi + i\sin m'\phi)^{*},\frac{m'}{\sin\theta}P_{l'}^{m'}(\cos\theta)\left(i\cos m'\phi - \sin m'\phi\right)^{*}\right)$$

$$= \frac{1}{r}\left(0,\left(\frac{\partial P_{l'}^{m'}(\cos\theta)}{\partial\theta}\right)(\cos m'\phi - i\sin m'\phi),\frac{m'}{\sin\theta}P_{l'}^{m'}(\cos\theta)\left(-i\cos m'\phi - \sin m'\phi\right)\right).$$

Substituting $\mathbf{B_{l'}^{m'}}^{*}$ into $\boldsymbol{u}\cdot\mathbf{B_{l'}^{m'}}^{*}$ generates (we omit $(\cos\theta)$ of $P_l^m(\cos\theta)$ for clarity)

$$\boldsymbol{u}\cdot\mathbf{B_{l'}^{m'}}^{*} = (\boldsymbol{u}_T + \boldsymbol{u}_P)\cdot\mathbf{B_{l'}^{m'}}^{*}$$

$$= \sum_{l=0}^{\infty}\sum_{m=0}^{l}\operatorname{Re}\left\{c_l^m\mathbf{C_l^m} + b_l^m\mathbf{B_l^m}\right\}\cdot\mathbf{B_{l'}^{m'}}^{*}$$

$$= \sum_{l=0}^{\infty}\sum_{m=0}^{l}\frac{1}{r^2}\left\{\frac{m}{\sin\theta}P_l^m\left(\frac{\partial P_{l'}^{m'}}{\partial\theta}\right)\left(c_{s,l}^m\cos m\phi - c_{c,l}^m\sin m\phi\right)(\cos m'\phi - i\sin m'\phi)\right.$$

$$- \frac{m'}{\sin\theta}\left(\frac{\partial P_l^m}{\partial\theta}\right)P_{l'}^{m'}\left(c_{c,l}^m\cos m\phi + c_{s,l}^m\sin m\phi\right)(-i\cos m'\phi - \sin m'\phi)$$

$$+ \left(\frac{\partial P_l^m}{\partial\theta}\right)\left(\frac{\partial P_{l'}^{m'}}{\partial\theta}\right)\left(b_{c,l}^m\cos m\phi + b_{s,l}^m\sin m\phi\right)(\cos m'\phi - i\sin m'\phi)$$

$$\left. + \frac{mm'}{\sin^2\theta}P_l^m P_{l'}^{m'}\left(b_{s,l}^m\cos m\phi - b_{c,l}^m\sin m\phi\right)(-i\cos m'\phi - \sin m'\phi)\right\}.$$

As we showed in the last section, when $m \neq m'$, all the terms become 0 and for $m = m'$, operating $\int_0^{2\pi}d\phi$ vanishes the terms with $\sin\times\cos$ and yields π from the terms with $\sin^2$ or $\cos^2$. Therefore, integration of (A.23) offers

$$\int_0^{\pi}\int_0^{2\pi}\boldsymbol{u}\cdot\mathbf{B_{l'}^{m'}}^{*}\sin\theta\,d\phi\,d\theta = \sum_{l=0}^{\infty}\frac{\pi}{r^2}\int_0^{\pi}\left[\frac{m}{\sin\theta}P_l^m\left(\frac{\partial P_{l'}^m}{\partial\theta}\right) + \frac{m}{\sin\theta}\left(\frac{\partial P_l^m}{\partial\theta}\right)P_{l'}^m\right]\left(c_{c,l}^m + ic_{s,l}^m\right)$$

$$+ \left[\left(\frac{\partial P_l^m}{\partial\theta}\right)\left(\frac{\partial P_{l'}^m}{\partial\theta}\right) + \frac{m^2}{\sin^2\theta}P_l^m P_{l'}^m\right]\left(b_{c,l}^m - ib_{s,l}^m\right)\sin\theta\,d\theta$$

$$= \sum_{l=0}^{\infty}\frac{m\pi}{r^2}\int_0^{\pi}\left[P_l^m\left(\frac{\partial P_{l'}^m}{\partial\theta}\right) + \left(\frac{\partial P_l^m}{\partial\theta}\right)P_{l'}^m\right]d\theta\left(c_{c,l}^m + ic_{s,l}^m\right)$$

$$+ \sum_{l=0}^{\infty}\frac{\pi}{r^2}b_l^m\int_0^{\pi}\left[\sin\theta\left(\frac{\partial P_l^m}{\partial\theta}\right)\left(\frac{\partial P_{l'}^m}{\partial\theta}\right) + \frac{m^2}{\sin\theta}P_l^m P_{l'}^m\right]\frac{d}{d\theta}d\theta$$

$$= 0 + \frac{\pi}{r^2}b_l^m\frac{2(l+m)!\,l(l+1)}{(l-m)!(2l+1)}$$

$$= \frac{\pi}{r^2}b_l^m\frac{2(l+m)!\,l(l+1)}{(l-m)!(2l+1)}$$

where we use the equations (A.19) and (A.21). In conclusion, we obtain

$$\int_0^{2\pi} \int_0^{\pi} \boldsymbol{u} \cdot \mathbf{B}_{\mathbf{l}'}^{\mathbf{m}'\,*} \sin\theta\, d\phi\, d\theta = \frac{2\pi}{r^2} \frac{(l+m)!}{(l-m)!} \frac{l(l+1)}{(2l+1)} b_l^m. \tag{A.24}$$

A.7   Calculation of power of toroidal motion and poloidal motion

From the equation (A.22) and (A.24), we acquire the coefficient of toroidal motion, c_l^m, and the coefficients of poloidal motion, b_l^m,

$$c_l^m = \frac{r^2(2l+1)(l-m)!}{2\pi l(l+1)(l+m)!} \int_0^{2\pi} \int_0^{\pi} \boldsymbol{u} \cdot \mathbf{C}_{\mathbf{l}}^{\mathbf{m}\,*} \sin\theta\, d\phi\, d\theta \tag{A.25}$$

$$b_l^m = \frac{r^2(2l+1)(l-m)!}{2\pi l(l+1)(l+m)!} \int_0^{2\pi} \int_0^{\pi} \boldsymbol{u} \cdot \mathbf{B}_{\mathbf{l}}^{\mathbf{m}\,*} \sin\theta\, d\phi\, d\theta. \tag{A.26}$$

We, thus, obtain the degree power spectra of toroidal and poloidal motion, $\sigma_T(l)$ and $\sigma_P(l)$,

$$\sigma_T^2(l) = \sum_{m=0}^{l} c_l^m c_l^{m*} = \sum_{m=0}^{l} \left\{ \left(c_{c,l}^m\right)^2 + \left(c_{s,l}^m\right)^2 \right\} \tag{A.27}$$

$$\sigma_P^2(l) = \sum_{m=0}^{l} b_l^m b_l^{m*} = \sum_{m=0}^{l} \left\{ \left(b_{c,l}^m\right)^2 + \left(b_{s,l}^m\right)^2 \right\}. \tag{A.28}$$

We calculate those coefficients numerically in the next section.

Appendix B

Numerical calculation of spherical harmonic expansion

B.1 Calculation of toroidal-poloidal power

To obtain the degree power spectra $\sigma_T(l)$ and $\sigma_P(l)$, we need the following coefficients c_l^m and b_l^m

$$\sigma_T^2(l) = \sum_{m=0}^{l} c_l^m c_l^{m*} = \sum_{m=0}^{l} \left\{ \left(c_{c,l}^m \right)^2 + \left(c_{s,l}^m \right)^2 \right\} \tag{B.1}$$

$$\sigma_P^2(l) = \sum_{m=0}^{l} b_l^m b_l^{m*} = \sum_{m=0}^{l} \left\{ \left(b_{c,l}^m \right)^2 + \left(b_{s,l}^m \right)^2 \right\}. \tag{B.2}$$

From the equations (A.25) and (A.26) in the last section, we can calculate them like

$$c_l^m = \frac{r^2}{2\pi} \frac{(l-m)!\,(2l+1)}{(l+m)!\,l\,(l+1)} \int_0^{2\pi} \int_0^{\pi} \boldsymbol{u} \cdot \left(\mathbf{C_l^m} \right)^* \sin\theta\, d\phi\, d\theta \tag{B.3}$$

$$b_l^m = \frac{r^2}{2\pi} \frac{(l-m)!\,(2l+1)}{(l+m)!\,l\,(l+1)} \int_0^{2\pi} \int_0^{\pi} \boldsymbol{u} \cdot \left(\mathbf{B_l^m} \right)^* \sin\theta\, d\phi\, d\theta \tag{B.4}$$

(this is the correspondence in Spherical harmonic expansion to the Fourier transform in Fourier series expansion). Furthermore, normalizing Legendre polynomials in $\mathbf{C_l^m}$ and $\mathbf{B_l^m}$ yields

$$c_l^m = \frac{r^2}{\pi l(l+1)} \int_0^{2\pi} \int_0^\pi \boldsymbol{u} \cdot \left(\tilde{\mathbf{C}}_\mathbf{l}^\mathbf{m}\right)^* \sin\theta \, d\phi \, d\theta \tag{B.5}$$

$$b_l^m = \frac{r^2}{\pi l(l+1)} \int_0^{2\pi} \int_0^\pi \boldsymbol{u} \cdot \left(\tilde{\mathbf{B}}_\mathbf{l}^\mathbf{m}\right)^* \sin\theta \, d\phi \, d\theta. \tag{B.6}$$

where $\tilde{\mathbf{C}}_\mathbf{l}^\mathbf{m}$ and $\tilde{\mathbf{B}}_\mathbf{l}^\mathbf{m}$ are normalized and the normalization of Legendre polynomial is

$$P_l^m(\cos\theta) \xrightarrow{normalization} \sqrt{\frac{(2l+1)(l-m)!}{2(l+m)!}} \tilde{P}_l^m(\cos\theta) \tag{B.7}$$

because

$$\int_{-1}^1 P_n^m(x) P_l^m(x) \, dx = \begin{cases} 0 & [n \neq l] \\ \frac{2(l+m)!}{(2l+1)(l-m)!} & [n = l] \end{cases} \tag{B.8}$$

where ˜ represent normalized functions. For clear expression, however, we omit ˜ of normalized $\tilde{\mathbf{C}}_\mathbf{l}^\mathbf{m}$, $\tilde{\mathbf{B}}_\mathbf{l}^\mathbf{m}$, and $\tilde{P}_l^m$ in the following calculation. Our numerical calculation utilizes summation as integral of the equation (B.3) and (B.4)

$$c_l^m = \frac{r^2}{\pi l(l+1)} \sum_{j=0}^{1801} \sum_{i=0}^{3600} \boldsymbol{u}\left(\phi(i), \theta(j)\right) \cdot \left(\mathbf{C}_\mathbf{l}^\mathbf{m}\right)^* \sin\theta(j) \, d\phi \, d\theta \tag{B.9}$$

$$b_l^m = \frac{r^2}{\pi l(l+1)} \sum_{j=0}^{1801} \sum_{i=0}^{3600} \boldsymbol{u}\left(\phi(i), \theta(j)\right) \cdot \left(\mathbf{B}_\mathbf{l}^\mathbf{m}\right)^* \sin\theta(j) \, d\phi \, d\theta \tag{B.10}$$

where the resolution of plate motion is $d\phi = d\theta = 0.1°$. We next show more concrete form of the integrands, $\boldsymbol{u} \cdot \left(\mathbf{C}_\mathbf{l}^\mathbf{m}\right)^*$ and $\boldsymbol{u} \cdot \left(\mathbf{B}_\mathbf{l}^\mathbf{m}\right)^*$.

B.2 Calculation of integrant

With regard to the integrand about toroidal motion, $\boldsymbol{u} \cdot \mathbf{C}_\mathbf{l}^{\mathbf{m}*}$, substituting

$$\mathbf{C}_\mathbf{l}^{\mathbf{m}*} = \frac{1}{r}\left(0, \frac{m}{\sin\theta} P_l^m(\cos\theta)\left(i\cos m\phi - \sin m\phi\right)^*, -\frac{\partial P_l^m(\cos\theta)}{\partial\theta}\left(\cos m\phi + i\sin m\phi\right)^*\right)$$

$$= \frac{1}{r}\left(0, \frac{m}{\sin\theta} P_l^m(\cos\theta)\left(-i\cos m\phi - \sin m\phi\right), -\frac{\partial P_l^m(\cos\theta)}{\partial\theta}\left(\cos m\phi - i\sin m\phi\right)\right)$$

into $\boldsymbol{u} \cdot \mathbf{C}_\mathbf{l}^{\mathbf{m}*}$ provides

$\boldsymbol{u} \cdot \mathbf{C_l^{m\,*}}$

$$= \left(0,\, u_\theta,\, u_\phi\right) \cdot \frac{1}{r} \left(0,\, \frac{m}{\sin\theta} P_l^m(\cos\theta)\left(-i\cos m\phi - \sin m\phi\right),\, -\left(\frac{\partial P_l^m(\cos\theta)}{\partial\theta}\right)\left(\cos m\phi - i\sin m\phi\right)\right)$$

$$= \frac{1}{r}\left[u_\theta \frac{m}{\sin\theta} P_l^m(\cos\theta)\left(-i\cos m\phi - \sin m\phi\right) - u_\phi\left(\frac{\partial P_l^m(\cos\theta)}{\partial\theta}\right)\left(\cos m\phi - i\sin m\phi\right)\right].$$

$$(\text{B.11})$$

Similarly, the integrand about poloidal motion, $\boldsymbol{u} \cdot \mathbf{B_l^{m\,*}}$, becomes

$$\boldsymbol{u} \cdot \mathbf{B_l^{m\,*}} = \frac{1}{r}\left[u_\theta\left(\frac{\partial P_l^m(\cos\theta)}{\partial\theta}\right)\left(\cos m\phi - i\sin m\phi\right) + u_\phi \frac{m}{\sin\theta} P_l^m(\cos\theta)\left(-i\cos m\phi - \sin m\phi\right)\right].$$

$$(\text{B.12})$$

For the integrands above (B.11) and (B.12), we are showing the calculation of Legendre polynomials P_l^m and the derivative $\partial P_l^m / \partial\theta$, particularly for numerical calculation.

B.3   Calculation of Legendre polynomial functions and the derivative

To reduce the calculation time, for almost all the Legendre polynomials we do not use the definition of Legendre polynomials

$$P_l^m(\cos\theta) = \sin^m\theta\left(\frac{dP_l(\cos\theta)}{d\cos\theta}\right) \tag{B.13}$$

where the P_l is Legendre function

$$P_l(\cos\theta) = \sum_{s=0}^{\leq l/2} (-1)^s \frac{(2l-2s)!}{2^l s!(l-s)!(l-2s)!} \cos^{l-2s}\theta, \tag{B.14}$$

since the calculation takes long time due to the summation and factorials at high degree. Instead, we utilize **recursive formulae** of Legendre polynomials. Calculation without summation provides us with some merits, such as not only reducing the calculation time but also avoiding numerical errors, like loss of trailing digit. Before starting the calculation of recursive formula, we raise two important points for numerical calculation: the order of normalization and the parity of Legendre polynomials.

B.3.1　Normalization of Legendre polynomials and the derivatives

Normalizing both Legendre polynomials and the derivatives, we have to be cautious about the order of normalization in our program. If we normalize Legendre polynomials before calculating the derivative, calculated derivatives become wrong since the derivatives are decided by various degree Legendre polynomials due to the recursive formulae. Therefore, we first obtain all the Legendre polynomials and the derivatives and after the calculation normalize all of them together. In detail, normalization means the result of the integral:

$$\int_{-1}^{1} P_l^m(x) P_l^m(x) dx = \frac{2(l+m)!}{(2l+1)(l-m)!} \tag{B.15}$$

becomes 1 and, therefore,

$$P_l^m(\cos\theta) \longrightarrow \sqrt{\frac{(2l+1)(l-m)!}{2(l+m)!}} P_l^m(\cos\theta) \tag{B.16}$$

$$\frac{dP_l^m(\cos\theta)}{d\theta} \longrightarrow \frac{d\sqrt{\frac{(2l+1)(l-m)!}{2(l+m)!}} P_l^m(\cos\theta)}{d\theta} = \sqrt{\frac{(2l+1)(l-m)!}{2(l+m)!}} \frac{dP_l^m(\cos\theta)}{d\theta} \tag{B.17}$$

where the arrows $\longrightarrow$ represents normalization.

B.3.2　Parity of Legendre polynomials

In addition, to shorten the calculation time more, we focus on the parity of Legendre polynomials, that is,

$$P_l^m(\cos(\pi-\theta)) = P_l^m(-\cos\theta) = (-1)^{l+m} P_l^m(\cos\theta) \tag{B.18}$$

$$\frac{dP_l^m(\cos\theta)}{d\theta} \xrightarrow{\theta=\pi-\theta} \frac{dP_l^m(\cos(\pi-\theta))}{d(\pi-\theta)} = \frac{1}{\frac{d(\pi-\theta)}{d\theta}} \frac{dP_l^m(\cos(\pi-\theta))}{d\theta}$$

$$= (-1) \frac{d(-1)^{l+m} P_l^m(\cos\theta)}{d\theta}$$

$$= (-1)^{l+m+1} \frac{dP_l^m(\cos\theta)}{d\theta}. \tag{B.19}$$

It means that calculation for the Northern Hemisphere ($0 \le \theta \le \pi/2$) can be used to ones of the Southern Hemisphere ($\pi/2 \le \theta \le \pi$), which reduces the calculation time to about half.

Now, keeping in mind the two points: the order of normalization and the parity, we can begin to calculate recursive formulae. For the calculation, we classify it into two cases: (a) $\theta \neq 0, \pi$ and (b) $\theta = 0, \pi$ since the recursive formulae include $1/\sin\theta$ and cannot be used in the case of (b).

(a) Legendre polynomials and its derivatives for $\theta \neq 0, \pi$

Here we consider the case of (a) $\theta \neq 0 \, \text{or} \, \pi$. For starting the calculation of recursive formula, we need initial Legendre polynomials at degree $l = 0, 1, 2$.

At degree l=0,1,2, Legendre polynomials and its derivatives are

$$\text{(at l=0)} \quad P_0^0(\cos\theta) = 1 \longrightarrow \frac{1}{\sqrt{2}}$$

$$\frac{dP_0^0(\cos\theta)}{d\theta} = 0 \longrightarrow 0$$

$$\text{(at l=1)} \quad P_1^0(\cos\theta) = \cos\theta \longrightarrow \sqrt{\frac{3}{2}}\cos\theta$$

$$\frac{dP_1^0(\cos\theta)}{d\theta} = -\sin\theta \longrightarrow -\sqrt{\frac{3}{2}}\sin\theta$$

$$P_1^1(\cos\theta) = \sin\theta \longrightarrow \sqrt{\frac{3}{4}}\sin\theta$$

$$\frac{dP_1^1(\cos\theta)}{d\theta} = \cos\theta \longrightarrow \sqrt{\frac{3}{4}}\cos\theta$$

$$\text{(at l=2)} \quad P_2^0(\cos\theta) = \frac{1}{2}\left(3\cos^2\theta - 1\right) \longrightarrow \frac{1}{2}\sqrt{\frac{5}{2}}\left(3\cos^2\theta - 1\right)$$

$$\frac{dP_2^0(\cos\theta)}{d\theta} = -3\cos\theta\sin\theta \longrightarrow -\sqrt{\frac{5}{2}}3\cos\theta\sin\theta$$

$$P_2^1(\cos\theta) = 3\sin\theta\cos\theta \longrightarrow \sqrt{\frac{5}{12}}3\sin\theta\cos\theta$$

$$\frac{dP_2^1(\cos\theta)}{d\theta} = 3\cos2\theta \longrightarrow \sqrt{\frac{5}{12}}3\cos2\theta$$

$$P_2^2(\cos\theta) = 3\sin^2\theta \longrightarrow \sqrt{\frac{5}{48}}3\sin^2\theta$$

$$\frac{dP_2^2(\cos\theta)}{d\theta} = 3\sin2\theta \longrightarrow \sqrt{\frac{5}{48}}3\sin2\theta$$

where the arrows $\longrightarrow$ represent normalization and the normalized results are written un-

naturally to clarify the effect of normalization. Now, with those initial values, we make use of recursive formulae for $l > 2$.

At a certain degree l, we calculate P_l^m and $dP_l^m/d\theta$ for $m = 0, 1, \cdots, l$. At $m = l$, from formulae of Legendre polynomials, we can obtain

$$P_l^l(\cos\theta) = (2l-1)!! \sin^l\theta \tag{B.20}$$

$$\frac{dP_l^l(\cos\theta)}{d\theta} = (2l-1)!! \, l \cos\theta \sin^{l-1}\theta$$

$$= l\frac{\cos\theta}{\sin\theta} P_l^l(\cos\theta) \tag{B.21}$$

where

$$(2l-1)!! = (2l-1)(2l-3)(2l-5)\cdots 3 \cdot 1.$$

For $m = l-1$, i.e., P_l^{l-1}, using the equation (B.20) and this recursive formula

$$(l-m)\cos\theta P_l^m - (l+m)P_{l-1}^m + \sin\theta P_l^{m+1} = 0 \tag{B.22}$$

at $m = l-1$ yields

$$(l-(l-1))\cos\theta P_l^{l-1} - (l+(l-1))P_{l-1}^{l-1} + \sin\theta P_l^l = 0$$

$$\Leftrightarrow \quad \cos\theta P_l^{l-1} - (2l-1)P_{l-1}^{l-1} + \sin\theta P_l^l = 0$$

$$\Leftrightarrow \quad \cos\theta P_l^{l-1} = (2l-1)\left[(2(l-1)-1)!! \sin^{l-1}\theta\right] - \sin\theta\left[(2l-1)!! \sin^l\theta\right] \quad \text{(from (B.20))}$$

$$= (2l-1)(2l-3)!! \sin^{l-1}\theta - \sin\theta\left[(2l-1)!! \sin^l\theta\right]$$

$$= (2l-1)!! \frac{\sin^l\theta}{\sin\theta} - \sin\theta\left[(2l-1)!! \sin^l\theta\right]$$

$$= \left(\frac{1}{\sin\theta} - \sin\theta\right)(2l-1)!! \sin^l\theta$$

$$= \frac{\cos^2\theta}{\sin\theta} P_l^l.$$

Therefore, Legendre polynomial P_l^{l-1} is

$$P_l^{l-1}(\cos\theta) = \frac{\cos\theta}{\sin\theta} P_l^l(\cos\theta) \tag{B.23}$$

where although we do not consider the case of $\cos\theta = 0$ this numerical calculation provides reasonable results at $\theta = \pi/2$. With P_l^l and P_l^{l-1}, we calculate P_l^m $(m = 0, 1, \cdots, l-2)$

recursively. This recursive formula

$$P_l^{m+2} - 2(m+1)\frac{\cos\theta}{\sin\theta}P_l^{m+1} + (l-m)(l+m+1)P_l^m = 0 \qquad \text{(B.24)}$$

offers P_l^m for $m = l-2, l-1, \ldots, 1, 0$:

$$P_l^m(\cos\theta) = \frac{1}{(l-m)(l+m+1)}\left[2(m+1)\frac{\cos\theta}{\sin\theta}P_l^{m+1}(\cos\theta) - P_l^{m+2}(\cos\theta)\right]. \qquad \text{(B.25)}$$

Moreover, using the definition of Legendre polynomials:

$$P_l^m(\cos\theta) = \sin^m\theta\left(\frac{d^m P_l(\cos\theta)}{d\cos\theta^m}\right), \qquad \text{(B.26)}$$

we also acquire the derivatives $dP_l^m/d\theta$ for $m = l-1, l-2, \cdots, 0$ recursively like

$$
\begin{aligned}
\frac{dP_l^m(\cos\theta)}{d\theta} &= \frac{d}{d\theta}\left(\sin^m\theta\left(\frac{d^m P_l(\cos\theta)}{d\cos\theta^m}\right)\right) \\
&= m\cos\theta\sin^{m-1}\theta\left(\frac{d^m P_l(\cos\theta)}{d\cos\theta^m}\right) + \sin^m\theta\frac{d\cos\theta}{d\theta}\left(\frac{d^{m+1}P_l(\cos\theta)}{d\cos\theta^{m+1}}\right) \\
&= m\frac{\cos\theta}{\sin\theta}\sin^m\theta\left(\frac{d^m P_l(\cos\theta)}{d\cos\theta^m}\right) - \sin^{m+1}\theta\left(\frac{d^{m+1}P_l(\cos\theta)}{d\cos\theta^{m+1}}\right) \\
&= m\frac{\cos\theta}{\sin\theta}P_l^m(\cos\theta) - P_l^{m+1}(\cos\theta).
\end{aligned}
$$

In conclusion, for the case of (a) $\theta \neq 0, \pi$, we can obtain all the Legendre polynomials and the derivatives.

(b) Legendre polynomials and its derivatives at $\theta = 0, \pi$

Here, we consider the case of (b) $\theta = 0, \pi$. Because of the parity of Legendre polynomials and the derivatives (cf. the equation (B.18) (B.19)), we only explain the case of $\theta = 0$. From the definition of Legendre polynomials:

$$
\begin{aligned}
P_l^m(\cos\theta = \cos 0 = 1) &= \sin^m 0\left(\frac{d^m P_l}{d\cos\theta^m}\right) \\
&= \begin{cases} 0 & [m \neq 0] \\ P_l(1) & [m = 0] \end{cases}
\end{aligned}
$$

and the characteristics of Legendre polynomials:

$$P_l(1) = 1, \tag{B.27}$$

we obtain Legendre polynomials at $\theta = 0$

$$P_l^m(1) = \begin{cases} 0 & [m \neq 0] \\ 1 \xrightarrow{normalization} \sqrt{\frac{2l+1}{2}} & [m = 0] \end{cases}. \tag{B.28}$$

As regards the derivatives, using the definition of Legendre polynomials (B.26) yields

$$\begin{aligned}
\frac{dP_l^m}{d\theta} &= \frac{d}{d\theta}\left(\sin^m\theta \frac{d^m P_l}{d\cos\theta^m}\right) \\
&= m\cos\theta\sin^{m-1}\theta\frac{d^m P_l}{d\cos\theta^m} + \sin^m\theta\frac{d\cos\theta}{d\theta}\frac{d^{m+1}P_l}{d\cos\theta^{m+1}} \\
&= m\cos\theta\sin^{m-1}\theta\frac{d^m P_l}{d\cos\theta^m} - \sin^{m+1}\theta\frac{d^{m+1}P_l}{d\cos\theta^{m+1}} \\
&\xrightarrow{\theta=0} \begin{cases} 0 & [m \neq 1] \\ \frac{dP_l(1)}{d\cos\theta} & [m = 1] \end{cases}.
\end{aligned}$$

To see $dP_l^l(\cos\theta)/d\theta$ at $m = 1$ and $\theta = 0$ carefully, we consider the following recursive formula

$$(l - m)\cos\theta P_l^m - (l + m)P_{l-1}^m + \sin\theta P_l^{m+1} = 0. \tag{B.29}$$

At $m = 1$, the formula becomes

$$(l - 1)\cos\theta P_l^1 - (l + 1)P_{l-1}^1 + \sin\theta P_l^2 = 0$$

and operating $\frac{d}{d\theta}$ on it yields

$$(l - 1)\left[-\sin\theta P_l^1 + \cos\theta\frac{dP_l^1}{d\theta}\right] - (l + 1)\frac{dP_{l-1}^1}{d\theta} + \left[\cos\theta P_l^2 + \sin\theta\frac{dP_l^2}{d\theta}\right] = 0.$$

When $\theta = 0$, we get

$$(l - 1)\frac{dP_l^1}{d\theta} - (l + 1)\frac{dP_{l-1}^1}{d\theta} + \cos\theta P_l^2 = 0.$$

From (B.28), because $P_l^2(1) = 0$ $(l > 2)$, the equation turns into

$$\frac{dP_l^1}{d\theta} = \frac{l+1}{l-1}\frac{dP_{l-1}^1}{d\theta}.$$

As a result, we can obtain $dP_l^l(\cos\theta)/d\theta$ at $m = 1, \theta = 0$ by the following recursive method,

$$
\begin{aligned}
\frac{dP_l^1}{d\theta} &= \frac{l+1}{l-1}\frac{dP_{l-1}^1}{d\theta} \\
&= \frac{l+1}{l-1}\frac{l}{l-2}\frac{dP_{l-2}^1}{d\theta} \\
&\;\;\vdots \\
&= \frac{(l+1)l\cdots 3}{(l-1)(l-2)\cdots 2\cdot 1}\frac{dP_1^1}{d\theta} \\
&= \frac{l(l+1)}{2}\cos(\theta = 0) \\
&= \frac{l(l+1)}{2} \\
&\xrightarrow{normalization} \frac{l(l+1)}{2}\sqrt{\frac{(2l+1)(l-1)!}{2(l+1)!}} \\
&= \sqrt{\frac{(2l+1)l(l+1)}{8}}.
\end{aligned}
$$

Consequently, the derivative of Legendre polynomial is

$$
\frac{dP_l^m(1)}{d\theta} = \begin{cases} 0 & [m \neq 1] \\ \sqrt{\frac{(2l+1)l(l+1)}{8}} & [m = 1] \end{cases}. \tag{B.30}
$$

To summarize, the normalized Legendre polynomials and the derivatives at $\theta = 0$ are

$$
P_l^m(1) = \begin{cases} 0 & [m \neq 0] \\ \sqrt{\frac{2l+1}{2}} & [m = 0] \end{cases}, \qquad \frac{dP_l^m(1)}{d\theta} = \begin{cases} 0 & [m \neq 1] \\ \sqrt{\frac{(2l+1)l(l+1)}{8}} & [m = 1] \end{cases}.
$$

B.4   Integrate through longitude ϕ and latitude θ

With obtained Legendre polynomials and the derivatives, we calculate the summation (B.9) and (B.10). As regards the terms about toroidal motion (the case of poloidal motion can be described similarly), $\boldsymbol{u}\cdot\mathbf{C_l^{m*}}$ (B.11), the product of it and r is (this expression is just for clear description)

$$r\left(\boldsymbol{u}\cdot\mathbf{C_l^{m*}}\right) = u_\theta \frac{m}{\sin\theta} P_l^m(\cos\theta)\left(-i\cos m\phi - \sin m\phi\right) - u_\phi\left(\frac{\partial P_l^m(\cos\theta)}{\partial\theta}\right)\left(\cos m\phi - i\sin m\phi\right)$$

$$= -\frac{m}{\sin\theta} P_l^m(\cos\theta)\left[u_\theta(\theta,\phi)\sin m\phi\right] - \left(\frac{\partial P_l^m(\cos\theta)}{\partial\theta}\right)\left[u_\phi(\theta,\phi)\cos m\phi\right]$$

$$- i\left[\frac{m}{\sin\theta} P_l^m(\cos\theta)\left[u_\theta(\theta,\phi)\cos m\phi\right] + \left(\frac{\partial P_l^m(\cos\theta)}{\partial\theta}\right)\left[u_\phi(\theta,\phi)\sin m\phi\right]\right].$$

$$(B.31)$$

Operating integral $\int_0^{2\pi} d\phi$, that is, numerically summation $\sum_{i=1}^{3600}(0.1\pi/180)$, on the product yields (we extract a part of every term associated with ϕ)

$$\int_0^{2\pi}\left[u_\theta(\theta,\phi)\sin m\phi\right]d\phi \approx \sum_{i=1}^{3600}\left[u_\theta(\theta,\phi(i))\sin m\phi(i)\right](0.1\pi/180) \equiv TS(m,\theta)$$

$$\int_0^{2\pi}\left[u_\phi(\theta,\phi)\cos m\phi\right]d\phi \approx \sum_{i=1}^{3600}\left[u_\phi(\theta,\phi(i))\cos m\phi(i)\right](0.1\pi/180) \equiv PC(m,\theta)$$

$$\int_0^{2\pi}\left[u_\theta(\theta,\phi)\cos m\phi\right]d\phi \approx \sum_{i=1}^{3600}\left[u_\theta(\theta,\phi(i))\cos m\phi(i)\right](0.1\pi/180) \equiv TC(m,\theta)$$

$$\int_0^{2\pi}\left[u_\phi(\theta,\phi)\sin m\phi\right]d\phi \approx \sum_{i=1}^{3600}\left[u_\phi(\theta,\phi(i))\sin m\phi(i)\right](0.1\pi/180) \equiv PS(m,\theta)$$

where two-letter functions represent their component, T:u_θ, P:u_ϕ, S:sin, C:cos, and $\phi(i) = 0.1i\cdot\pi/180$. At this point, $\int_0^{2\pi} r\left(\boldsymbol{u}\cdot\mathbf{C_l^{m*}}\right)d\phi$ is

$$\int_0^{2\pi} r\left(\boldsymbol{u}\cdot\mathbf{C_l^{m*}}\right)d\phi = -\frac{m}{\sin\theta} P_l^m(\cos\theta)\,TS(m,\theta) - \left(\frac{\partial P_l^m(\cos\theta)}{\partial\theta}\right)PC(m,\theta)$$

$$- i\left[\frac{m}{\sin\theta} P_l^m(\cos\theta)\,TC(m,\theta) + \left(\frac{\partial P_l^m(\cos\theta)}{\partial\theta}\right)PS(m,\theta)\right].$$

Next, operating integral of θ, $\int_0^\pi \sin\theta\, d\theta$, i.e., numerically summation $\sum_{i=1}^{1801}(0.1\pi/180)$, we can write the result in a simple form by using parity of Legendre polynomials and the derivatives as follows. In respect to the terms with TS, using the parity of Legendre polynomials (B.18), we can change it like this

$$-\int_0^\pi \frac{m}{\sin\theta} P_l^m(\cos\theta)\, TS(m,\theta)\sin\theta\, d\theta$$

$$= -\int_0^\pi m P_l^m(\cos\theta)\, TS(m,\theta)\, d\theta$$

$$= -\left[\int_0^{\pi/2} m P_l^m(\cos\theta)\, TS(m,\theta)\, d\theta + \int_{\pi/2}^\pi m P_l^m(\cos\theta)\, TS(m,\theta)\, d\theta\right]$$

$$= -\left[\int_0^{\pi/2} m P_l^m(\cos\theta)\, TS(m,\theta)\, d\theta + \int_0^{\pi/2} m P_l^m(\cos(\pi-\theta))\, TS(m,(\pi-\theta))\, d\theta\right]$$

$$= -\int_0^{\pi/2} m\left[P_l^m(\cos\theta)\, TS(m,\theta) + P_l^m(-\cos\theta)\, TS(m,(\pi-\theta))\right] d\theta$$

$$= -\int_0^{\pi/2} m P_l^m(\cos\theta)\left[TS(m,\theta) + (-1)^{l+m} TS(m,(\pi-\theta))\right] d\theta$$

$$\approx -\sum_{j=1}^{900} m P_l^m\big(\cos\theta(j)\big)\left[TS(m,\theta(j)) + (-1)^{l+m} TS(m,(\pi-\theta(j)))\right] (0.1\pi/180)$$

$$\quad - m P_l^m\left(\cos(\theta = \frac{\pi}{2})\right) TS(m,(\theta = \frac{\pi}{2}))(0.1\pi/180)$$

$$\equiv TRe1(m)$$

where $\theta(j) = 0.1 j \cdot \pi/180$ and the function $TRe1(m)$ depends only on the order m. Similarly, using the parity of Legendre polynomials (B.18) and the derivatives (B.19), the terms with PC, TC, and PS become

$$-\int_0^\pi \left(\frac{\partial P_l^m(\cos\theta)}{\partial\theta}\right) PC(m,\theta)\sin\theta\, d\theta$$

$$= -\int_0^{\pi/2} \left(\frac{\partial P_l^m(\cos\theta)}{\partial\theta}\right) PC(m,\theta)\sin\theta\, d\theta$$

$$\quad -\int_0^{\pi/2} (-1)^{l+m+1}\left(\frac{\partial P_l^m(\cos\theta)}{\partial\theta}\right) PC(m,(\pi-\theta))\sin(\pi-\theta)\, d\theta$$

$$= -\int_0^{\pi/2} \sin\theta \left(\frac{\partial P_l^m(\cos\theta)}{\partial\theta}\right)\left[PC(m,\theta) + (-1)^{l+m+1} PC(m,(\pi-\theta))\right] d\theta$$

$$\approx -\sum_{j=0}^{900} \sin\theta \left(\frac{\partial P_l^m(\cos\theta)}{\partial\theta}\right)\left[PC(m,\theta) + (-1)^{l+m+1} PC(m,(\pi-\theta))\right] (0.1\pi/180)$$

$$\quad - \sin(\theta = \frac{\pi}{2}) \left(\frac{\partial P_l^m\big(\cos(\theta = \frac{\pi}{2})\big)}{\partial\theta}\right) PC(m,(\theta = \frac{\pi}{2}))(0.1\pi/180)$$

$$\equiv TRe2(m),$$

$$\int_0^\pi \frac{m}{\sin\theta} P_l^m(\cos\theta)\, TC(m,\theta)\sin\theta\, d\theta$$

$$= \int_0^{\pi/2} mP_l^m(\cos\theta)\, TC(m,\theta)\, d\theta + \int_0^{\pi/2} m(-1)^{l+m} P_l^m(\cos\theta)\, TC(m,(\pi-\theta))\, d\theta$$

$$= \int_0^{\pi/2} mP_l^m(\cos\theta)\left[TC(m,\theta) + (-1)^{l+m}TC(m,(\pi-\theta))\right] d\theta$$

$$\approx \sum_{j=0}^{900} mP_l^m(\cos\theta(j))\left[TC(m,\theta(j)) + (-1)^{l+m}TC(m,(\pi-\theta(j)))\right](0.1\pi/180)$$

$$+ mP_l^m\left(\cos(\theta = \frac{\pi}{2})\right) TC(m,(\theta = \frac{\pi}{2}))(0.1\pi/180)$$

$$\equiv TIm1(m),$$

$$\int_0^\pi \left(\frac{\partial P_l^m(\cos\theta)}{\partial\theta}\right) PS(m,\theta)\sin\theta\, d\theta$$

$$= \int_0^{\pi/2}\left(\frac{\partial P_l^m(\cos\theta)}{\partial\theta}\right) PS(m,\theta)\sin\theta\, d\theta$$

$$+ \int_0^{\pi/2}(-1)^{l+m+1}\left(\frac{\partial P_l^m(\cos\theta)}{\partial\theta}\right) PS(m,(\pi-\theta))\sin(\pi-\theta)\, d\theta$$

$$= \int_0^{\pi/2}\sin\theta\left(\frac{\partial P_l^m(\cos\theta)}{\partial\theta}\right)\left[PS(m,\theta) + (-1)^{l+m+1}PS(m,(\pi-\theta))\right] d\theta$$

$$\approx \sum_{j=0}^{900}\sin\theta\left(\frac{\partial P_l^m(\cos\theta)}{\partial\theta}\right)\left[PS(m,\theta) + (-1)^{l+m+1}PS(m,(\pi-\theta))\right](0.1\pi/180)$$

$$+ \sin(\theta = \frac{\pi}{2})\left(\frac{\partial P_l^m\left(\cos(\theta = \frac{\pi}{2})\right)}{\partial\theta}\right) PS(m,(\theta = \frac{\pi}{2}))(0.1\pi/180)$$

$$\equiv TIm2(m)$$

where the letters of the resulted functions represent T:toroidal, P:poloidal, Re:Real, Im:Imaginary, and (1 or 2):the number of the function. In conclusion, $r\left(\boldsymbol{u}\cdot\mathbf{C_l^{m*}}\right)$ is calculated

$$\int_0^\pi \int_0^{2\pi} r\left(\boldsymbol{u}\cdot\mathbf{C_l^{m*}}\right) d\phi\sin\theta\, d\theta = TRe1(m) + TRe2(m) - i\left[TIm1(m) + TIm2(m)\right]$$

$$\equiv [TRe(m)] - i[TIm(m)]$$

$$= \left(c_l^m \frac{\pi l(l+1)}{r^2}\right) r \qquad \text{(from (B.5))}$$

and we can thus describe c_l^m as

$$c_l^m = \frac{r}{\pi l(l+1)} \left[-TRe(m) - i\, TIm(m) \right].$$ (B.32)

Likewise, we can calculate the coefficient of poloidal motion, b_l^m. The important point is that we can use TS, TC, PS, and PC calculated above again, which reduces the calculation time. The $r\left(\boldsymbol{u} \cdot \mathbf{B_l^{m*}}\right)$ accordingly becomes

$$
\begin{aligned}
r\left(\boldsymbol{u} \cdot \mathbf{B_l^{m*}}\right) &= u_\theta \left(\frac{\partial P_l^m(\cos\theta)}{\partial\theta} \right)(\cos m\phi - i\sin m\phi) + u_\phi \frac{m}{\sin\theta} P_l^m(\cos\theta)\left(-i\cos m\phi - \sin m\phi\right) \\
&= \left(\frac{\partial P_l^m(\cos\theta)}{\partial\theta} \right)\left[u_\theta(\theta,\phi)\cos m\phi \right] - \frac{m}{\sin\theta} P_l^m(\cos\theta)\left[u_\phi(\theta,\phi)\sin m\phi \right] \\
&\quad - i\left[\left(\frac{\partial P_l^m(\cos\theta)}{\partial\theta} \right)\left[u_\theta(\theta,\phi)\sin m\phi \right] + \frac{m}{\sin\theta} P_l^m(\cos\theta)\left[u_\phi(\theta,\phi)\cos m\phi \right] \right] \\
&\xrightarrow{\int d\phi} \left(\frac{\partial P_l^m(\cos\theta)}{\partial\theta} \right) TC(\theta,\phi) - \frac{m}{\sin\theta} P_l^m(\cos\theta)\, PS(\theta,\phi) \\
&\quad - i\left[\left(\frac{\partial P_l^m(\cos\theta)}{\partial\theta} \right) TS(\theta,\phi) + \frac{m}{\sin\theta} P_l^m(\cos\theta)\, PC(\theta,\phi) \right] \\
&\xrightarrow{\int \sin\theta\, d\theta} \int_0^\pi \sin\theta \left(\frac{\partial P_l^m(\cos\theta)}{\partial\theta} \right) TC(\theta,\phi) - m P_l^m(\cos\theta)\, PS(\theta,\phi) \\
&\quad - i\left[\sin\theta \left(\frac{\partial P_l^m(\cos\theta)}{\partial\theta} \right) TS(\theta,\phi) + m P_l^m(\cos\theta)\, PC(\theta,\phi) \right] d\theta \\
&\equiv PRe1(m) + PRe2(m) - i\left[PIm1(m) + PIm2(m) \right] \\
&\equiv \left[PRe(m) \right] - i\left[PIm(m) \right] \\
&= \left(b_l^m \frac{\pi l(l+1)}{r^2} \right) r
\end{aligned}
$$

where $\xrightarrow{\int d\phi}$ and $\xrightarrow{\int \sin\theta\, d\theta}$ represent operating $\int_0^{2\pi} d\phi$ and $\int_0^\pi \sin\theta\, d\theta$ on the equation, respectively. Hence, we can get b_l^m

$$b_l^m = \frac{r}{\pi l(l+1)} \left[PRe(m) - i\, PIm(m) \right].$$ (B.33)

Finally, we acquire the coefficients of toroidal and poloidal motion, c_l^m and b_l^m, and thus the degree power spectra of toroidal and poloidal motion, $\sigma_T(l)$ and $\sigma_P(l)$, from the equation (B.1) and (B.2).

B.5   Formulae of Legendre polynomials

This is the list of definitions and formulae we used in this paper. The references are Terazawa (1983) (in Japanese) and Moriguchi (1987) (in Japanese).

Definition of Legendre function:

$$P_l(\cos\theta) = \sum_{s=0}^{\leq l/2} (-1)^s \frac{(2l-2s)!}{2^l s!(l-s)!(l-2s)!} \cos^{l-s2}\theta \tag{B.34}$$

Legendre function at the endpoint:

$$P_l(\cos\theta) = \begin{cases} 1 & [\theta = 0] \\ (-1)^l & [\theta = \pi] \end{cases} \tag{B.35}$$

Definition of Legendre polynomials:

$$P_l^m(\cos\theta) = \sin^m\theta \frac{d^m P_l(\cos\theta)}{d\cos\theta^m} \tag{B.36}$$

Definite integrals of Legendre polynomials:

$$\int_{-1}^{1} P_n^m(x) P_l^m(x)\,dx = \begin{cases} 0 & [n \neq l] \\ \frac{2(l+m)!}{(2l+1)(l-m)!} & [n = l] \end{cases} \tag{B.37}$$

$$\int_0^\pi \left[\frac{m^2}{\sin^2\theta} P_n^m(\cos\theta) P_l^m(\cos\theta) + \frac{dP_n^m(\cos\theta)}{d\theta} \frac{dP_l^m(\cos\theta)}{d\theta} \right] \sin\theta\,d\theta = \begin{cases} 0 & [n \neq l] \\ \frac{2l(l+1)(l+m)!}{(2l+1)(l-m)!} & [n = l] \end{cases} \tag{B.38}$$

Recursive formula of Legendre polynomials:

$$(l-m+1)P_{l+1}^m - (2l+1)\cos\theta P_l^m + (l+m)P_{l-1}^m = 0 \tag{B.39}$$

$$(l-m)\cos\theta P_l^m - (l+m)P_l^m + \sin\theta P_l^{m+1} = 0 \tag{B.40}$$

$$P_l^{m+2} - 2(m+1)\frac{\cos\theta}{\sin\theta} P_l^{m+1} + (l-m)(l+m+1)P_l^m = 0 \tag{B.41}$$

Parity of Legendre polynomials:

$$P_l^m(\cos(\pi-\theta)) = P_l^m(-\cos\theta) = (-1)^{l+m} P_l^m(\cos\theta) \tag{B.42}$$

$$\frac{dP_l^m(\cos(\pi-\theta))}{d(\pi-\theta)} = -\frac{dP_l^m(\cos(\pi-\theta))}{d\theta} = (-1)^{l+m+1} \frac{dP_l^m(\cos\theta)}{d\theta} \tag{B.43}$$

Legendre polynomials for order $m = l$:

$$P_l^l(\cos\theta) = (2l-1)!! \sin^l\theta \tag{B.44}$$

where

$$(2l-1)!! = (2l-1)(2l-3)(2l-5)\cdots 3 \cdot 1$$

Appendix C

Effect of plate geometry on the toroidal/poloidal ratio

Here we investigate the effect of various plate geometries on the toroidal/poloidal ratio. We consider the effect of the size, aspect ratio, roundness of plate and the ratio of transform fault to ridge and subduction zone.

C.1 Effect of plate size

First, we consider the effect of plate size on the toroidal/poloidal ratio. We make four virtual square plates with a different plate size (Large: 60°×60°, Small: 30°×30°, Tiny: 10°× 10°, Micro: 2°×2°) and impose a straight motion by putting the same Euler pole (1°/Myr) at the North Pole (Figure C.1) or a spin motion by putting the same Euler pole (1°/Myr) at the center of the plate (Figure C.4). The results of spherical harmonic expansion ($2 < l < 1000$) are Figure C.2, C.3, C.5 and C.6.

With a straight motion, the correlation between the plate size and the toroidal/poloidal ratio is weak compared with that of a spin motion. Although the result of the small plates are almost constant, they are expected to take the small peaks at higher spherical harmonic degrees than 1000. Figure C.3 shows l^{-1} decay, which is a common feature of the toroidal-poloidal spectrum in plate tectonics (O'Connell et al., 1991). Another notable fea-

Fig. C.1   Straight motion of ideal plates with a different plate size. The size: [top, left] Large: $60° \times 60°$; [top, right] Small: $30° \times 30°$; [bottom, left] Tiny: $10° \times 10°$; [bottom, right] Micro: $2° \times 2°$. All the plate has the same Euler pole at the North Pole and orange vectors represents the induced eastward motion.

ture is a soaring of spectrum of small plates, indicating that smaller plate might affect the observed toroidal/poloidal ratio at higher degrees.

With a spin motion, similarly to the case of straight motion, the plate size affects the spherical harmonic degrees taking the peak of the spectra, i.e., the smaller the plate, the higher the spherical harmonic degrees of the peak of the spectrum. One notable feature

Size Effect with Straight Motion
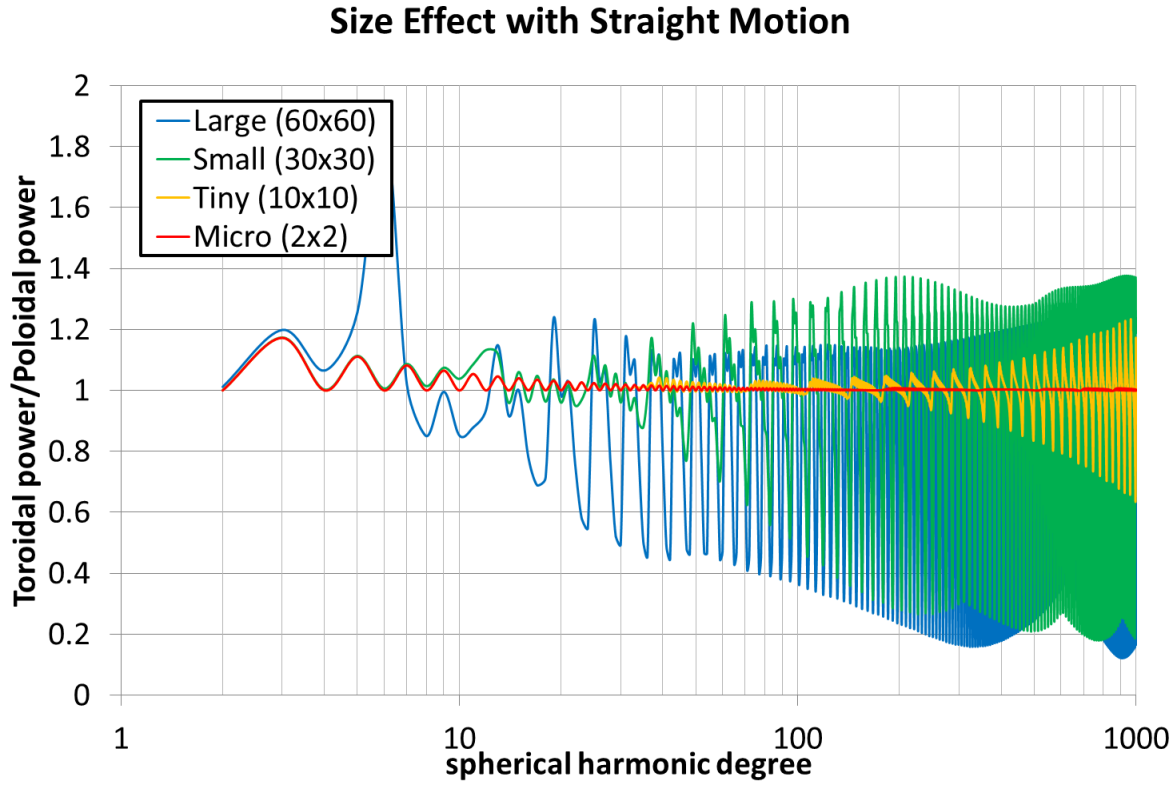
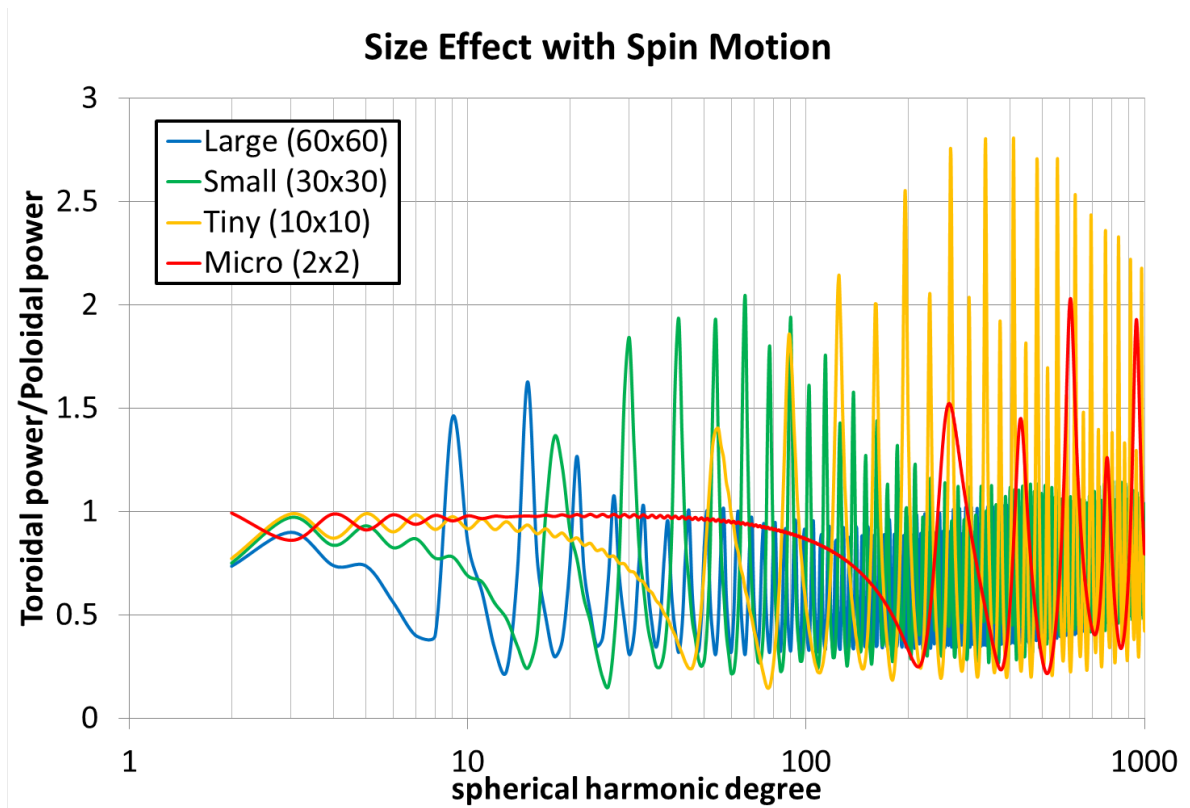Fig. C.2   Toroidal/poloidal ratio of plates with a different size in the case of a straight motion. Blue, green, orange and red lines represent the result of Large, Small, Tiny and Micro, respectively.

about the power spectra is that spectra of small plates (bright blue and orange lines in Figure C.6) exhibit soaring instead of l^{-1} decay. Moreover, considering a fast spin motion of a small plate (Figure 3.3), the magnitude of the spectra (dashed bright blue and orange lines in Figure C.6) is comparable to that of the large plates (red and blue lines in Figure C.6)and the difference between the observed toroidal and poloidal power spectra (gray and black line in Figure C.6). Therefore, it is conceivable that the spin motions of small plates affect the observed toroidal/poloidal ratio at high spherical harmonic degrees as we showed in Figure 2.3. From these results, we argue that there is a correlation between the plate size and the toroidal/poloidal ratio particularly when the plate holds a spin motion.

Accordingly, in order to comprehend the effect of plate size especially with a spin motion, we focus on the Easter plate, at which an active spin motion is observed in previ-
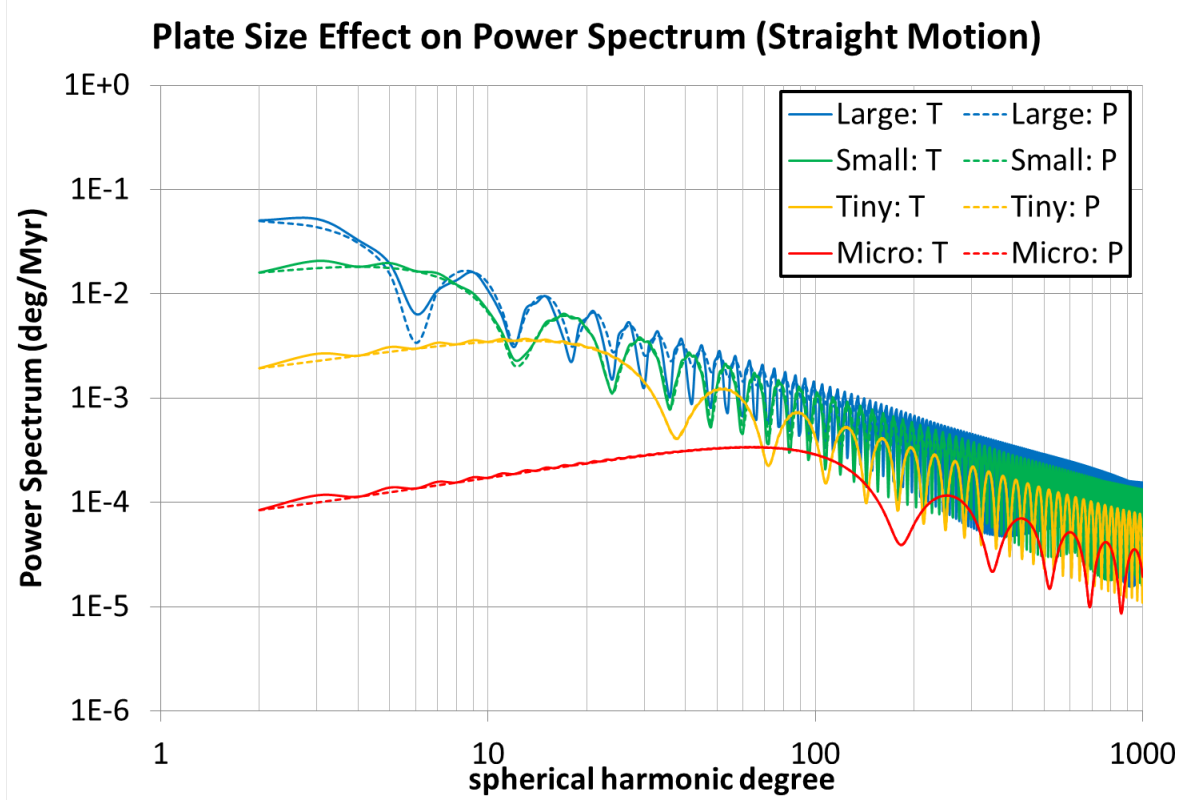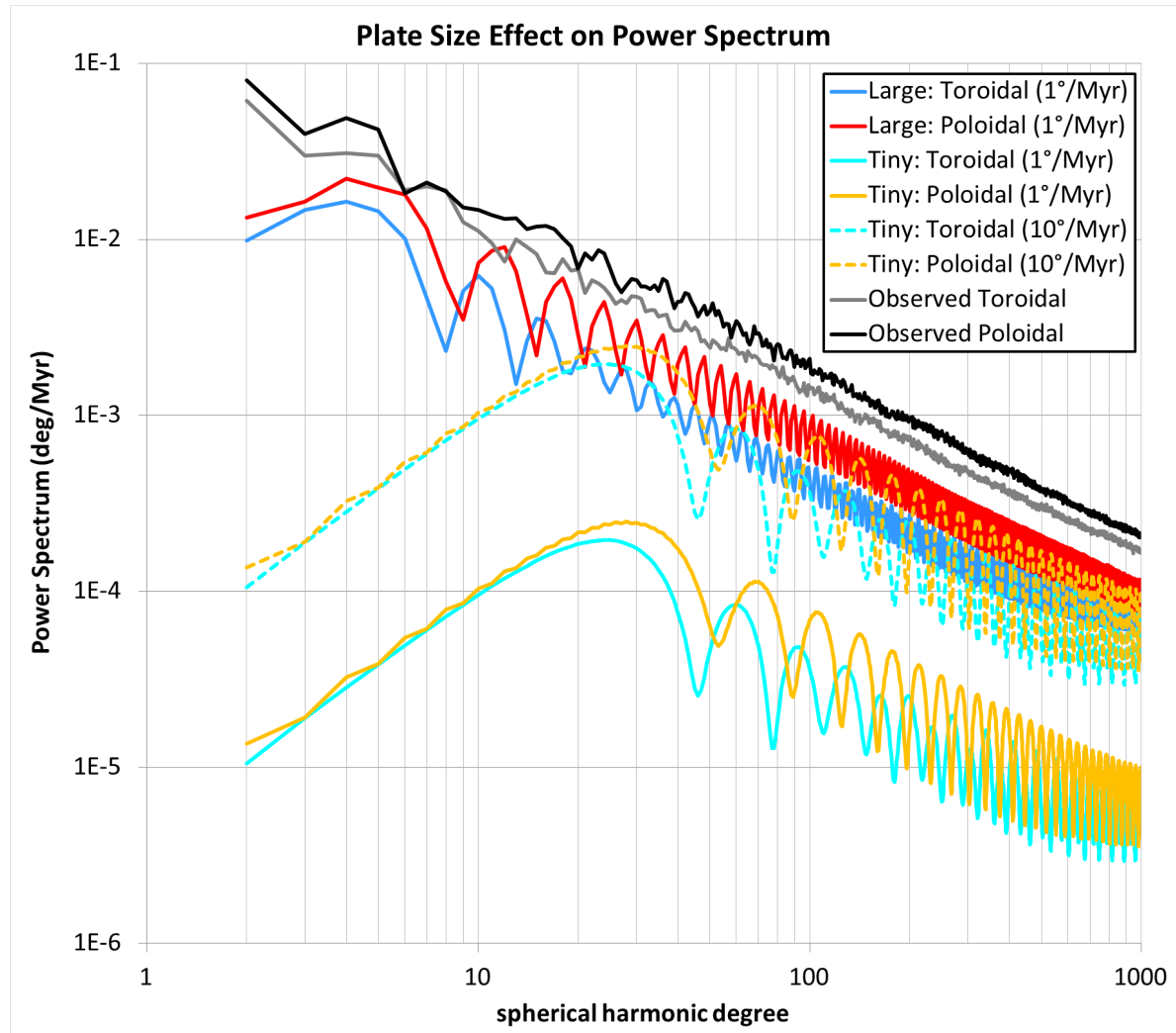
Fig. C.3 Toroidal-poloidal power spectrum of plates with a different size in the case of a straight motion. Solid and dashed lines represent toroidal and poloidal power spectrum, respectively. Blue, green, orange and red lines represent the result of Large, Small, Tiny and Micro, respectively.

ous work (Schouten et al., 1993), and extract a part of the observed Euler pole component which passes the center of the Easter plate, ω_C in Section 3.1. Then, we impose only the extracted Euler pole on the Easter plate to generate the spin motion and calculate the toroidal/poloidal ratio. Please note that in this case the other plates do not move and solely the Easter plate holds its spin motion by excluding the straight component. The result is Figure C.7. Figure C.7 shows that the spin motion of the Easter plate clearly increases the toroidal/poloidal ratio at high spherical harmonic degrees ($l > 100$), which reinforces a strong correlation between the size of plate with a spin motion and the toroidal/poloidal ratio. Please ensure that since the toroidal-poloidal decomposition is a linear analysis the result of the whole toroidal/poloidal ratio from observed global plate motion is summa-
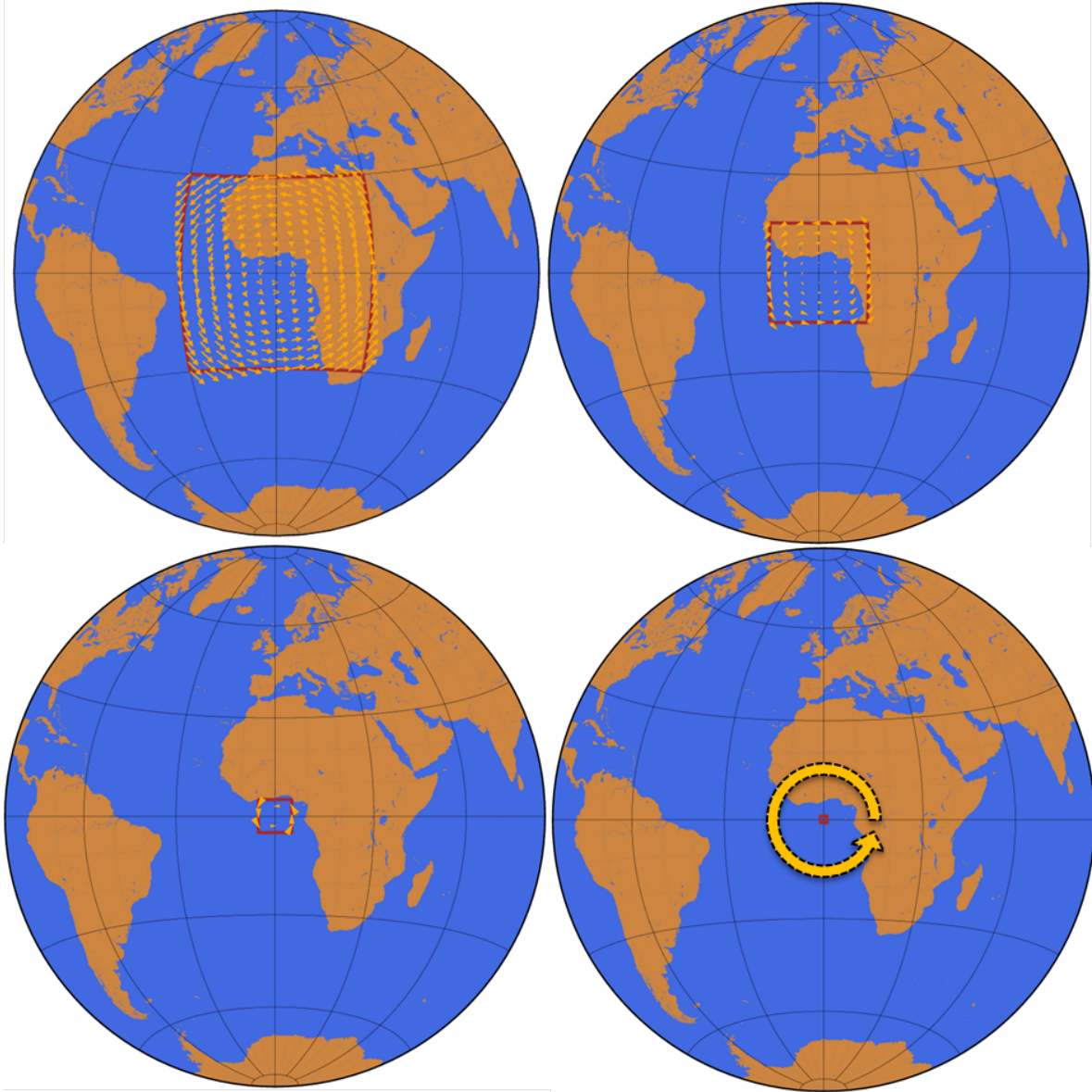
Fig. C.4   Spin motion of ideal plates with a different plate size. Regarding the size of plate, please refer to the caption of Figure C.1. All the plate has the same Euler pole at the center and orange vectors represents the induced counterclockwise spin motion (we put a large circular vector in the case of Micro plate for clarity).

tion of that of a part of the plate motion, such as the spin of the Easter plate of this example.

Therefore, we conclude that there is a clear relationship between the spin motion of indi-

vidual plate and the toroidal/poloidal ratio. As a future work, we need to investigate how

important the spin motion of small plate is in the observed toroidal/poloidal ratio.

Fig. C.5   Toroidal/poloidal ratio of plates with a different size in the case of a spin motion. Blue, green, orange and red lines represent the result of Large, Small, Tiny and Micro, respectively.

Fig. C.6   Toroidal-poloidal power spectrum of plates with a different size in the case of a spin motion. Blue and red lines represent toroidal and poloidal power spectrum of spin motion of "Large" plate, respectively. Bright blue and yellow lines represent toroidal and poloidal power spectrum of spin motion of "Tiny" plate, respectively. In the model plate cases, the rotation rate of solid and dashed lines are 1 and 10 degree/Myr, respectively. Gray and black lines are observed toroidal and poloidal power spectrum, respectively (Figure 2.2).
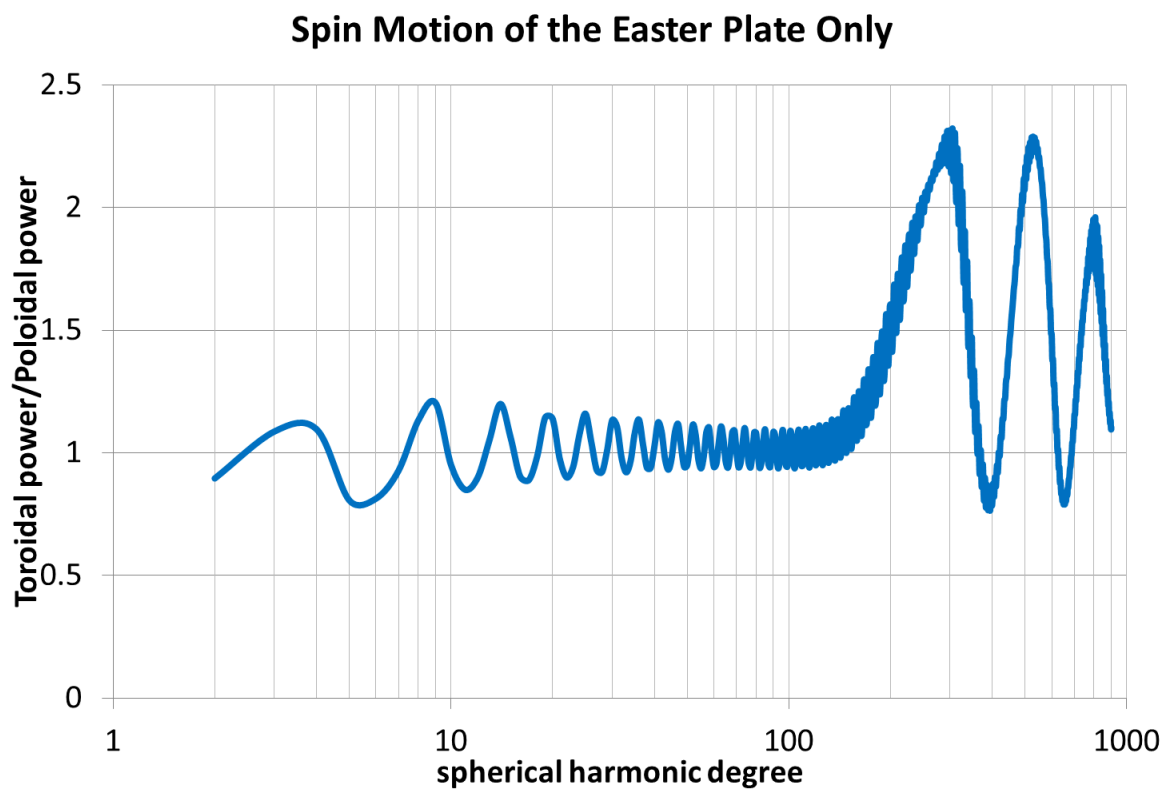
Fig. C.7   Toroidal/poloidal ratio of the spin motion of the Easter plate. We analyze only the extracted Euler pole on the Easter plate to generate the spin motion and calculate the toroidal/poloidal ratio. Please note that in this case the other plates do not move and solely the Easter plate holds its spin motion by excluding the straight component.

C.2   Effect of aspect ratio

In order to examine the effect of plate aspect ratio upon the toroidal/poloidal ratio, we impose straight (Figure C.8) or spin motion (Figure C.11) on one virtual rectangular plate on the Earth which we change its aspect ratio from 1 (square) to 3 with keeping the area almost same. The results of spherical harmonic expansion ($2 < l < 100$) are Figure C.10 and C.13. We also plot the toroidal-poloidal power spectra (Figure C.9 and C.12) since the magnitude of each power spectra is important to change the ratio of global toroidal/poloidal ratio (Figure 2.3).

When we impose solely straight motion on a rectangular plate by putting the same Euler pole (1°/Myr) at the North pole (Figure C.10), the toroidal/poloidal ratio, especially the maximum value, increases to approximately 8 in the case of aspect ratio 3 as the correlation was pointed out by Olson and Bercovici (1991). The reason of the correlation is that, as the aspect ratio increases, the length of plate boundary with the strike-slip motion increases and that with the divergent-convergent motion decreases (Figure C.8).

When we put a spin motion on a plate by imposing the same Euler pole (1°/Myr) at the center of the plate (Figure C.13), generally there is a correlation between the aspect ratio and the toroidal/poloidal ratio, yet the amplitude of the spectrum is less than that generated by straight motions. This feature is shown more clearly in power spectra (Figure C.12), in which the amplitude of toroidal-poloidal spectra is almost same. Another notable characteristic is that the high amplitude in the result of spin motion with the aspect ratio 2.5 and 3 continues to a higher spherical harmonic degrees, i.e., smaller scale of motions, compared with the result of the straight motion, which implies that the short sides of rectangular plates generate a high toroidal/poloidal ratio in the case of spin motion. Faster motion along the short sides because of higher aspect ratio, i.e., longer distance from the
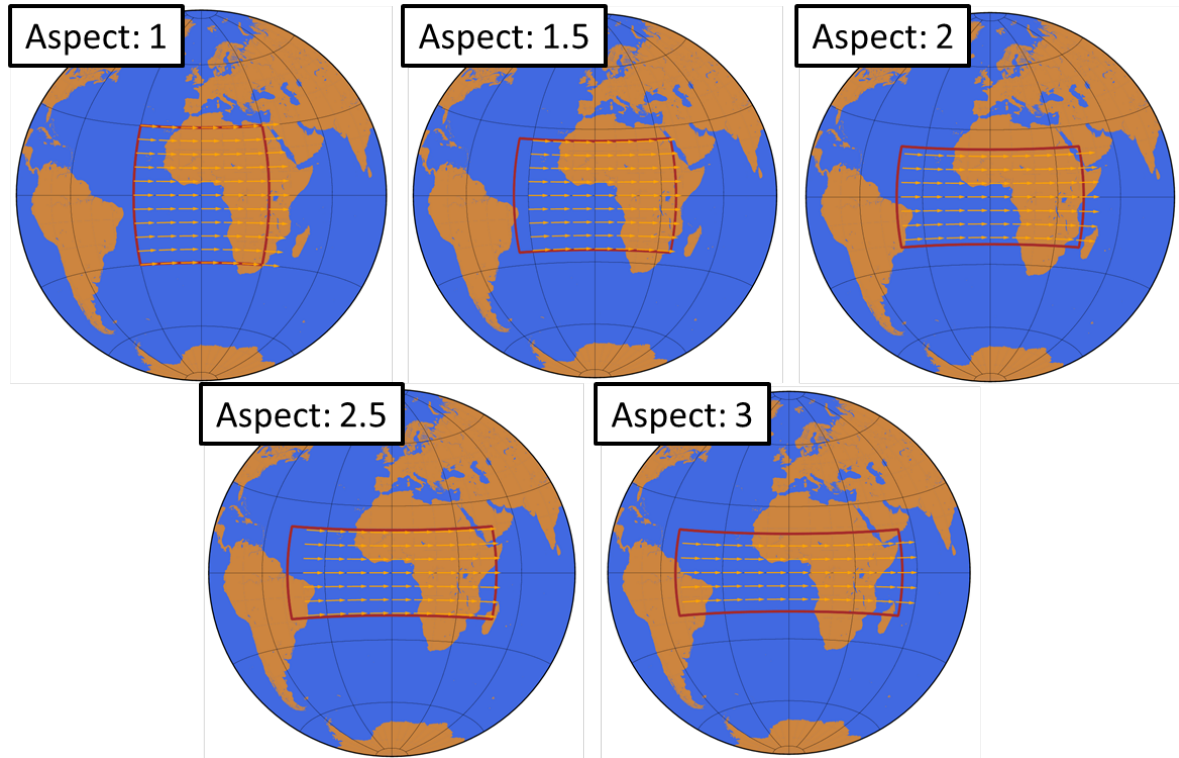
Fig. C.8   Straight motion of ideal plates with a different aspect ratio. Top: left to right, the aspect ratio is 1, 1.5 and 2. Bottom: left to right, the aspect ratio is 2.5 and 3. The aspect ratio is defined as the ratio of "the length of a plate parallel to the plate motion" to "that normal to the plate motion". All the plates have the same area.

Euler pole at the center of the plate, might produce the higher toroidal/poloidal ratio. Another features of the result is that, whereas the amplitude of spectra of the aspect ratio 2.5 and 3 is large, that of the aspect ratio 1, 1.5 and 2 does not vary so much, indicating that the effect of aspect ratio with spin motion is not strong especially when we compare it with the result of the straight motion.

Though the correlation between the aspect ratio of a plate with a spin motion and the toroidal/poloidal ratio is not strong, we confirm that generally there is a correlation between the aspect ratio and the toroidal/poloidal ratio. In order to understand the effect of the aspect ratio on the observed toroidal/poloidal ratio, we plot the aspect ratio (the length of a plate parallel and normal to the observed plate motion) and its plate size in Figure C.14. Figure C.14 demonstrates that although several plates hold a high aspect ra-
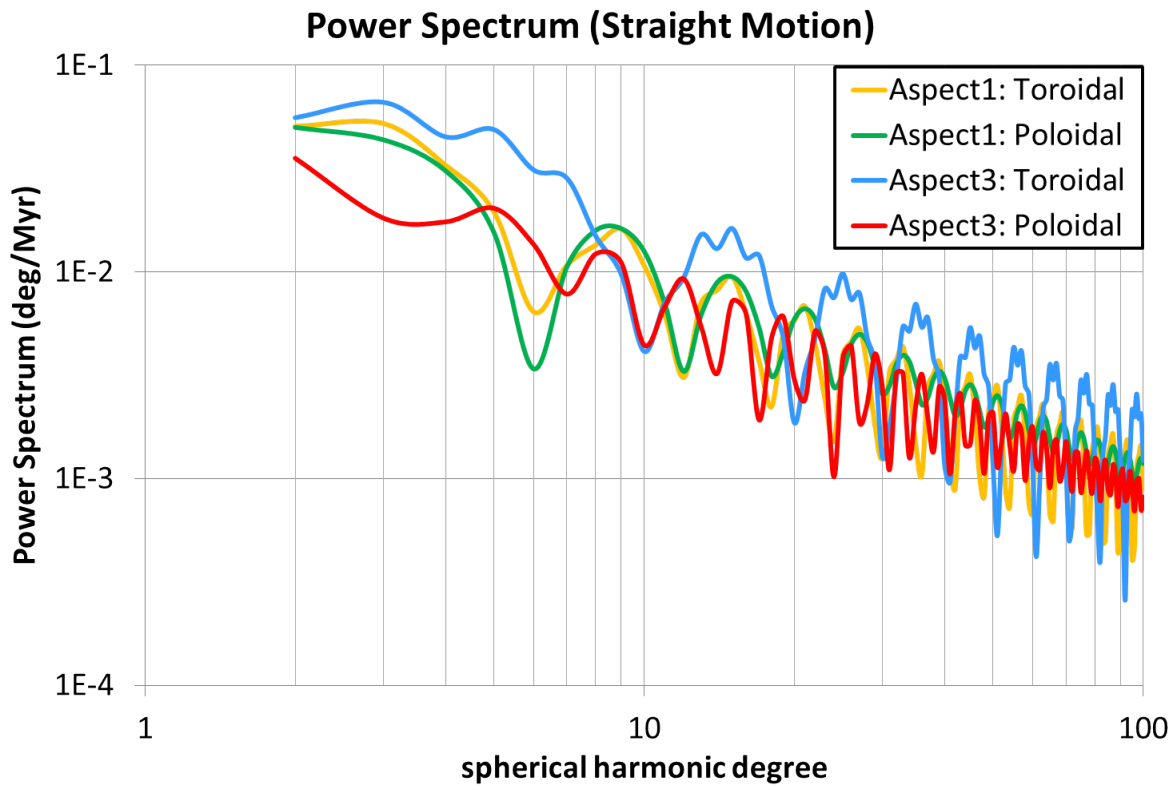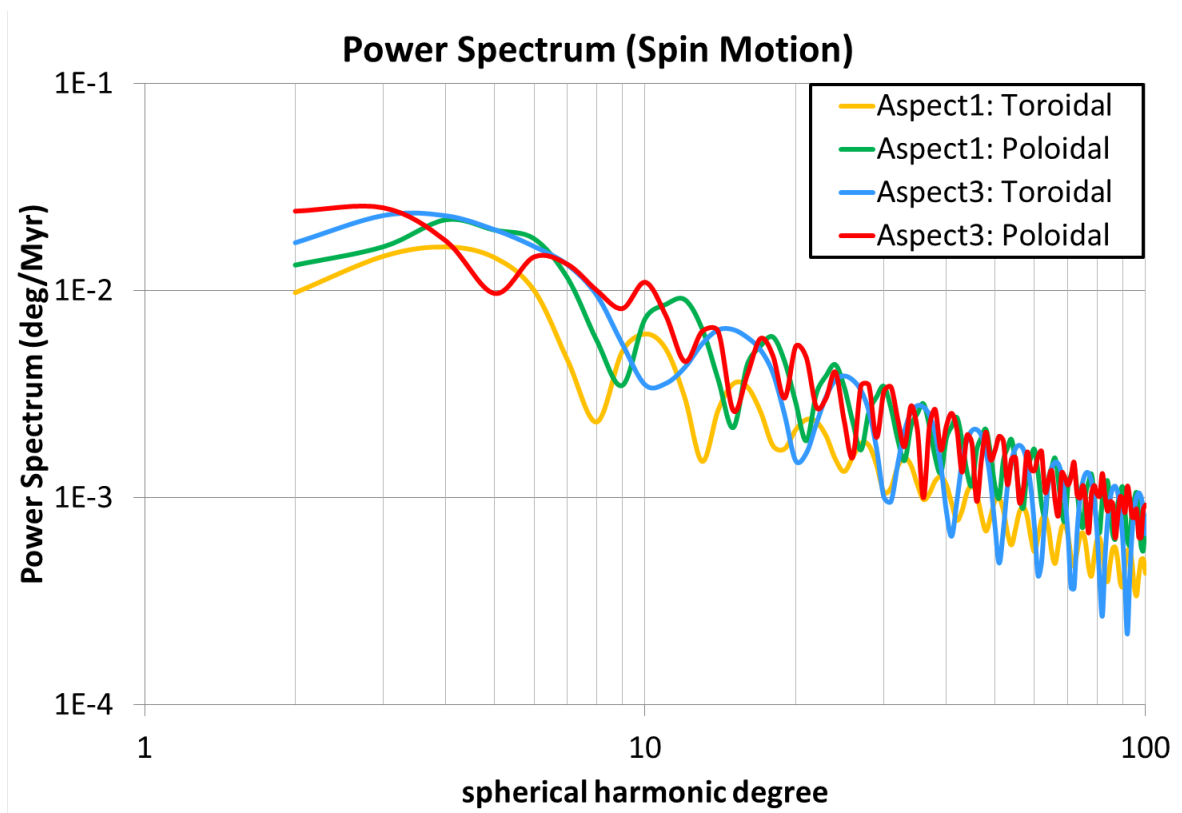
Fig. C.9   Toroidal-poloidal power of the plate with a different aspect ratio in the case of straight motion. Orange and green lines represent the result of toroidal and poloidal spectrum of the aspect ratio 1, respectively. Blue and red lines represent the result of toroidal and poloidal spectrum of the aspect ratio 3, respectively.

tio, there is no systematic correlation between the aspect ratio and the plate size. Thus, the

aspect ratio of plate geometry does not induce the increase in the toroidal/poloidal ratio.
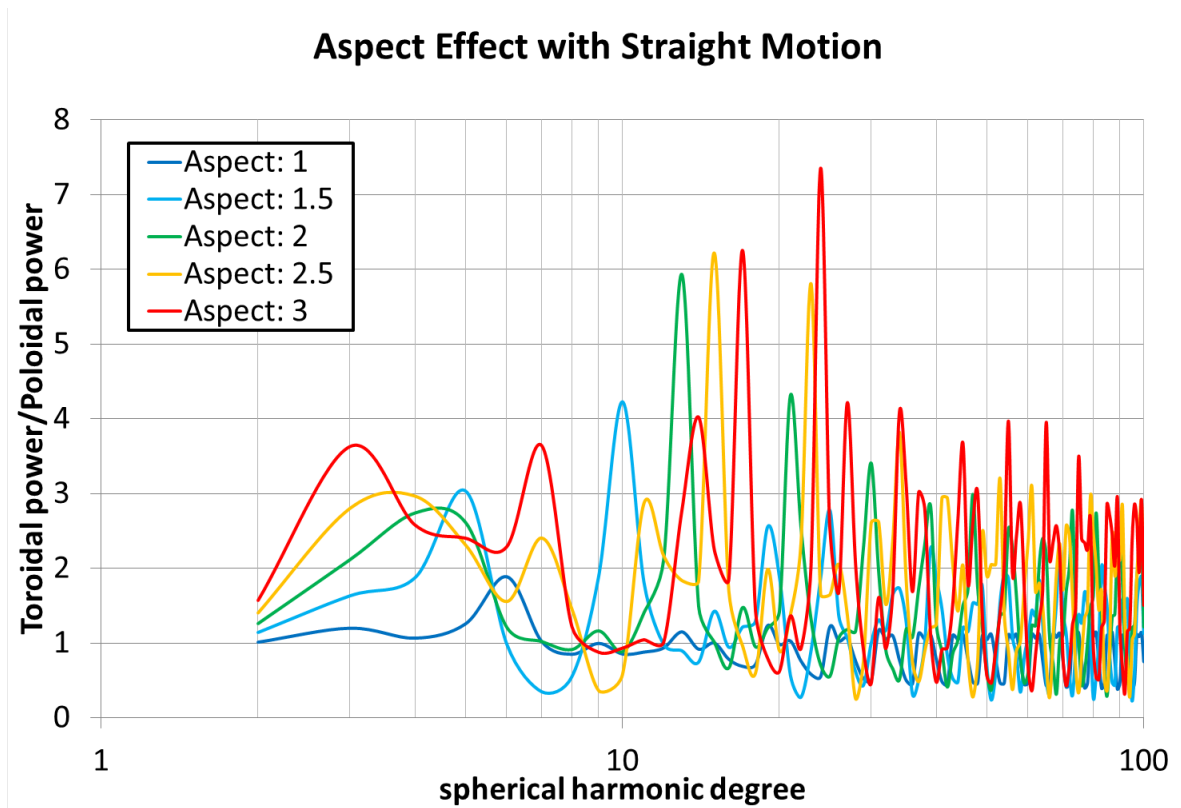
Fig. C.10   Toroidal/poloidal ratio of the plate with a different aspect ratio in the case of straight motion. Dark-blue, light-blue, green, orange and red lines represent the result of the aspect ratio $1, 1.5, 2, 2.5$ and 3, respectively.
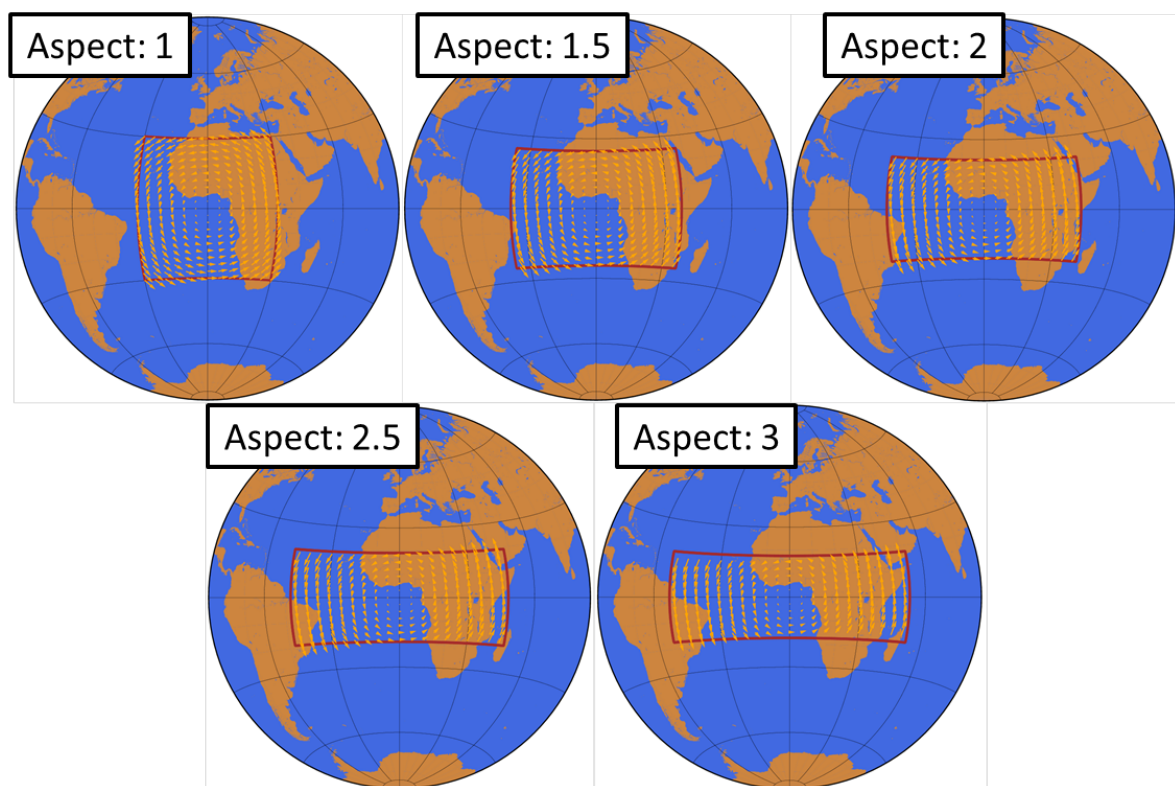
Fig. C.11   Spin motion of ideal plates with a different aspect ratio. Please refer to Figure C.8 for the explanation.

Fig. C.12   Toroidal-poloidal power of the plate with a different aspect ratio in the case of spin motion. Orange and green lines represent the result of toroidal and poloidal spectrum of the aspect ratio 1, respectively. Blue and red lines represent the result of toroidal and poloidal spectrum of the aspect ratio 3, respectively.
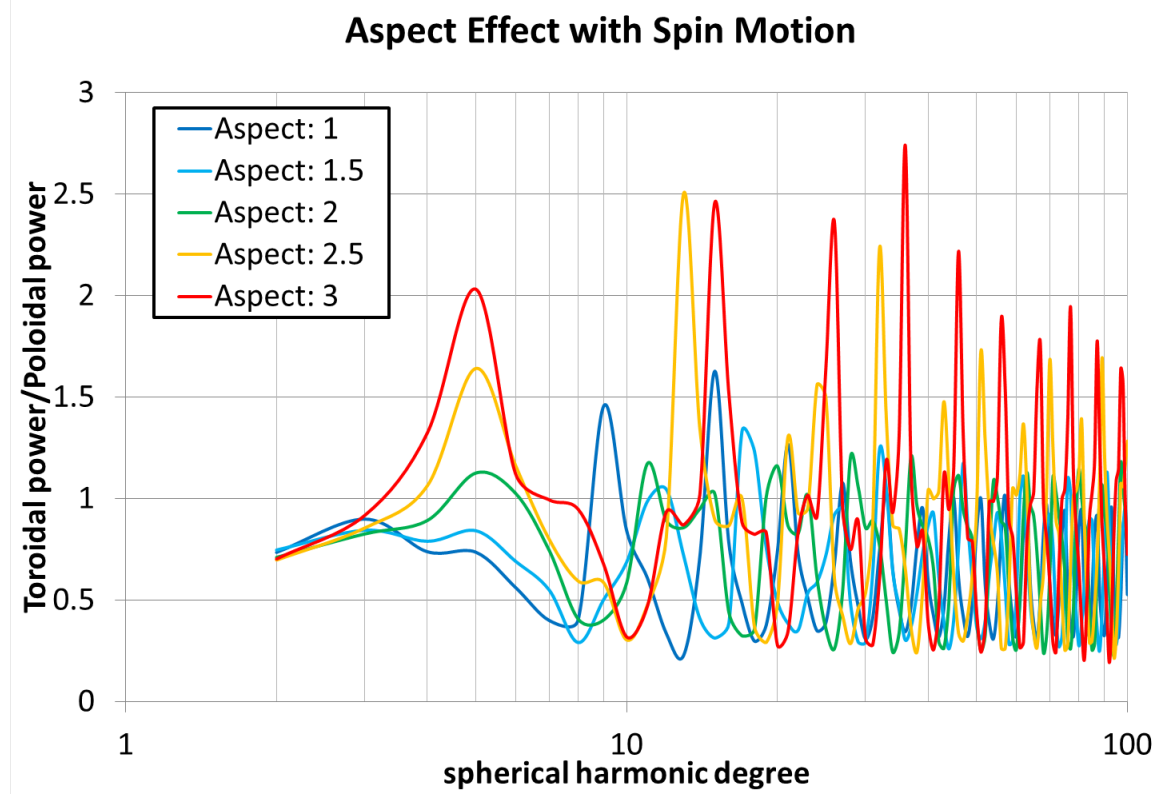
Fig. C.13   Toroidal/poloidal ratio of the plate with a different aspect ratio in the case of spin motion. Dark-blue, light-blue, green, orange and red lines represent the result of the aspect ratio $1, 1.5, 2, 2.5$ and 3, respectively.
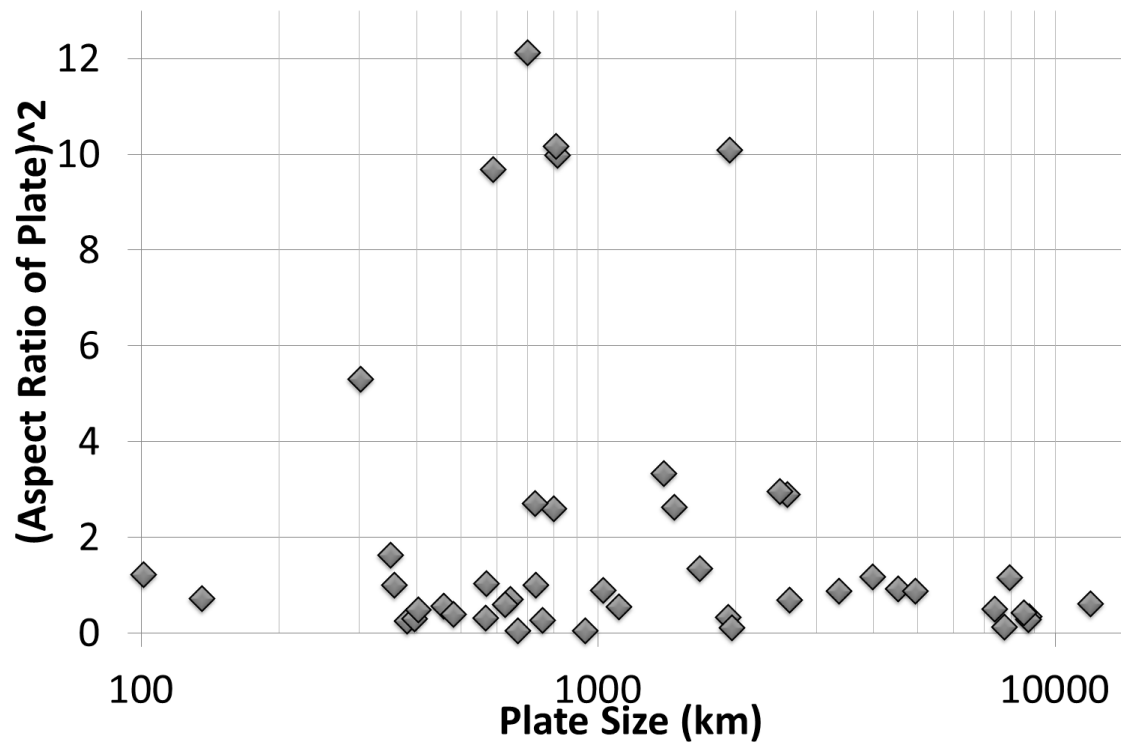
Fig. C.14   Aspect ratio of each plate as a function of plate size. Note that small plates in this figure (left side) correspond to high spherical harmonic degrees in Figure 2.3 (right side).

C.3 Effect of roundness

When a plate has a spin motion, as the geometry of the plate becomes circular, i.e., increases the roundness, the toroidal power increases since the vorticity (toroidal component) along the plate boundary is generated but the divergence (poloidal component) almost vanishes (Figure 2.5). To confirm the correlation between the roundness of a plate with a spin motion and the toroidal/poloidal ratio, we consider three virtual plates on the Earth, hexagon (six sides and angles), octagon (eight sides and angles) and dodecagon (twelve sides and angles) and impose spin motion by putting the same Euler pole ($1°$/Myr) at the center of the plate (Figure C.15). The result of spherical harmonic expansion ($2 < l < 100$) is Figure C.16 (power spectra) and C.17 (ratio). Figure C.17 shows that, although the minimum value of the spectra of the ratio does not vary, the maximum amplitude correlates with the roundness although Figure C.16 exhibits that the roundness does not change the amplitude of the power spectrum and, thus, the effect of roundness on the observed toroidal/poloidal ratio would not be strong. In order to consider the effect of the roundness on the observed toroidal/poloidal ratio, in PB2002 we calculate the length from the center of a plate to the plate boundary, compile the data by each plate and obtain how disperse the length from the average, i.e., standard deviation. Please note that the average length of a plate represents the radius of the plate size. In order to compare the deviation of each plate, we calculate the coefficient of variation (= standard deviation / average). The smaller the coefficient of variation, the higher roundness the plate geometry has. The result is Figure C.18, demonstrating that there is no systematic decrease in the coefficient; therefore, the roundness is not the cause of the increase in the observed toroidal/poloidal ratio.
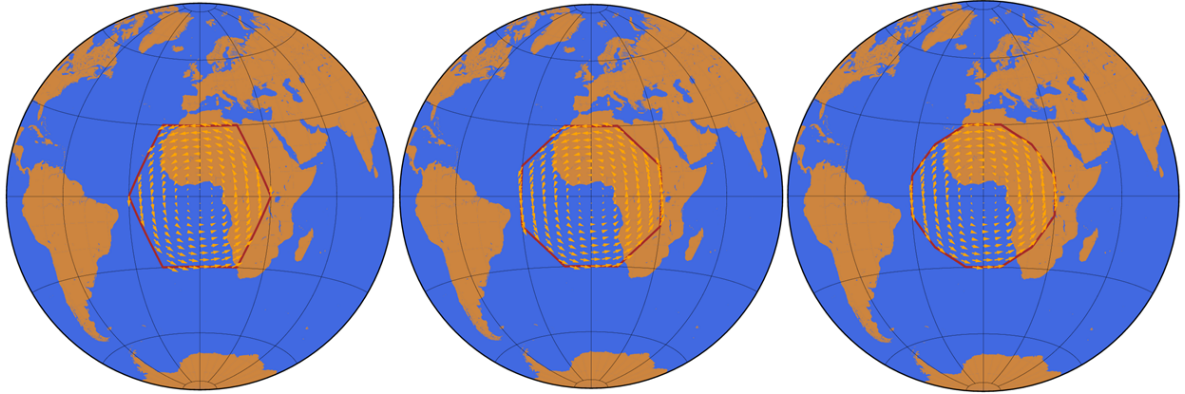
Fig. C.15   Ideal plate with a different roundness. The geometry of those plates is hexagon, octagon and dodecagon (left to right). All the plates have the same Euler pole at the center.
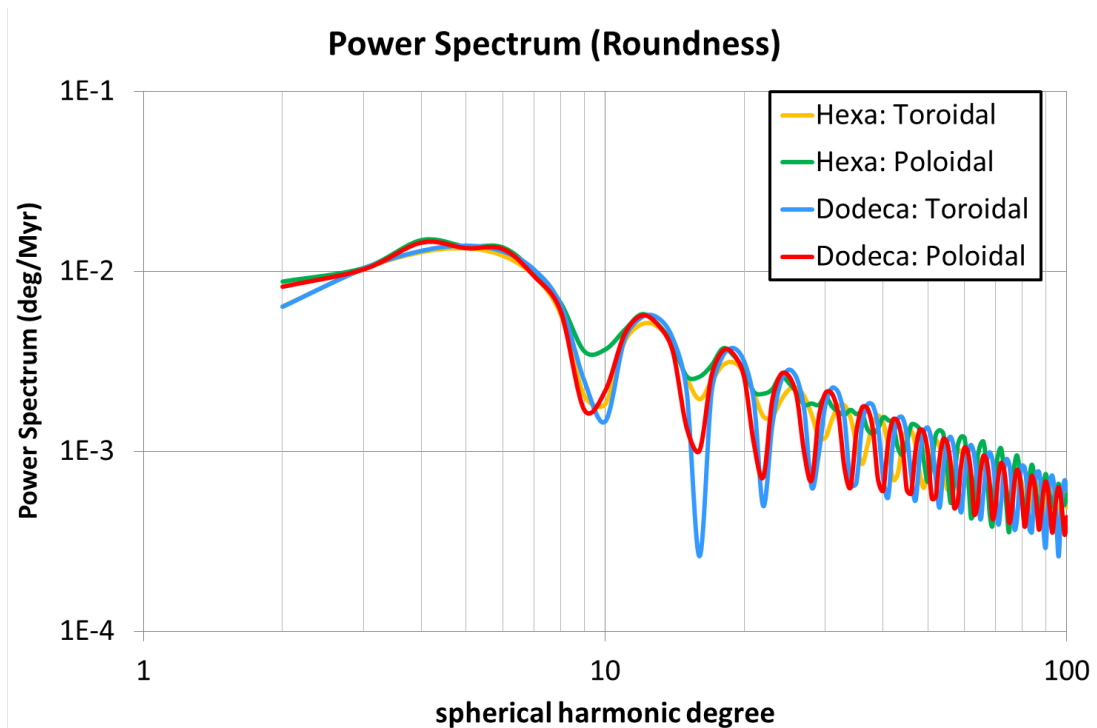

Fig. C.16   Toroidal-poloidal power spectrum of the plate with a different roundness. Orange and green lines represent the result of toroidal and poloidal spectrum of hexagon, respectively. Blue and red lines represent the result of toroidal and poloidal spectrum of dodecagon, respectively.
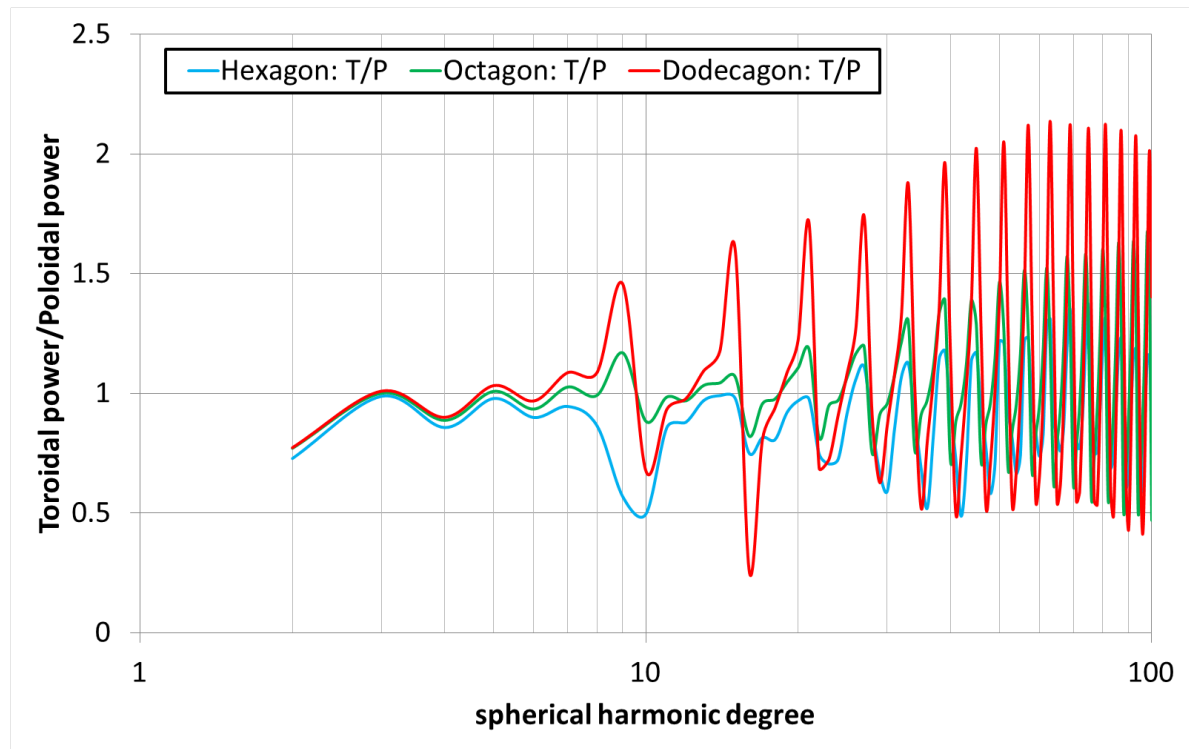
Fig. C.17   Toroidal/poloidal ratio of the plate with a different roundness. Blue, green and red lines represent the result of the hexagon, octagon and dodecagon, respectively.
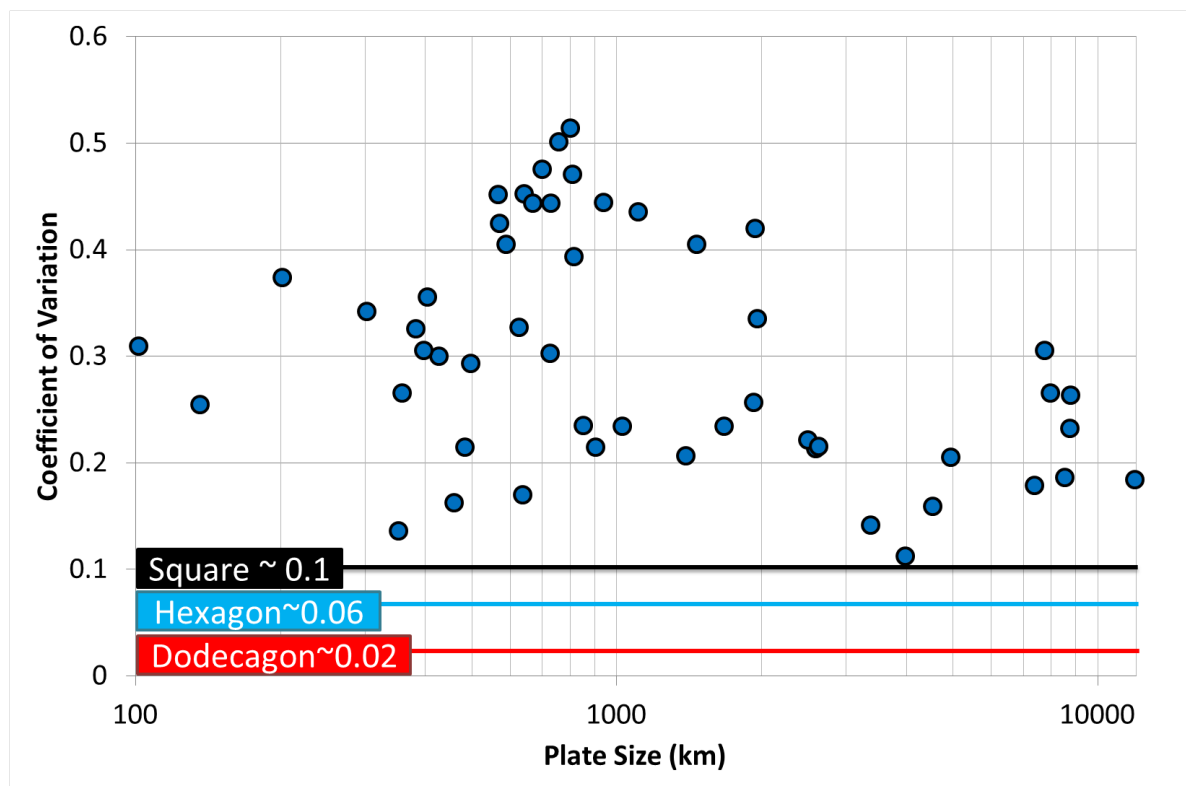
Fig. C.18   Coefficient of variation of each plate in PB2002. For comparison, we delineate three lines to represent the coefficient of variation of a square (∼ 0.1), hexagon (∼ 0.06) and dodecagon (∼ 0.02).

C.4 Effect of ridge-transform fault system

Because the Earth is sphere, the geometry of a plate receives its influence and, as a result, the geometry of subduction zone, for example, becomes arc instead of a straight line (e.g., Laravie, 1975). Another example which is expected to be more influential in the toroidal/poloidal ratio is ridge-transform fault system, in which a ridge is divided into small parts by transform faults. This geometry might affect the toroidal/poloidal ratio especially at high spherical harmonic degrees. To estimate the effect, we investigate ridges, subduction zone and transform faults in PB2002 and compile the number of each kind of plate boundary with its length. The result is Figure C.19. There are several notable features. First, although long subduction zones (mainly over 1000 km) exists (blue line in Figure C.19), ridge and transform fault are generally shorter than several hundred kilometers (red and green lines in Figure C.19, respectively), indicating that a sufficient length (mass) is necessary for plate to subduct and, in contrast, a long ridge cannot exist and is divided into short parts by short transform faults. Second, the ratio of transform fault (associated with toroidal component) to ridge and subduction zone (associated with poloidal component) (orange dashed line in Figure C.19) does not show a systematic increase until the plate boundary length becomes shorter than several ten kilometers. Hence, the effect of division of ridge by transform fault is not directly related to the increase in the observed toroidal/poloidal ratio in Figure 2.3 although the effect may induce the increase in the toroidal/poloidal ratio at very high spherical harmonic degrees, such as over 400.
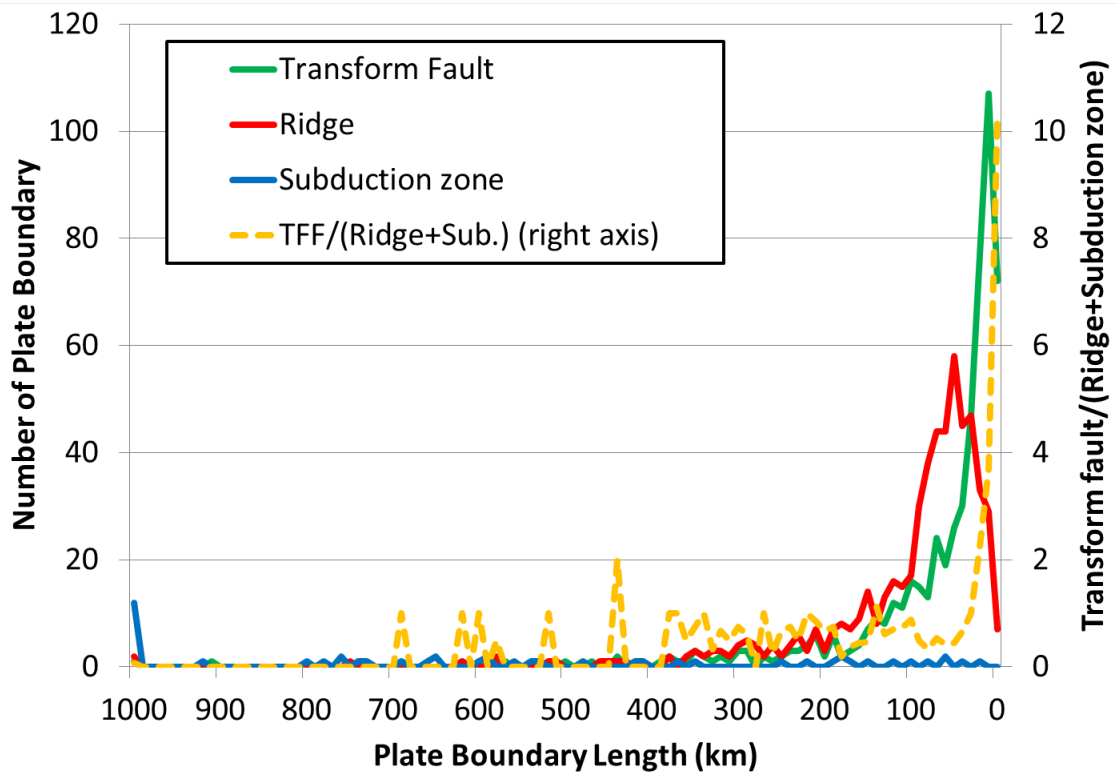
Fig. C.19   The number of plate boundaries as a function of the length. The horizontal axis means the length of plate boundary and the left vertical axis shows the number of the plate boundary. For example, if the number of ridges with the length of 90 km in the horizontal axis is 30, it means that there are 30 ridges whose length is between 90–100 km. The value at 1000 km in the horizontal axis means the number of plate boundaries whose length is more than 1000 km. Green, red and blue lines show the number of transform faults, ridges and subduction zones, respectively. The right vertical axis and orange dashed line represent the ratio of the number of transform faults to that of ridges and subduction zones.